

# Important Notice

This copy may be used only for the purposes of research and private study, and any use of the copy for a purpose other than research or private study may require the authorization of the copyright owner of the work in question. Responsibility regarding questions of copyright that may arise in the use of this copy is assumed by the recipient.

# **Binning, Static Correction, and Interpretation of P-SV Surface-Seismic Data**

**by**

**Armin W. Schafer**

An M. Sc. Thesis at the University of Calgary  
in the Department of Geology and Geophysics  
April, 1993

Supported by



THE UNIVERSITY OF CALGARY

**Binning, Static Correction, and Interpretation  
of P-SV Surface-Seismic Data**

by

Armin W. Schafer

A THESIS

SUBMITTED TO THE FACULTY OF GRADUATE STUDIES  
IN PARTIAL FULFILLMENT OF THE REQUIREMENTS FOR THE  
DEGREE OF MASTER OF SCIENCE

DEPARTMENT OF GEOLOGY AND GEOPHYSICS

CALGARY, ALBERTA

APRIL, 1993

© Armin W. Schafer 1993

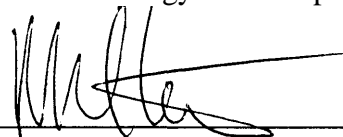
THE UNIVERSITY OF CALGARY  
FACULTY OF GRADUATE STUDIES

The undersigned certify that they have read and recommend to the Faculty of Graduate Studies for acceptance, a thesis entitled "Binning, Static Correction, and Interpretation of P-SV Surface-Seismic Data" submitted by Armin W. Schafer in partial fulfillment of the requirements for the degree of Master of Science.



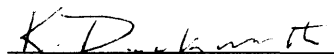
Supervisor, Dr. R. J. Brown,

Department of Geology and Geophysics



Dr. R. R. Stewart,

Department of Geology and Geophysics



Dr. K. Duckworth,

Department of Geology and Geophysics



Dr. R. M. Rangayyan

Electrical and Computer Engineering

April 29, 1993

## Abstract

In this thesis, some of the problems of using converted-wave (P-SV) surface-seismic data are examined. A general processing flow for converted-wave data is presented and discussed. Converted-wave binning methods are examined by applying them to structurally complex P-SV synthetic-seismic data. P-SV dip moveout (DMO) and depth-variant binning give very good results, while the asymptotic approximation fails for the shallow section and common midpoint (CMP) binning provides a poor result. Converted-wave static correction methods are examined by applying them to the radial component of a multicomponent surface-seismic data set from Slave Lake, Alberta. Hand-picking and common receiver point (CRP) stack-power optimization provide good results, while the P-SV refraction static correction methods fails to satisfactorily remove all the static shifts. Converted-wave interpretation is examined by analyzing a two-component surface-seismic data set from Crystal East, Alberta. For these data, lateral variations of  $V_P/V_S$  can be used to delineate a Viking sandstone channel.

## **Acknowledgments**

Many individuals and companies have made valuable contributions to this work. Dr. R. J. (Jim) Brown provided his excellent editing capabilities and offered numerous suggestions. Mark Harrison answered many questions concerning P-SV processing and Chakrit Sukaramongkol offered the use of his P-SV synthetic-seismic model. Tina Howell and Dr. Don Lawton provided ongoing support and assistance with computer applications. Scott Graham and Unocal Canada Ltd. generously donated the Slave Lake data set and Alberta Energy Company Ltd. donated the Crystal East data set. Peter Cary and David Eaton developed the CRP stack-power optimization program, which was implemented on Pulsonic Geophysical's computer system. Western Geophysical and ITA graciously allowed The University of Calgary to use their processing software. Finally, the sponsors of the CREWES project provided invaluable financial assistance.

I am deeply indebted to all these people, and would also like to thank my family and friends; especially my mother, Rosemarie, and girlfriend, Jodie Retzlaff, for all of their understanding and support throughout my term at University.

## Table of Contents

Approval Page .....	ii
Abstract .....	iii
Acknowledgments .....	iv
Table of Contents .....	v
List of Tables .....	viii
List of Figures .....	ix
List of Symbols, Abbreviations, and Nomenclature .....	xiv
Chapter 1 – INTRODUCTION .....	1
1.1 Background .....	1
1.2 Thesis objectives .....	3
1.3 Seismic data sets used in this thesis .....	3
1.3.1 Slave Lake, Alberta .....	3
1.3.2 Crystal East, Alberta .....	4
1.3.3 Synthetic P-SV seismic data set .....	4
1.4 Hardware and software used .....	4
Chapter 2 – GENERAL PROCESSING OF P-SV SURFACE-SEISMIC DATA .....	6
2.1 Introduction .....	6
2.2 Polarity reversal of trailing spread .....	6
2.3 Geometric-spreading compensation .....	8
2.4 P-SV stacking velocity estimation and NMO correction .....	9
2.5 P-SV static corrections .....	11
2.6 CCP binning .....	11
Chapter 3 – P-SV BINNING .....	12
3.1 Introduction .....	12

3.2	P-SV Synthetic data set -----	13
3.2.1	Design -----	13
3.2.2	Acquisition and processing -----	15
3.3	Binning theory -----	16
3.3.1	Asymptotic CCP approximation -----	16
3.3.2	Depth-variant CCP -----	17
3.3.3	Dip moveout (DMO) -----	17
3.4	Binning results -----	18
3.5	Discussion -----	19
Chapter 4 - THREE-COMPONENT SEISMIC DATA PROCESSING: SLAVE		
	LAKE, ALBERTA -----	23
4.1	Introduction -----	23
4.2	Data acquisition -----	23
4.4	Discussion -----	35
Chapter 5 - P-SV STATIC CORRECTION -----		
5.1	Introduction -----	41
5.2	Hand-picked static correction -----	42
5.3	Refraction methods -----	46
5.3.1	Time-difference refraction static correction -----	48
5.3.2	EGRM Gauss-Seidel Refraction Static correction -----	50
5.4	CRP stack-power optimization -----	52
5.5	Comparison of static-correction methods -----	53
5.6	Discussion -----	59
Chapter 6 - Two-component seismic data processing: Crystal East, Alberta -----		
6.1	Introduction -----	62
6.2	Data acquisition -----	62

6.3	Data Processing .....	65
6.4	Discussion .....	78
Chapter 7 - CONVERTED-WAVE INTERPRETATION .....		80
7.1	Introduction .....	80
7.2	Event interpretation and correlation between P-P and P-SV seismic sections .....	80
7.4	Discussion .....	86
Chapter 8 – SUMMARY AND CONCLUSIONS .....		88
8.1	Summary .....	88
8.2	Conclusions .....	89
REFERENCES .....		91

## List of Tables

Table 3.1.	Physical parameters of the Highwood Structure P-SV synthetic-seismic model. -----	15
Table 4.1.	Acquisition parameters for the Slave Lake survey. -----	25
Table 4.2.	Processing sequence and parameters for the vertical-component data. ----	29
Table 4.3.	Processing sequence and parameters for the radial-component data. -----	30
Table 6.1.	Field acquisition and recording parameters for the Crystal East survey.-----	65
Table 6.2.	Processing sequence and parameters for the vertical-component (P-P) data.-----	68
Table 6.3.	Processing sequence and parameters for the radial-component (P-SV) data.-----	69
Table 6.4.	$V_P/V_S$ ratios computed from event and interval time for vertical (P-P) and radial (P-SV) component data.-----	78

## List of Figures

FIG. 2.1.	Radial-component processing flow. Highlighted steps are discussed in this chapter. See also Harrison (1992). -----	7
FIG. 2.2.	Schematic diagram of a P-SV survey demonstrating the need to reverse the polarity of the trailing spread. -----	8
FIG. 3.1.	Schematic diagram showing conversion-point trajectory, asymptotic approximation, and converted-wave raypaths. -----	13
FIG. 3.2.	Location map of the Highwood Structure, Turner Valley, Alberta.-----	14
FIG. 3.3.	Thrust-fault model based on the Highwood Structure, Turner Valley. -----	14
FIG. 3.4.	Highwood Structure P-SV synthetic seismic section using CMP binning: (a) without polarity reversals; (b) with polarity of trailing spread reversed. -----	20
FIG. 3.5.	Highwood Structure P-SV synthetic seismic section using asymptotic CCP binning: (a) without polarity reversals; (b) with polarity of trailing spread reversed. -----	21
FIG. 3.6.	Highwood Structure P-SV synthetic seismic section using depth-variant CCP binning with polarity of trailing spread reversed.-----	22
FIG. 3.7.	Highwood Structure P-SV synthetic seismic section using P-SV DMO with polarity of trailing spread reversed. -----	22
FIG. 4.1.	Location map of the Slave Lake survey: (a) inside Alberta; (b) close-up of lines EUE001 and EUE002. -----	24
FIG. 4.2.	Sample shot record from the vertical-component (P-P) data from Slave Lake for shots located at: (a) station 101; (b) station 461. -----	26
FIG. 4.3.	Sample shot record from the radial-component (P-SV) data from Slave Lake for shots located at: (a) station 101; (b) station 461. -----	27

FIG. 4.4.	Sample shot record from the transverse-component (P-SH) data from Slave Lake for shots located at: (a) station 101; (b) station 461. -----	28
FIG. 4.5.	Sample velocity-analysis plots for the vertical component of line EUE001: (a) common offset stacked section; (b) semblance-analysis plot; (c) stack power. -----	31
FIG. 4.6.	Sample velocity-analysis plots for the radial component of line EUE001: (a) common offset stacked section; (b) semblance-analysis plot; (c) stack power. -----	32
FIG. 4.7.	NMO-corrected common offset stacked gathers showing the mute functions used: (a) P-P; (b) P-SV. -----	33
FIG. 4.8.	Amplitude spectra from fast Fourier transformation of ten adjacent traces: (a) P-P; (b) P-SV. -----	34
FIG. 4.9.	Final stacked sections from line EUE001 with poststack $f-k$ filter applied: (a) P-P; (b) P-SV. -----	36
FIG. 4.10.	Final stacked section of the transverse component from line EUE001 with poststack $f-k$ filter applied. -----	37
FIG. 4.11.	Final receiver static solutions for line EUE001. -----	37
FIG. 5.1.	Near-surface P-wave and S-wave velocity structures from Jumping Pound, Alberta (from Lawton, 1990). -----	42
FIG. 5.2.	CSP-stacked sections without any static-corrections applied: (a) P-P; (b) P-SV. -----	43
FIG. 5.3.	CSP-stacked sections with hand-picked and residual static-corrections applied: (a) P-P; (b) P-SV. -----	43
FIG. 5.4.	CRP-stacked sections without any static-corrections applied: (a) P-P; (b) P-SV. -----	44

FIG. 5.5.	CPR-stacked sections with hand-picked and residual static-corrections applied: (a) P-P; (b) P-SV. -----	45
FIG. 5.6.	Definition of traveltimes, time differences, and source-receiver offsets for the time difference method (Lawton, 1989).-----	49
FIG. 5.7.	Geometry of the raypath for the $n$ -layer model, showing a wave refracted at the $n$ th layer -----	50
FIG. 5.8.	Definition of thickness at the receiver, offset between the receivers; and forward, reverse, and total travelpaths for a two-layer model ( $n=2$ ). -----	51
FIG. 5.9.	Time-difference S-wave Earth models: (a) thicknesses ; (b) velocities.----	54
FIG. 5.10.	EGRM Gauss-Seidel S-wave Earth models: (a) thicknesses; (b) velocities. -----	55
FIG. 5.11.	CRP-stacked section with time-difference refraction static solution applied. -----	56
FIG. 5.12.	CRP-stacked section with EGRM Gauss-Seidel refraction static solution applied. -----	56
FIG. 5.13.	CRP-stacked section with hand-picked and some residual static solution applied. -----	57
FIG. 5.14.	CRP-stacked section with CRP stack-power optimization static solution applied. -----	57
FIG. 5.15.	Comparison of the receiver static solutions. -----	58
FIG. 6.1.	Location map of the Crystal East survey: (a) inside Alberta; (b) close-up of lines 6222, 6223, and 6224. -----	63
FIG. 6.2.	Shot record at station 146 from line 6223: (a) vertical-component (P-P) data; (b) radial-component (P-SV) data. -----	64
FIG. 6.3.	Sample velocity-analysis semblance plots for line 6223: (a) P-P;	

	(b) P-SV. -----	66
FIG. 6.4.	Sample NMO-corrected common offset stacked records: (a) P-P; (b) P-SV. The applied mute function for station 146 is shown on both records. -----	67
FIG. 6.5.	Averaged time-variant cross-power spectra between adjacent stacked traces from line 6223: (a) P-P; (b) P-SV. Contours are in percentage of maximum. -----	71
FIG. 6.6.	Final receiver static solutions for line 6223: (a) P-P; (b) P-SV. -----	72
FIG. 6.7.	Final stacked sections from line 6222 with poststack <i>f-k</i> filter applied: (a) P-P; (b) P-SV. -----	73
FIG. 6.8.	Final stacked sections from line 6223 with poststack <i>f-k</i> filter applied: (a) P-P; (b) P-SV. -----	74
FIG. 6.9.	Final stacked sections from line 6224 with poststack <i>f-k</i> filter applied: (a) P-P; (b) P-SV. -----	75
FIG. 6.10.	Correlation of the radial components of the Crystal East survey. -----	76
FIG. 6.11.	Reflection correlation between (a) the vertical-component (P-P) section and (b) the radial-component (P-SV) section from line 6224. -----	77
FIG. 7.1.	P-P synthetic seismograms for offsets ranging from zero to 3125 m, generated from the P-wave sonic and density logs of well 8-9-45- 3W5: (a) without mute; (b) with mute applied. -----	83
FIG. 7.2.	P-SV synthetic seismograms for offsets ranging from zero to 2500 m, generated from the P-wave sonic and density logs of well 8-9-45- 3W5, using a $V_p/V_s$ of 2.0: (a) without mute; (b) with mute applied. -----	84
FIG. 7.3.	Identification of events and correlation between vertical component (P-P) and radial component (P-SV) of line 6223 using P-P and P-SV	

	synthetics generated from the P-wave sonic and density logs of well 8-9-45-3W5. ....	85
FIG. 7.4.	$V_P/V_S$ versus $V_P$ for sandstone, limestone, and shale (Miller and Stewart, 1990).....	87
FIG. 7.5.	(a) Viking sand channel model and (b) corresponding $V_P/V_S$ anomaly for line 6223 of the Crystal East survey. ....	87

## List of Symbols, Abbreviations, and Nomenclature

P	compressional
$\alpha, V_P$	P-wave velocity
P-P	compressional-source, vertical component data
S	shear
$\beta, V_S$	S-wave velocity
P-SV	compressional-source, radial component data, also known as converted-wave data
$\gamma, V_P/V_S$	ratio of P-wave to S-wave velocities
P-SH	compressional-source, transverse component data
NMO	normal moveout
CMP	common midpoint
CCP	common conversion point
CSP	common source point
CRP	common receiver point

## Chapter 1 – INTRODUCTION

### 1.1 Background

Converted waves are defined in the Encyclopedic Dictionary of Exploration Geophysics (Sheriff, 1991) as "seismic energy which has traveled partly as a *P*-wave and partly as an *S*-wave, being converted from one to the other upon reflection or refraction at oblique incidence on an interface." The use of converted waves in exploration geophysics has only gained popularity in the 1980s, even though shear-wave recording can be traced back into the 1800s, in earthquake studies.

The earliest seismic instrument was invented in 132 A. D., in China. This seismoscope consisted of a wine jar with a diameter of six feet, believed to enclose an inverted pendulum, which recorded the direction of an earthquake by releasing a ball into one of eight porcelain toads oriented in the major directions of the compass (Dewey and Byerly, 1969). The next series of instruments were pendulum seismometers, dating back to the nineteenth century, which measured horizontal ground motion. The original definition of earthquake magnitude is based upon displacement observed on a Wood-Anderson torsional seismometer (Richter, 1935), although this did not measure shear-wave energy, but measured the horizontal motion associated with the first-arriving *P* wave.

In the early part of this century, the era of exploration geophysics began with the use of an impulsive source and vertical geophones that recorded the *P*-wave energy. *P* waves were first used for exploration purposes largely for convenience. *P*-wave surveys employed simple vertical-component geophones, which were simpler and more robust than multicomponent geophones. Further, *P*-wave sources were easier to generate than shear-wave sources and the transit-times were easier to determine from *P*-waves.

The first observations of S waves outside of earthquake seismology were S-wave arrivals in a conventional check-shot survey by Horton (1943). These were followed by several observational studies that used P waves and S waves along with multicomponent geophones to understand fundamental seismic wave propagation (Jolly, 1956; White et al., 1956; Press and Dobrin, 1956). In the 1960s, attempts were made to take advantage of the theoretically higher vertical resolution of S waves for structural mapping (Cherry and Waters, 1968; Erickson et al., 1968). Unfortunately, the attenuation of higher frequencies limited the wavelengths of S waves to those of P waves, hence the anticipated increase in vertical resolution was not observed. Further, large S-wave static corrections hindered the use of S waves for exploration purposes.

Experimental studies by Pickett (1963) initiated the idea of using S waves for stratigraphic mapping by relating  $V_p/V_s$  values to lithology. Gardner and Harris (1968) followed this result by relating  $V_p/V_s$  anomalies to gas saturation. These results spurred the start of the Conoco Shear-Wave Group Shoot in 1976. The goals of this venture were to distinguish P-wave bright spots caused by gas saturation from those caused by lithologic variations, to examine the use of  $V_p/V_s$  ratios as an indication of lithology or porosity variations, and to test S-waves in no-reflection (NR) areas. The results of this survey were published by several authors (Ensley, 1984; Winterstein and Hanten, 1985; Winterstein, 1986; Robertson and Pritchett, 1985; Tatham, 1985; Tatham and Krug, 1985; Anno, 1987; Corbin et al., 1987), and led to further S-wave studies by other companies.

The first use of converted-wave (P-SV) surface-seismic data for exploration purposes was by Garotta et al. (1985). They used a P-wave source and two-component geophones to simultaneously record the vertical component of motion (P-P) and the radial component of motion (P-SV). Lateral variations in lithology were successfully mapped to changes in  $V_p/V_s$  ratio, obtained by matching events on the P-P data to those

on the P-SV data. The  $V_p/V_s$  ratio can also be derived from the stacking velocities of the P-P and P-SV data (Iverson et al., 1989). Nazar (1991) also demonstrated the possibility of using P-SV data for lithology identification through amplitude-versus-offset (AVO) analysis.

## **1.2 Thesis objectives**

This thesis attempts to solve some of the common problems likely to be encountered when multicomponent seismic data are used in hydrocarbon exploration. Differences observed during the processing of two different multicomponent surface-seismic data sets are described. An algorithm for converted-wave binning using the asymptotic approximation is described and tested on field data and structurally complex synthetic-seismic data. Various converted-wave static correction methods are applied to the field data from Slave Lake: including several refraction static correction methods, a hand-picking method, and residual static correction methods. Finally, the interpretation of multicomponent seismic data is discussed, citing an example of a two-component seismic data set that was used to find sandstone channels that conventional seismic data could not image.

## **1.3 Seismic data sets used in this thesis**

Two multicomponent surface-seismic data sets and a P-SV synthetic-seismic data set are used in this thesis.

### **1.3.1 Slave Lake, Alberta**

A three-component data set was recorded using an array of four half-kilogram dynamite charges as sources in March of 1988 by Petty-Ray Geophysical of Canada. This

data set has been donated by Unocal Canada Ltd. to the CREWES Project at The University of Calgary for analysis. Details of the processing of line EUE001 of this data set are discussed in Chapter 4.

### 1.3.2 Crystal East, Alberta

A two-component surface-seismic data set was recorded using 1-kg dynamite charges as sources in November of 1985 by Compagnie Générale de Géophysique (CGG). This data set has also been donated to the CREWES Project at The University of Calgary by Alberta Energy Company Ltd. The processing of this data set is discussed in Chapter 6, and some aspects of the interpretation of this data set are discussed in Chapter 7.

### 1.3.3 Synthetic P-SV seismic data set

The synthetic data set used for testing the P-SV asymptotic CCP binning program (Chapter 3) was modelled after the Highwood Structure and was created using the UNISEIS seismic modelling software on a Landmark RT workstation.

## 1.4 Hardware and software used

Some initial processing of the Slave Lake data set and all the processing of the Crystal East data set were performed using the processing software of Western Geophysical, operating on an IBM 4381-Q03 mainframe computer using the MVS operating system. The processing of the Slave Lake data set was completed on Sun workstations using the "Insight" processing system of Inverse Theory and Applications (ITA), which replaced the IBM mainframe and the Western Geophysical software. ITA software is running on a UNIX platform on a Sun Microsystems Inc. 470 workstation,

which is linked to eight SPARC II workstations. The P-SV asymptotic binning code was written in FORTRAN 77 on the Sun SPARC II workstations. The seismic data plots are generated on either the 24" Versatec 8224 plotter or the 11" VER-120 thermal plotter using ITA's plotting subroutines. All the text-processing functions are running on an Apple Macintosh IIsi computer. Most of the figures used have been scanned using the Abaton SCAN 300/COLOR scanner and the Adobe Photoshop® software package. The scanned images were then transferred as TIFF format files into Pagemaker® for labelling. Some figures are reduced from large paper sections using a photographic reduction technique (PMT) and then labelled by hand. Other figures were created using the Canvas® drawing package and graphs are generated using Cricketgraph®. Basic text processing, including tables and equations, was done using Microsoft Word 5.0®.

## **Chapter 2 – GENERAL PROCESSING OF P-SV SURFACE-SEISMIC DATA**

### **2.1 Introduction**

This chapter outlines a general processing flow for P-SV seismic data (Figure 2.1) and examines some of the unique aspects of P-SV processing relative to P-P processing. The use of the P-P data to assist in the processing of the P-SV data is also discussed. Detailed examinations of the processing of two multicomponent seismic data sets follow in Chapters 4 and 6.

### **2.2 Polarity reversal of trailing spread**

P-SV mode conversion has radial symmetry about the source location for an isotropic Earth with flat, homogeneous layers; therefore, P-SV particle motion will always be oriented away from the source. However, the multicomponent phones are usually positioned to have the radial component of the phone aligned in the direction that the survey is being shot. Thus, if the survey is being shot from the South to the North (Figure 2.2), the radial component of the geophones will all be oriented toward the North, but the P-SV particle motion in the trailing spread will be toward the South. To avoid having an opposite polarity between the trailing and the leading spreads, the trailing spread is reversed to match the leading spread. The leading spread could have been reversed instead of the trailing spread; the trailing spread was simply chosen to result in a stacked section where a positive velocity increase is a peak.

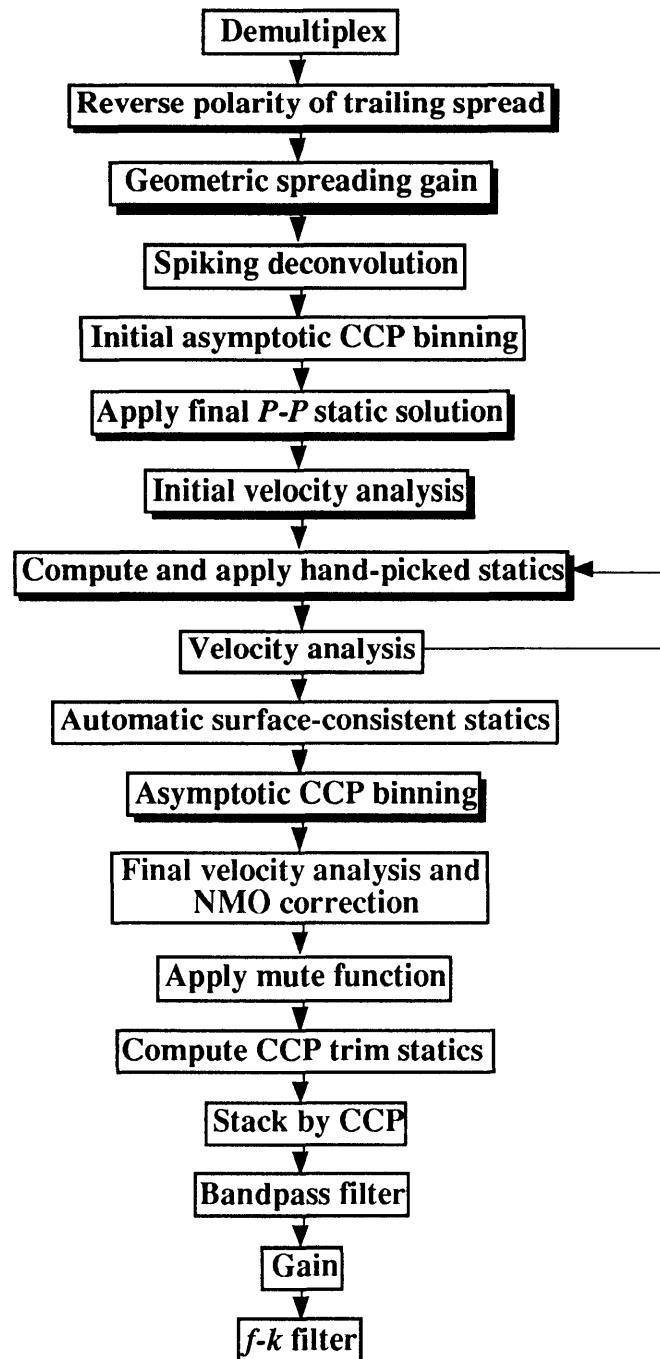


FIG. 2.1. Radial-component processing flow. Highlighted steps are discussed in this chapter. See also Harrison (1992).

### 2.3 Geometric-spreading compensation

Geometric spreading corrections are necessary to correct for the amplitude loss that occurs due to the spreading of energy in a spherical wavefront. For the P-P case, Newman (1973) has derived a spreading compensation formula which is dependent on the root-mean-square (RMS) stacking velocity. Newman states that the divergence factor at normal incidence,  $D_0$ , is given by

$$D_0 = \frac{t_0 \tilde{\alpha}^2}{\alpha_0}, \quad (2.1)$$

where

$$\tilde{\alpha} = \sqrt{\frac{\sum_{i=1}^n t_i \alpha_i^2}{t_0}}, \quad (2.2)$$

$t_0 = \sum_{i=1}^n t_i$ , the two-way P-wave reflection time,  $\alpha_0$  is the P-wave velocity in the first layer,  $\tilde{\alpha}$  is the time-weighted P-wave RMS velocity commonly used in normal moveout (NMO) calculations,  $t_i$  is the time required to travel through the layer  $i$ , and  $\alpha_i$  is the P-wave velocity in layer  $i$ .

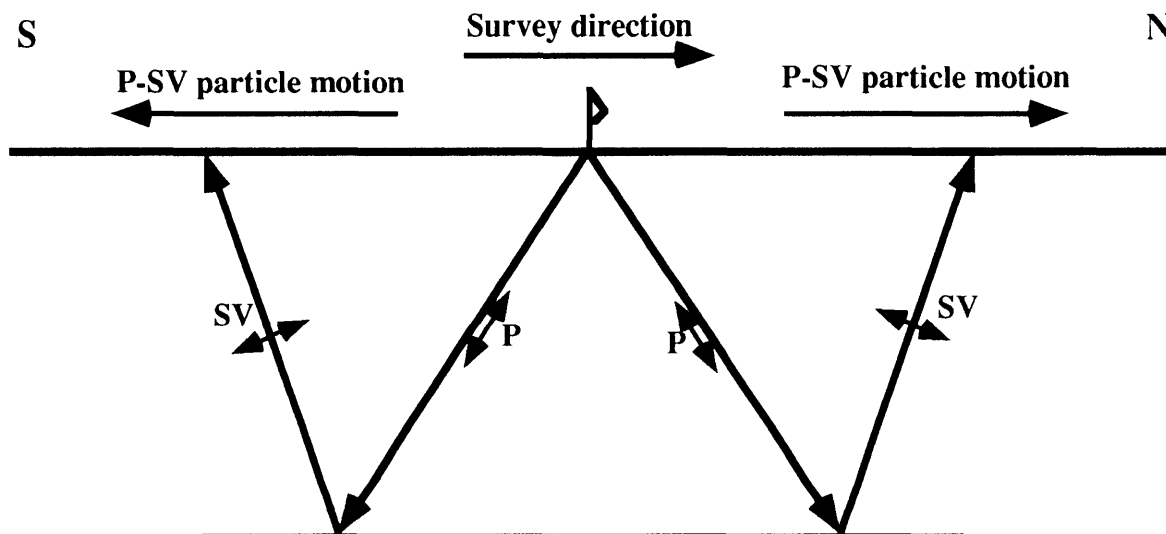


FIG. 2.2. Schematic diagram of a P-SV survey demonstrating the need to reverse the polarity of the trailing spread.

Ursin (1990) and Harrison (1992) have extended this geometrical spreading correction to include the P-SV case. Their final formula for the P-SV divergence factor at normal incidence is

$$D_0 = \frac{t_{P-SV_0} \tilde{v}^2}{\alpha_0}, \quad (2.3)$$

where  $t_{P-SV_0}$  is the two-way P-SV vertical traveltime, and  $\tilde{v}$  is the time-weighted P-SV RMS velocity (Harrison, 1992),

$$\tilde{v} = \sqrt{\frac{1}{t_{P-SV_0}} \int_0^{t_{P-SV_0}} \alpha(\tau) \beta(\tau) d\tau}. \quad (2.4)$$

Tessmer and Behle (1988) have shown that the stacking velocities obtained by conventional velocity analysis are identical in the first order to the P-SV RMS velocity. Using these results, P-SV geometric spreading can be compensated for by using the P-SV stacking velocity function and total two-way traveltime, and the P-wave velocity of the first layer in the near-surface.

## 2.4 P-SV stacking velocity estimation and NMO correction

Tessmer and Behle (1988) show that, to first order, P-SV moveout curves are given by the hyperbolic function

$$t_{P-SV}^2 = t_{P-SV_0}^2 + \frac{4h^2}{\tilde{\varphi}^2}, \quad (2.5)$$

where  $h$  is the source-receiver half-offset. The P-SV stacking velocity  $\tilde{\varphi}$  is the discretized form of equation (2.4);

$$\tilde{\varphi} = \sqrt{\frac{\sum_{i=1}^n \alpha_i \beta_i \tau_i}{\sum_{i=1}^n \tau_i}}, \quad (2.6)$$

where

$$\begin{aligned} \tau_i &= \left( \frac{1}{\alpha_i} + \frac{1}{\beta_i} \right) z_i \\ &= (1 + \gamma_i) \frac{z_i}{\alpha_i}, \quad \gamma_i = \frac{\alpha_i}{\beta_i}, \end{aligned} \quad (2.7)$$

where  $z_i$  is the thickness of layer  $i$ .

The hyperbolic nature of the first-order P-SV NMO curves allows conventional (hyperbolic) velocity analysis (Taner and Koehler, 1969) to yield a P-SV stacking function. Unfortunately, the error associated with the hyperbolic approximation for P-SV moveout curves increases with offset. To reduce this error for increased offsets, Slotboom (1990) has derived a shifted-hyperbola NMO equation that is more accurate as offset increases than the hyperbolic approximation. The shifted-hyperbola NMO correction method was used for the P-SV synthetic stacked sections (Chapter 6), but all the surface-seismic data processing procedures used the conventional hyperbolic moveout method.

Since P-SV static shifts severely affect any attempts at conventional types of velocity analysis, such as semblance plots, it is necessary to obtain an estimate of the P-SV velocities from other sources. Tessmer and Behle (1988) and Harrison (1992) have shown that an initial estimate of the P-SV stacking velocities can be derived from the P-P stacking velocities. If a constant velocity ratio,  $\gamma$ , is assumed, then the P-SV RMS velocity,  $\tilde{\varphi}$ , is related to the P-P RMS velocity,  $\tilde{\alpha}$ , by

$$\tilde{\varphi} = \frac{\tilde{\alpha}}{\sqrt{\gamma}}, \quad (2.8)$$

and the P-SV vertical travelttime,  $t_{P-SV_0}$ , is related to the P-P vertical travelttime,  $t_0$ , as (Harrison, 1992):

$$t_{P-SV_0} = \frac{(1+\gamma)}{2} t_0. \quad (2.9)$$

Equations (2.8) and (2.9) are then used for an initial estimation of P-SV stacking velocities, which allows for static correction analysis to be carried out.

## 2.5 P-SV static corrections

P-SV static shifts are a major problem encountered in the processing of P-SV surface-seismic data. Unlike the initial P-SV velocity analysis solution, the P-SV static solution does not correspond to the P-P static solution (Nazar, 1991; Schafer, 1991; Harrison, 1992). The problem of P-SV static corrections will be discussed in detail in Chapter 4.

## 2.6 CCP binning

Several authors (Chung and Corrigan, 1985; Behle and Dohr, 1985; Fromm et al., 1985; Tessmer and Behle, 1988; Eaton et al., 1990) have shown that the lateral location of the mode-conversion point varies with depth for converted waves. A detailed comparison and discussion of the various methods for binning P-SV data is presented in Chapter 3.

## Chapter 3 – P-SV BINNING

### 3.1 Introduction

Early seismic surveys consisted of single-fold coverage; that is, at the location of each reflection point at depth, there was only one raypath sampling this area. To increase the signal-to-noise ratio, the use of multifold data was first attempted in 1956 (Mayne, 1956 and 1962). The advantage of multifold data is that most of the random noise is removed when several traces at the same depth location are combined (stacked) to form one trace. However, to combine the correct traces, it is necessary to sort the data based upon common midpoint (CMP) locations. A CMP location is the location of the point of reflection of seismic waves. A CMP bin consists of a group of CMP locations, which are gathered into one CMP "gather". This gather is then NMO-corrected and stacked to form one trace, corresponding to one CMP location on a multifold seismic section.

This method of CMP binning and stacking has worked well for P-wave data, but recent interest in converted-wave surveys has raised the issue of proper CMP binning for P-SV data (Chung and Corrigan, 1985, and Fromm et al., 1985). Assuming horizontal reflectors, the location of the reflection point for P-P seismic data is below the midpoint between the source and the receiver due to the symmetry of the raypath. Thus, sorting P-wave data from the shot and receiver locations into the actual point of reflection is simply a matter of dividing the source-receiver offset by two. However, the raypaths are not symmetrical for converted-wave reflections, since the downgoing P wave travels at roughly twice the velocity of the upgoing S wave. The upgoing raypath bends toward the normal as predicted by Snell's law and will be shorter than the downgoing raypath (Figure 3.1). This offsets the mode-conversion point away from the midpoint and towards the receiver location. The lateral location of this conversion point also varies with depth (Tessmer and Behle, 1988; Fromm et al., 1985), ranging from a deep-reflection

asymptotic position roughly two-thirds of the way from source to receiver to a position almost approaching the receiver location at shallower depths (Eaton et al., 1990).

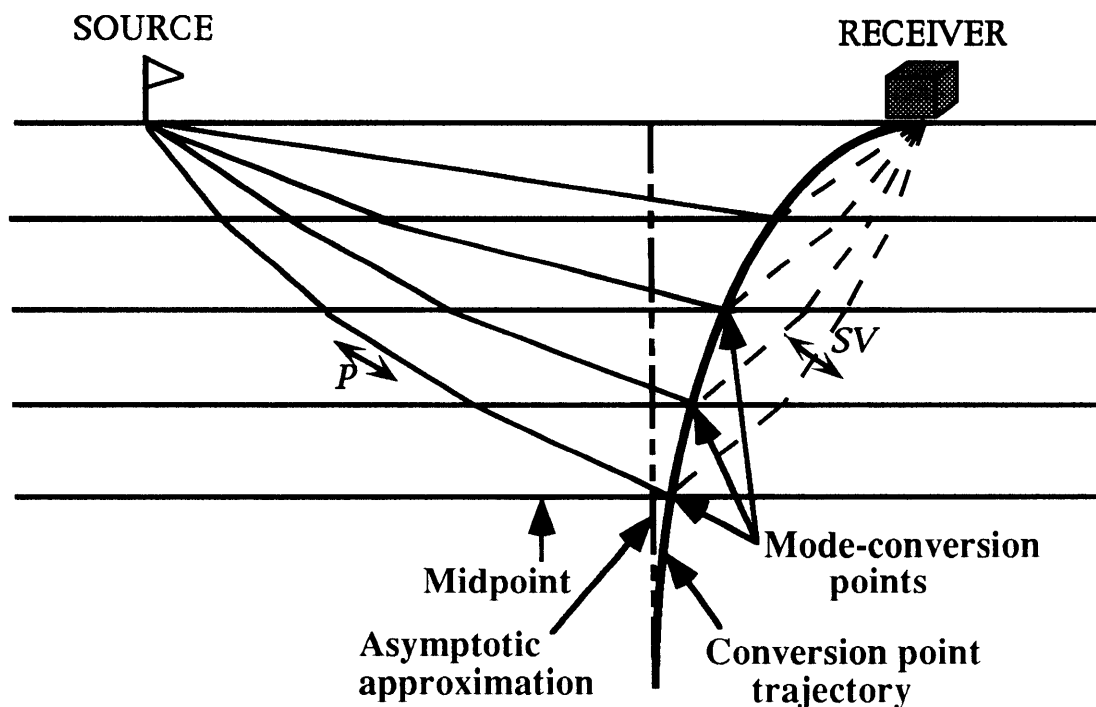


FIG. 3.1. Schematic diagram showing conversion-point trajectory, asymptotic approximation, and converted-wave raypaths.

## 3.2 P-SV Synthetic data set

### 3.2.1 Design

The data set used for this analysis is a synthetic P-SV seismic reflection data set which simulates a thrust fault, the Highwood structure, located near the town of Turner Valley in SW Alberta (Figure 3.2). This model is based on the interpretation of a seismic line in the area by MacKay (1991) and consists of Mississippian carbonates which have been overthrust onto Mesozoic clastics (Figure 3.3).

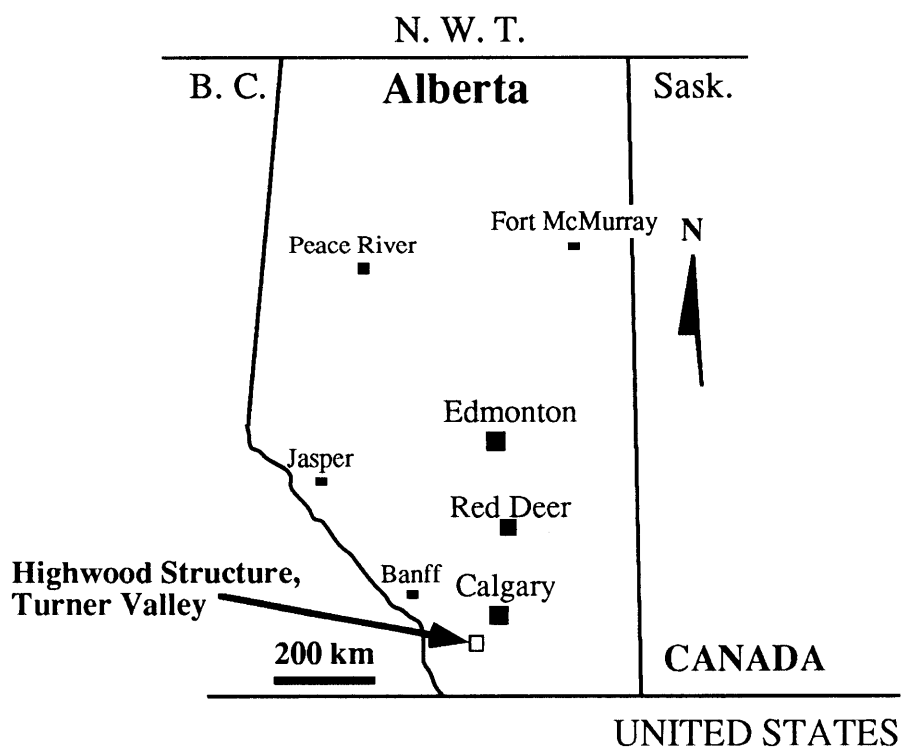


FIG. 3.2. Location map of the Highwood Structure, Turner Valley, Alberta.

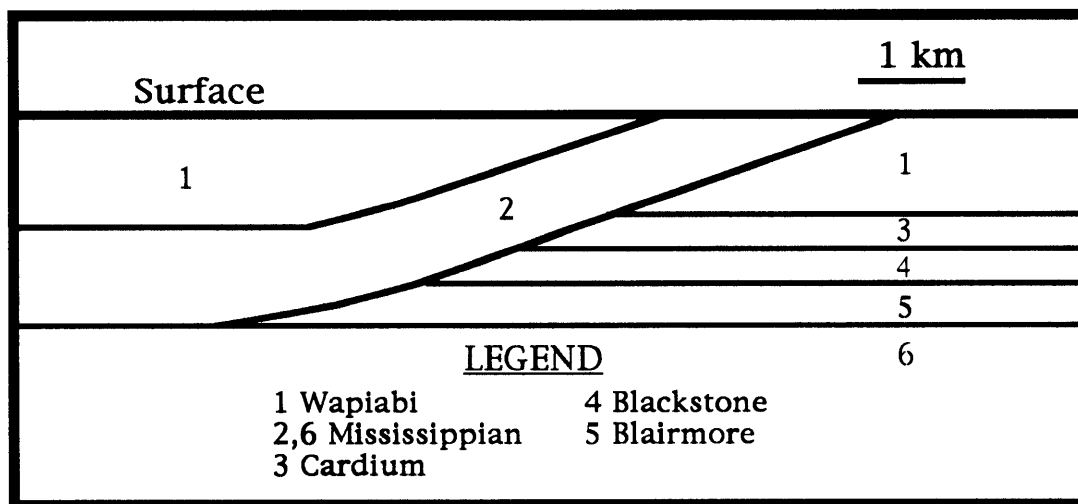


FIG. 3.3. Thrust-fault model based on the Highwood Structure, Turner Valley.

This model was implemented by Sukaramongkol and Lawton (1992) to examine the effects of near-surface, high-velocity material on P-SV seismic reflection data. The velocities and densities of each layer (Table 3.1) were derived from the well 6-19-19-3W5 and taken from Miller and Stewart (1990).

Table 3.1. Physical parameters of the Highwood Structure P-SV synthetic-seismic model.

Formations	$V_p$ (m/s)	$V_s$ (m/s)	Density ( $\text{kg/m}^3$ )	Thickness (m)
Mississippian	5500	2894	2800	1000
Wapiabi	3884	2044	2550	1200
Cardium	4300	2529	2650	230
Blackstone	4000	2139	2600	270
Blairmore	4200	2545	2650	300

### 3.2.2 Acquisition and processing

The synthetics were computed on a Landmark RT using the UNISEIS modelling software. The model was first entered into UNISEIS by hand, and then ray-traced to allow conversion from P to SV at interfaces. The ray-tracing method used the Knott-Zoepritz coefficients to accommodate amplitude variation as a function of angle of incidence. The resulting reflection-coefficient series was then convolved with a Ricker wavelet with a maximum center frequency of 20 Hz to generate the synthetic P-SV seismic reflection data. To make up the model, forty-six shot gathers were acquired using split-spread geometry, with 240 groups at 20-m intervals and with 200-m shot intervals, giving an anticipated fold of twelve.

For processing, the data were transferred to the Sun SPARC II workstations. The data were then converted from SEG-Y to ITA's INSIGHT format using ITA software. Once the headers are modified to contain the acquisition geometry, subsequent processing – such as CCP binning, sorting, NMO application and stacking – can be performed.

Most of the P-SV processing steps are similar to P-P processing steps and thus can use the same software. However, due to the asymmetric raypaths, new programs had to be written for CCP binning. Similarly, a program for P-SV dip moveout (DMO) had to be written (Harrison, 1992). Further, the nonhyperbolic nature of the P-SV moveout curve would require a nonhyperbolic NMO correction to be applied (Slotboom, 1990); but, for offsets comparable to the depth to the zone of interest, the regular P-P NMO correction can be used to approximate the P-SV moveout correction, since the difference between P-P and P-SV moveout curves is small. Because these data are synthetic, there is no need for either deconvolution or static corrections, which simplifies the processing. After reversing the polarity of the trailing spread, the data are corrected for geometry, sorted into CCP location, NMO-corrected, muted and stacked. Finally, for display purposes, an automatic gain-control (AGC) function is also applied.

### 3.3 Binning theory

#### 3.3.1 Asymptotic CCP approximation

As an initial attempt at converted-wave binning, the asymptotic value of the conversion-point trajectory was used. This is the slope of the curve at a sufficiently large depth, where it can be assumed that the offset-to-depth ratio approaches zero as shown in Figure 3.1. The general form of the formula for the asymptotic correction is (Eaton et al., 1990):

$$X_p = \frac{X}{1 + \frac{V_S}{V_P}}, \quad (3.1)$$

where  $X_p$  is the offset from the source to the conversion point,  $X$  is the total source-to-receiver offset, and  $V_p$  and  $V_S$  are the shear-wave and compressional-wave velocities. The advantage of this method is that it is not depth-variant and thus each shot-receiver pair requires only one simple calculation to be binned into the proper subsurface location.

### 3.3.2 Depth-variant CCP

To improve on the asymptotic approximation, it is necessary to account for the lateral variation of the conversion point with depth. Tessmer and Behle (1988) have shown that the difference,  $D$ , between  $X_P$  and the source-receiver midpoint satisfies the fourth-order polynomial equation:

$$D^4 + (Z^2 - X^2)D^2 - Z^2kXD + \frac{1}{16}(X^4 + 4X^2Z^2) = 0, \quad (3.2)$$

where  $Z$  is the layer thickness,  $X$  is the source-receiver offset, and

$$k = \frac{1 + \frac{V_S}{V_P}}{1 - \frac{V_S}{V_P}}. \quad (3.3)$$

There are four solutions to this equation, of which only two are real; and of these two, the correct solution satisfies the relation  $D \leq \frac{X}{2}$ . The solution of the exact single-layer formula is used to reposition each sample point in depth to its correct conversion-point location.

### 3.3.3 Dip moveout (DMO)

The method of CCP binning works well for symmetric, flat layers. For the P-P case it is well known that once dipping layers are considered, there is smearing or dispersal of data within CMP gathers, caused by the displacement away from the midpoint of the reflection point (Levin, 1971). Dispersal within a CMP gather causes an increase in the apparent velocity necessary to properly flatten the dipping event, and thus the dipping data are attenuated by stacking (Judson et al., 1978). To avoid this problem, DMO is used to place the reflection in the proper location for dipping data. For the P-P

case, this method has been successfully used for over a decade ever since its introduction in 1978 (Judson et al., 1978).

P-P DMO has recently been extended for use on P-SV data by Harrison (1992). The equations for P-SV dispersal, P-SV apparent velocity, and the P-SV constant-velocity DMO operators are much more complicated than those for the P-P case, and thus will not be discussed in detail as a part of this thesis. However, the method can be summarized as being an algorithm that first constructs the time-domain DMO operator for each input trace, and then sums the operators to get the final DMO result, similar to the integral summation technique for P-P DMO (Deregowski, 1985).

### **3.4 Binning results**

The result of applying CMP binning to P-SV data, without reversing the polarity of the trailing spread, is shown as Figure 3.4a. This is equivalent to treating the P-SV data as P-P data, since P-P data are sorted into the CMP and have no need for polarity reversals. Note that the horizons are not sharp, due to smearing of traces in CMP bins, and that events are not continuous. Next, the polarity of the trailing spread is reversed for the CMP-sorted data (Figure 3.4b). This results in a slight improvement in continuity of the deeper reflectors, but the smearing of traces in CMP bins is still evident, particularly in the shallow section.

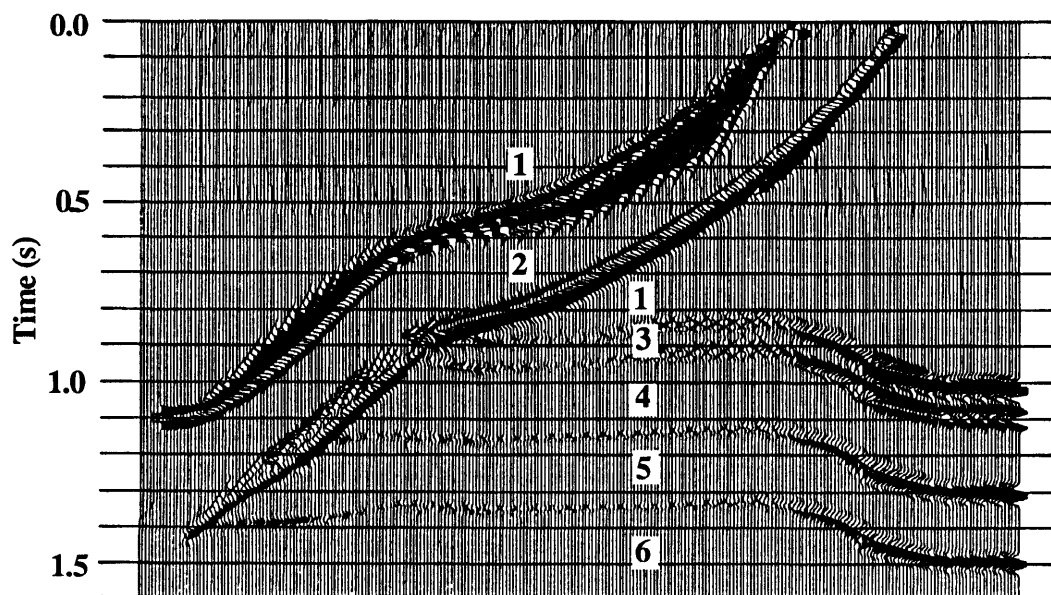
Applying asymptotic CCP binning helps to remove some of the smearing of the CMP bins (Figure 3.5a) and reversing the polarity of the trailing spread of the asymptotic CCP binned data improves the continuity of reflections throughout (Figure 3.5b). However, there are now a few blank traces, observed best on the lower reflectors, due to the irregular distribution of traces in the asymptotic CCP bins (Eaton and Lawton, 1992). Finally, applications of depth-variant CCP binning (Figure 3.6) and DMO (Figure 3.7)

serve to remove the smearing of CCP locations and further improve the continuity of reflections.

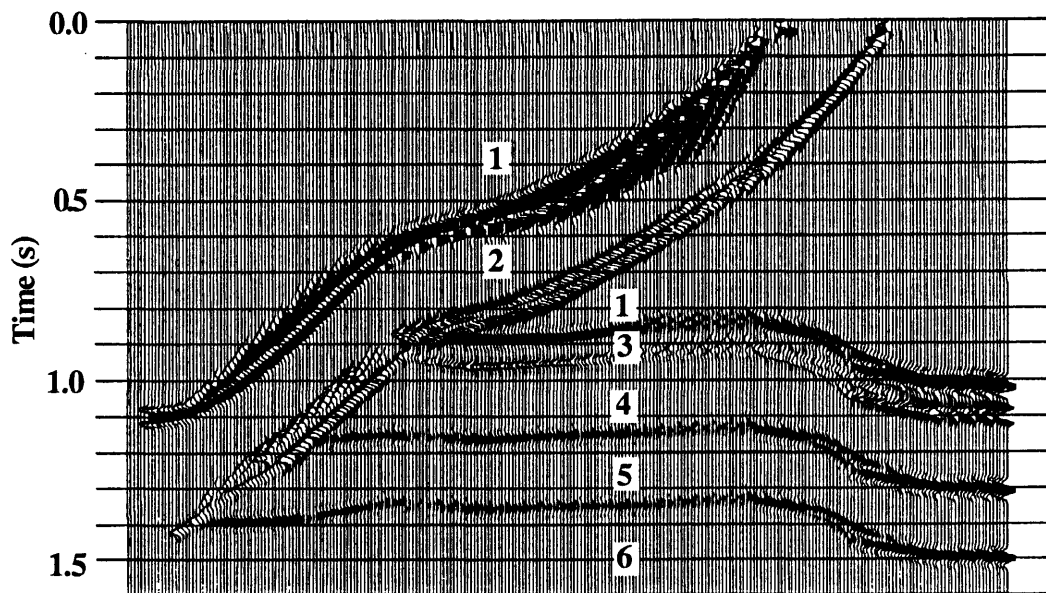
### 3.5 Discussion

As anticipated, there exists a direct correlation between the quality of the solutions and the time invested in obtaining them. The better solutions are obtained by incorporating P-SV DMO and depth-variant binning, which require approximately ten times as much CPU time as CMP binning. These methods also require a more detailed knowledge of the data set, as  $V_p/V_s$  ratios are required as a function of depth. Asymptotic binning assumes a fixed  $V_p/V_s$  ratio with depth and takes the same amount of time as CMP binning, but results in a better stacked section. Choosing the best method of converted-wave binning depends on the amount of dip present, the offset-to-depth ratio of the zone of interest, and the amount of time available. For steeply dipping layers, P-SV DMO is essential to avoid dispersion of CCP bins. For data with an offset-to-depth ratio less than one and with almost no dipoles, asymptotic binning would work well (Eaton et al., 1990). If there is not too much dip and a better solution for the shallow data is desired, then depth-variant CCP binning or P-SV DMO could be used.

For P-SV surface-seismic data, the asymptotic approximation method should be used as an initial estimate of the CCP binning solution. Then, if a better solution is desired, the  $V_p/V_s$  ratios are calculated from transit times of the vertically and radially polarized components and depth-variant binning or P-SV DMO can be used. The P-SV surface-seismic data processed in the remainder of this thesis used the asymptotic method and the method provided good continuity of reflections in the zone of interest. The asymptotic method worked well in these cases, because the data sets have an offset-to-depth ratio for the zone of interest of less than one, and no indications of dip as observed on the vertical-component data.

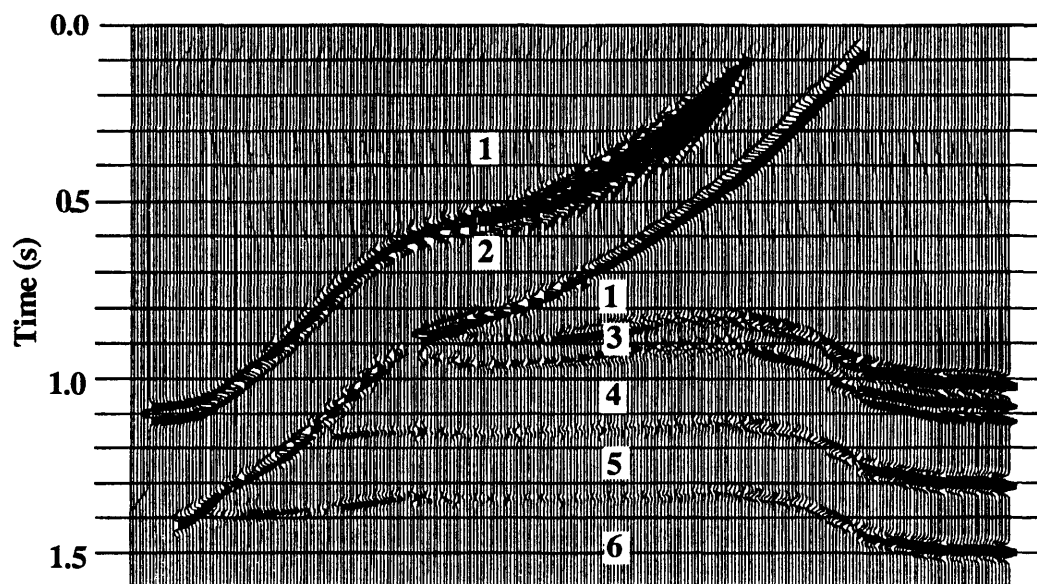


(a)

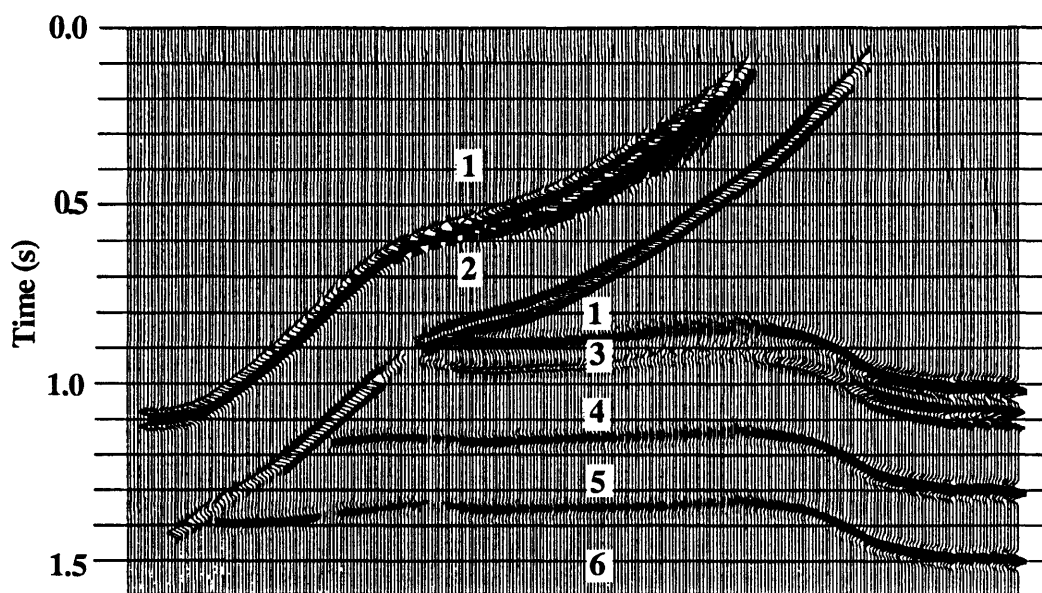


(b)

FIG. 3.4. Highwood Structure P-SV synthetic seismic section using CMP binning:  
 (a) without polarity reversals; (b) with polarity of trailing spread reversed.



(a)



(b)

FIG. 3.5. Highwood Structure P-SV synthetic seismic section using asymptotic CCP binning: (a) without polarity reversals; (b) with polarity of trailing spread reversed.

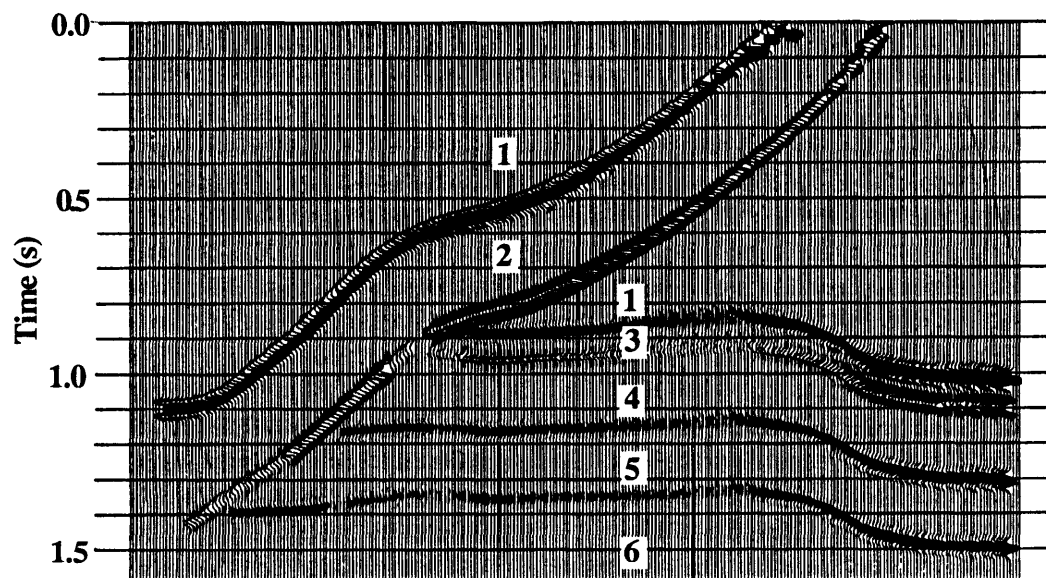


FIG. 3.6. Highwood Structure P-SV synthetic seismic section using depth-variant CCP binning with polarity of trailing spread reversed.

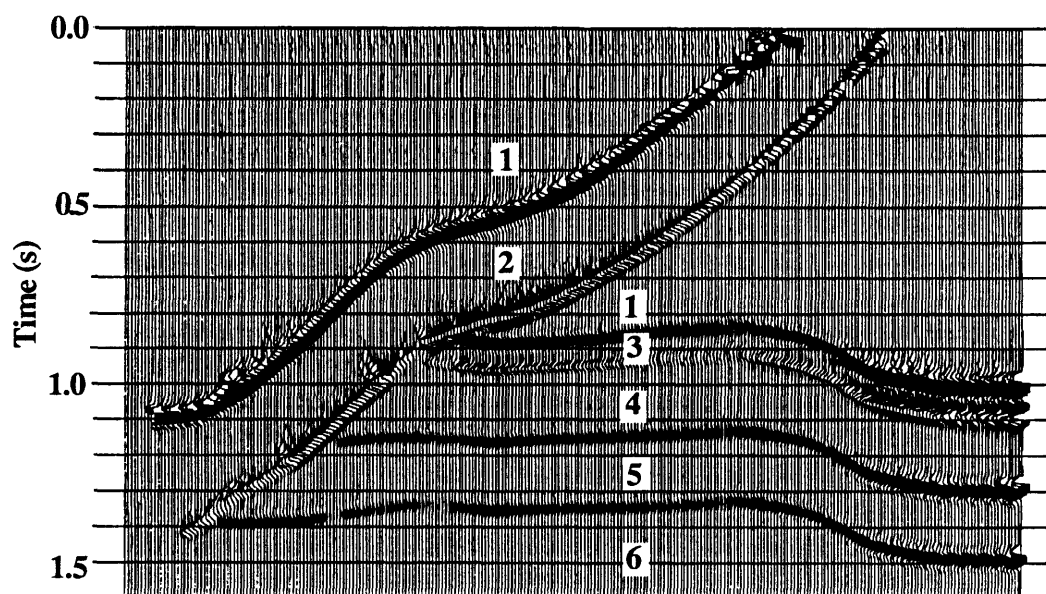


FIG. 3.7. Highwood Structure P-SV synthetic seismic section using P-SV DMO with polarity of trailing spread reversed.

## **Chapter 4 - THREE-COMPONENT SEISMIC DATA PROCESSING: SLAVE LAKE, ALBERTA**

### **4.1 Introduction**

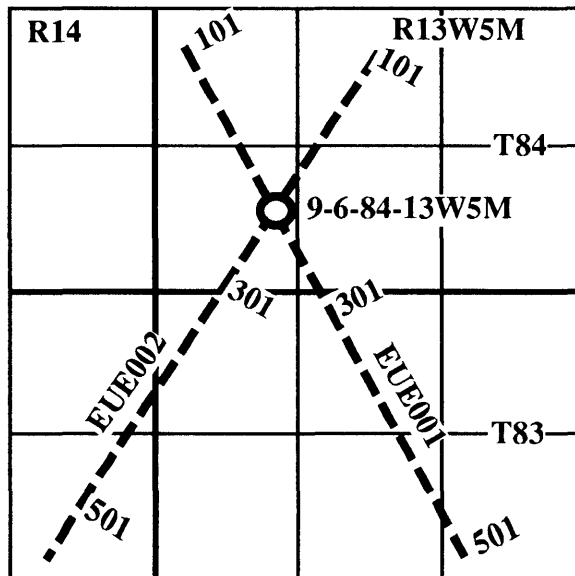
A three-component seismic survey was recorded in the Slave Lake area of northern Alberta (Figure 4.1a) by Petty-Ray Geophysical Canada in March 1988. The data have since been donated to The University of Calgary by Unocal Canada Ltd. This chapter discusses most of the details of the processing of Slave Lake line EUE001, except for static corrections, which are covered in Chapter 5. The zone of interest is the Slave Point and carbonate buildups in the Slave Point are the targets.

### **4.2 Data acquisition**

The field acquisition parameters for the Slave Lake three component survey are summarized in Table 4.1. The survey was shot using 120-trace MDS 10 recording systems with an array of dynamite charges as sources. The shot array consisted of four dynamite charges of one-half kg each, positioned on the corners of a rectangle, with the long side of the rectangle aligned in the direction of shooting of the survey. Instead of the geophone arrays commonly used for conventional (P-P) seismic surveys, single three-component geophones were used for each receiver location. These phones simultaneously record motion in the vertical, radial, and transverse directions. Each of these components was recorded on a separate tape by one of the MDS 10 recorders, resulting in the multicomponent data set. A source interval of 68 m and a group interval of 17 m, with 120 groups, result in a nominal fold of 30.



(a)



(b)

FIG. 4.1. Location map of the Slave Lake survey: (a) inside Alberta; (b) close-up of lines EUE001 and EUE002.

Table 4.1. Acquisition parameters for the Slave Lake survey.

Energy source	Dynamite
Charge size	0.5 kg
Hole Depth	6 m
Source Array	4 over 34 m
Geophone make	PE6
Peak Frequency	10 Hz
Geophone type	PE6, 10 Hz
Geophone array	single phones
Groups recorded	120
Group interval	17 m
Normal source interval	68 m
Near offset	170 m
Recorder type	MDS 10
Amplifiers	IFP
Tape format	SEGB, 1600 BPI
Sample rate	2 ms
Record length	3 s
Low cut filter	Out
Antialias filter	125 Hz@72 dB
60 Hz notch filter	Out

Line EUE001 was shot starting with an end-on spread until station number 369. Then the spread remained fixed from station 382 to 501 while the source moved through the spread until the last shot at station 501 (Figure 4.1b). This change in recording method resulted in differences in the fold and range of offsets as station numbers increased. The effect of this on the seismic sections will be discussed later in this chapter.

Examples of end-on (SP101) and split-spread (SP437) shot gathers are shown in Figures 4.2 to 4.4 for the vertical, radial, and transverse components, respectively. All of these gathers have had an RMS gain function applied to them, so that deeper events would be easily visible. Several events are labelled on the shot gathers and their interpretation will be explained in the discussion section of this chapter.

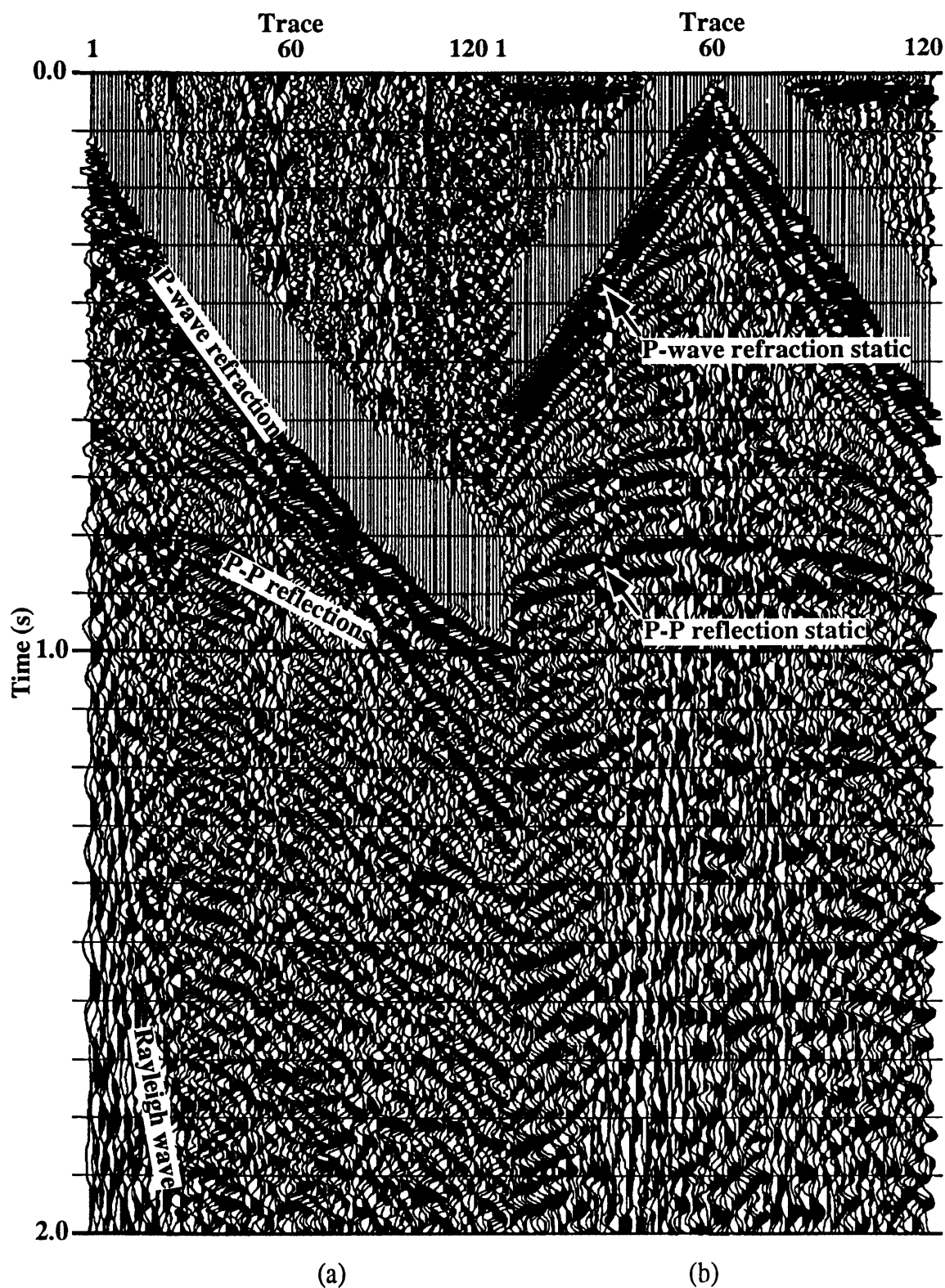


FIG. 4.2. Sample shot record from the vertical-component (P-P) data from Slave Lake for shots located at: (a) station 101; (b) station 461.

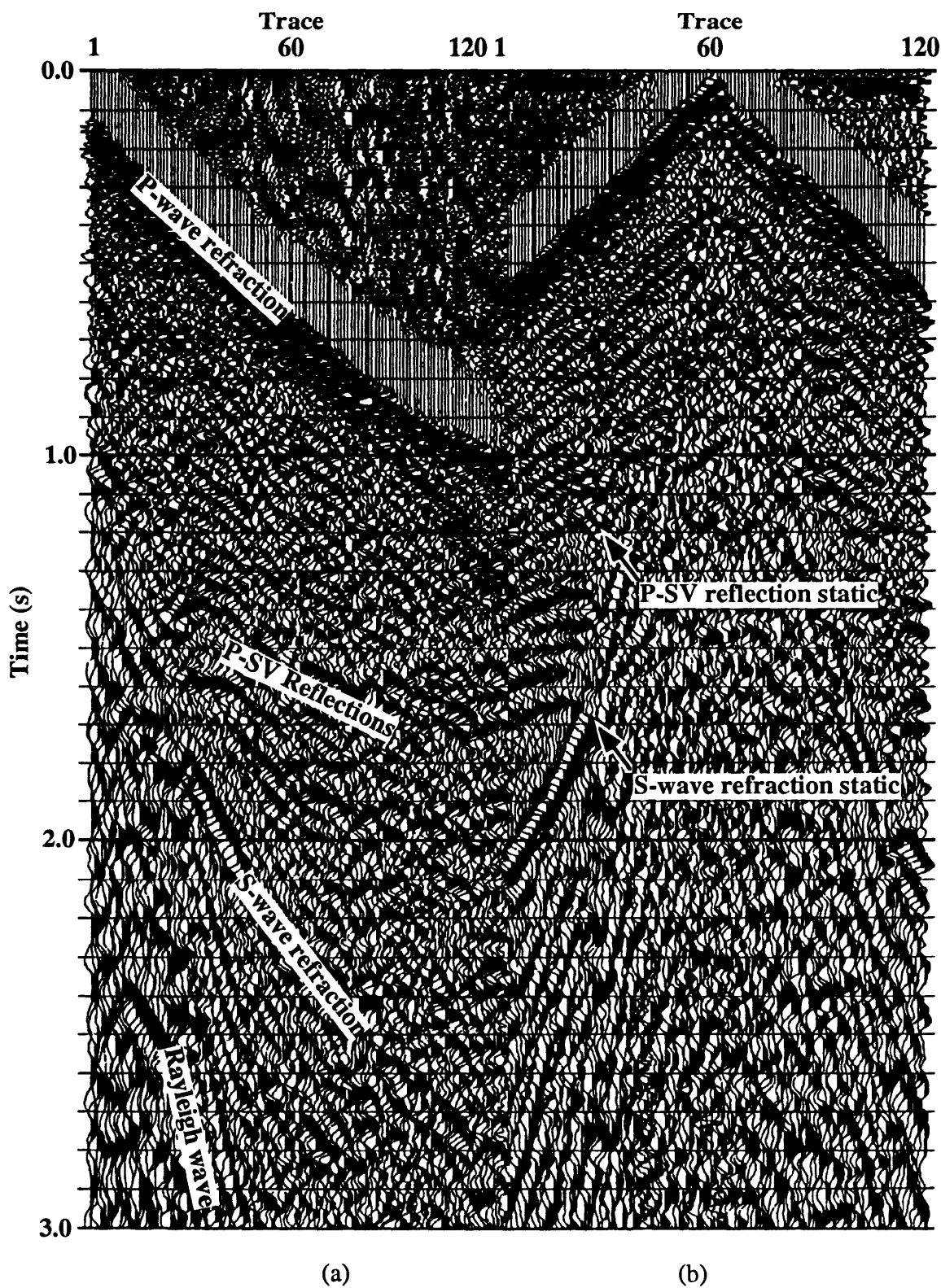


FIG. 4.3. Sample shot record from the radial-component (P-SV) data from Slave Lake for shots located at: (a) station 101; (b) station 461.

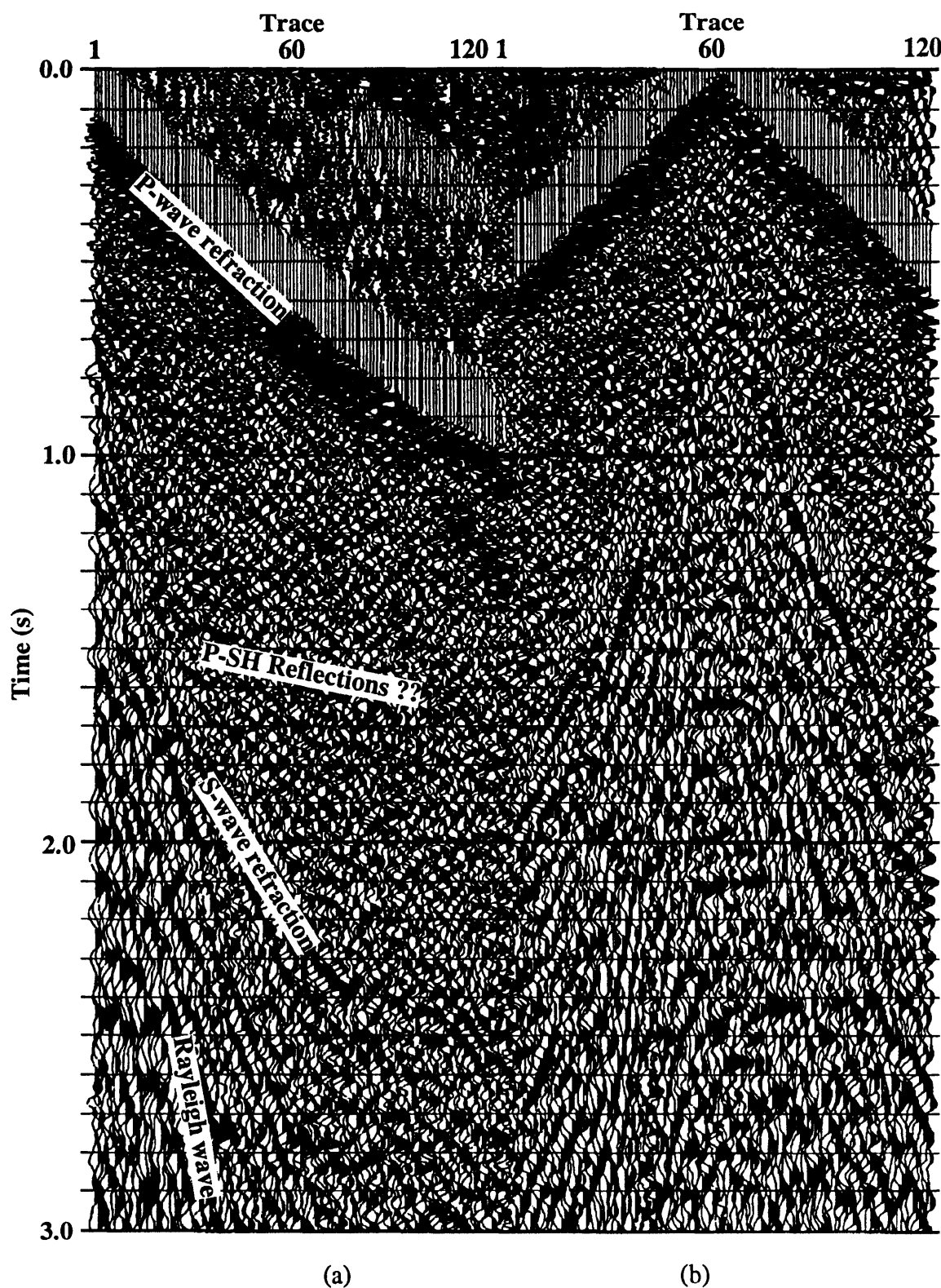


FIG. 4.4. Sample shot record from the transverse-component (P-SH) data from Slave Lake for shots located at: (a) station 101; (b) station 461.

### 4.3 Data Processing

Processing of a three-component data set normally starts with the processing of the vertical channel. The vertical channel records vertically-polarized ground motion, just as a conventional (P-P) survey would, and thus the processing flow used is the same. The processing flow for the vertical channel, along with the processing parameters used, is outlined in Table 4.2.

Table 4.2. Processing sequence and parameters for the vertical-component data.

DEMULTIPLEX  
 GEOMETRIC SPREADING COMPENSATION  
 SPIKING DECONVOLUTION  
     100 ms operator, 0.1% prewhitening  
 CMP SORT  
 ELEVATION & REFRACTION STATIC CORRECTION  
 INITIAL VELOCITY ANALYSIS  
 AUTOMATIC SURFACE-CONSISTENT STATIC CORRECTION  
     Correlation window of 450 to 1100 ms  
     Maximum shift of  $\pm 20$  ms  
 VELOCITY ANALYSIS  
 NORMAL MOVEOUT CORRECTION  
 MUTE  
 CMP TRIM STATIC CORRECTION  
     Correlation window from 400 to 1200 ms  
     Maximum shift of  $\pm 10$  ms  
 STACK  
 BANDPASS FILTER  
     Zero-phase, 12-65 Hz  
 RMS GAIN  
     First window of 300 ms, second of 400 ms,  
     subsequent windows of 800 ms

As explained in Chapters 2 and 3, processing of the radial component requires several modifications from the processing of the vertical component. The processing flow used for the radial component, along with the corresponding parameters, is shown in Table 4.3.

Table 4.3. Processing sequence and parameters for the radial-component data.

DEMULTIPLEX  
 GEOMETRIC SPREADING COMPENSATION  
 SPIKING DECONVOLUTION  
     120 ms operator, 0.1% prewhitening  
 REVERSE THE POLARITY OF TRAILING SPREAD  
 FINAL P-WAVE STATIC CORRECTION  
 INITIAL VELOCITY ANALYSIS  
 HAND STATIC CORRECTION FROM SURFACE STACKS  
 AUTOMATIC SURFACE-CONSISTENT STATIC CORRECTION  
     Correlation window from 600 to 1700 ms  
     Maximum shift of  $\pm 25$  ms  
 CMP STACK  
 CCP REBINNING  
      $V_p/V_s$  of 1.95 used  
 VELOCITY ANALYSIS  
 NORMAL MOVEOUT CORRECTION  
 MUTE  
 STACK  
 BANDPASS FILTER  
     Zero-phase, 7-35 Hz  
 RMS GAIN  
     First window of 300 ms, second of 600 ms,  
     subsequent windows of 900 ms

ITA's interactive velocity analysis program, "VAN2", is used to estimate the stacking velocities from velocity-semblance plots (Figures 4.5 and 4.6). The semblances are created from NMO-corrected, muted, and NMO-uncorrected common-offset stacked sections (Figures 4.5 and 4.6). The maximum semblance at each time, relative to the maximum semblance of the entire plot, is shown in Figure 4.5c and 4.6c. The stacking velocity functions are then picked from the semblance plots using a mouse on a Sun workstation. The velocity analysis program also has two other menus: the "STAK" menu and the "NMO" menu. These menus are used to check the effect that changing the velocity function has on stacked data, and to pick a mute function from NMO-corrected gathers, respectively. Examples of NMO-corrected constant-offset stacked gathers, with the mute function outlined are shown as Figure 4.7.

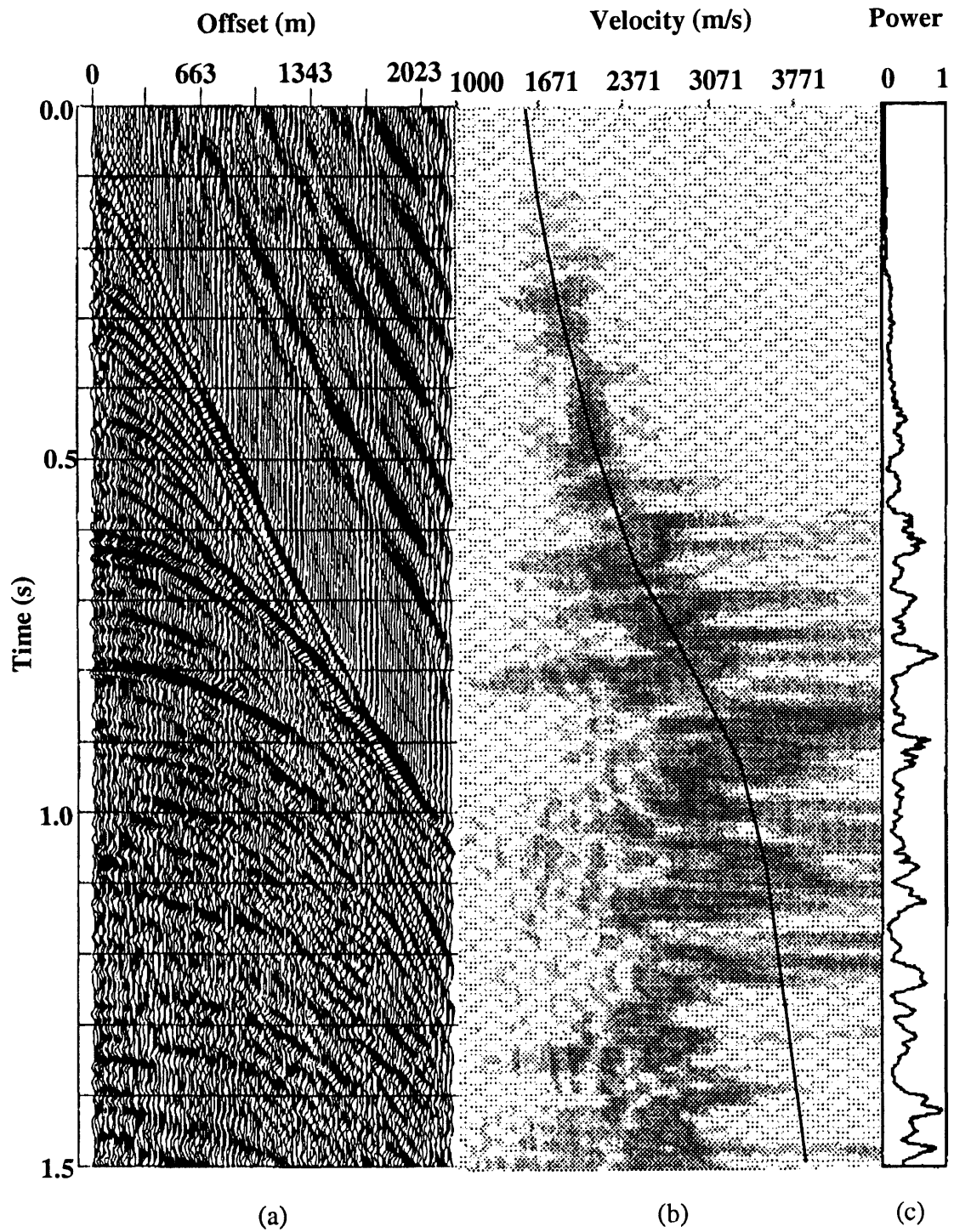


FIG. 4.5 Sample velocity-analysis plots for the vertical component of line EUE001: (a) common-offset stacked section; (b) semblance-analysis plot; (c) stack power.

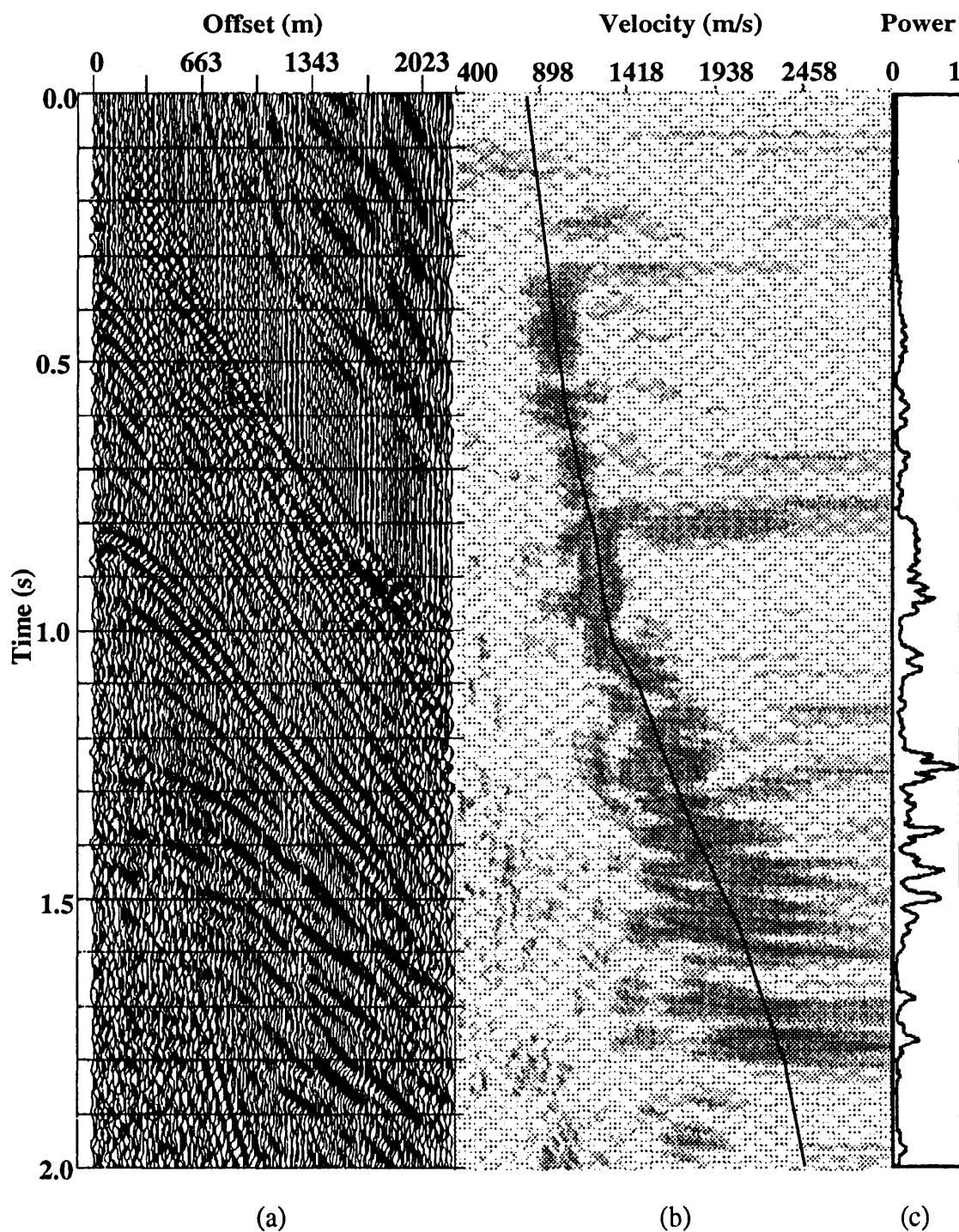


FIG. 4.6 Sample velocity-analysis plots for the radial component of line EUE001: (a) common-offset stacked section; (b) semblance-analysis plot; (c) stack power.

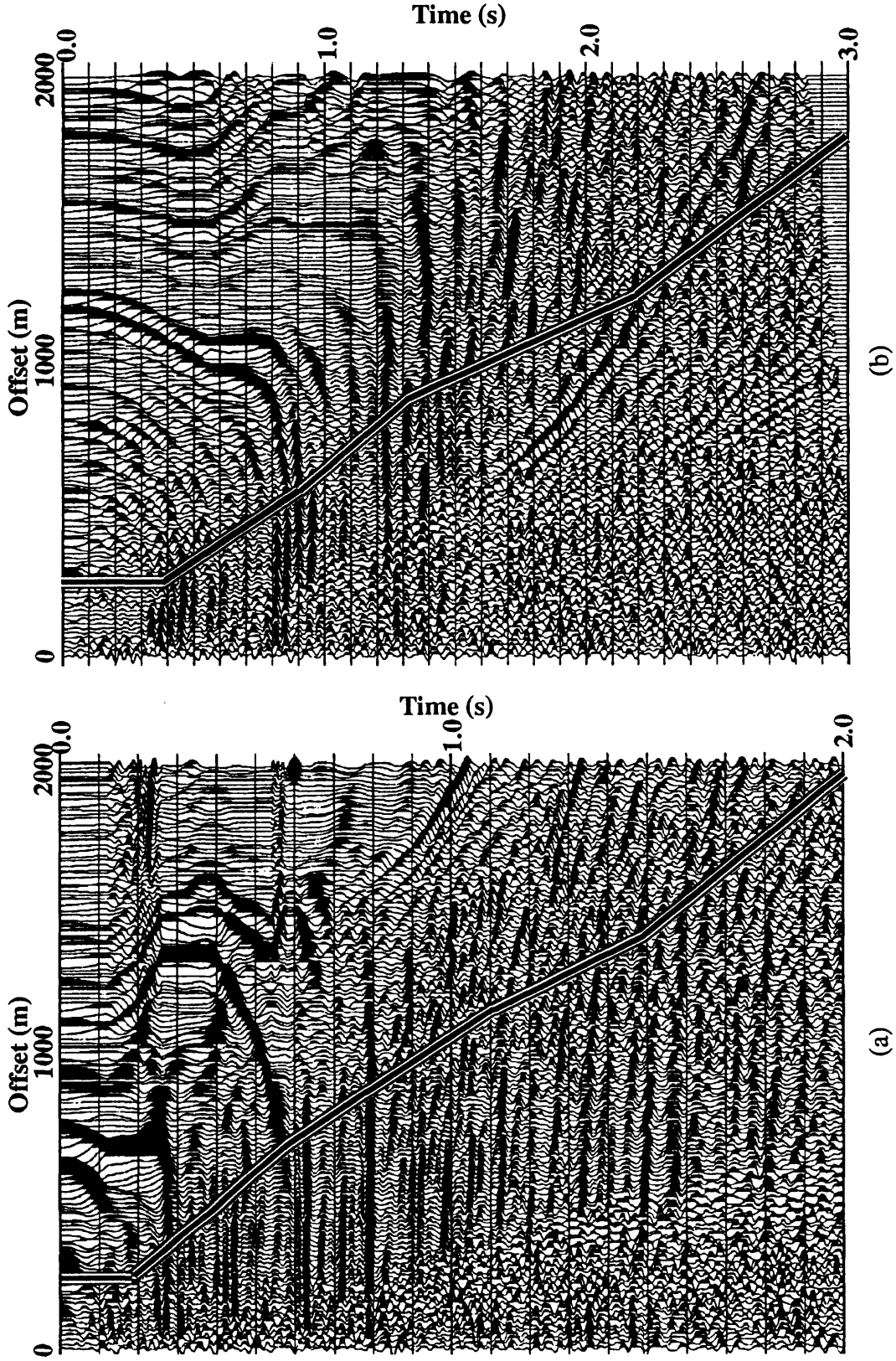
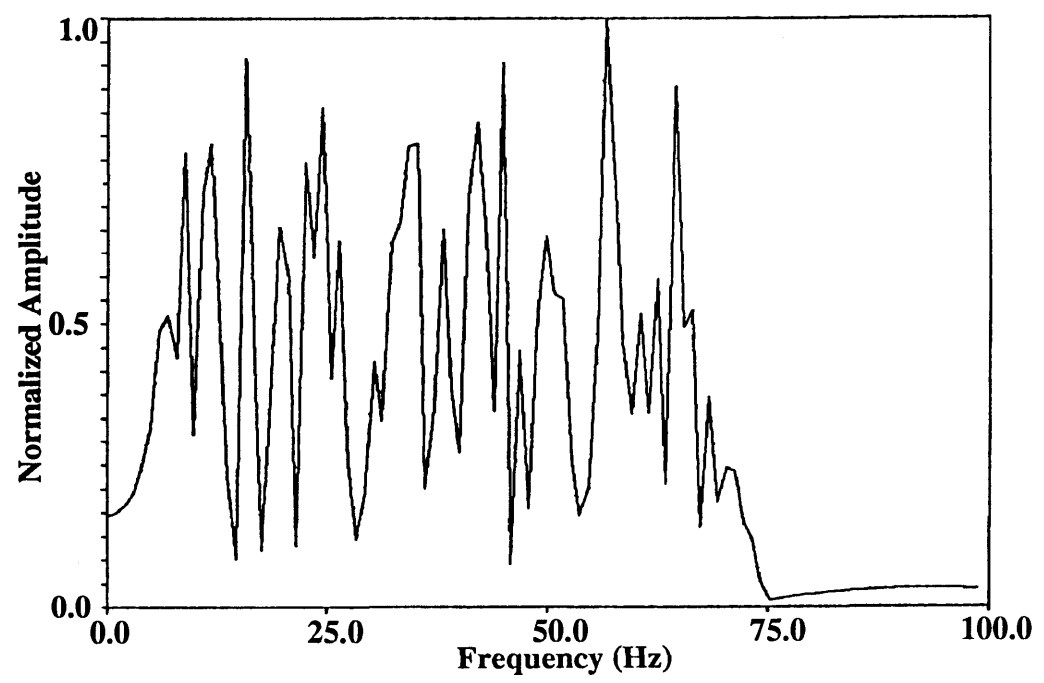
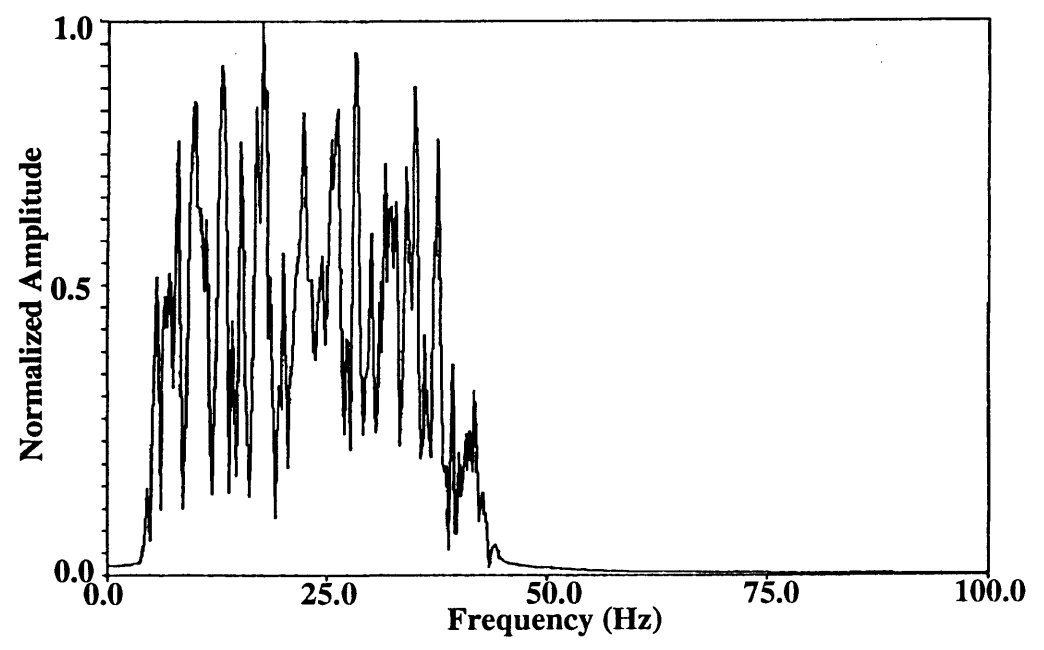


FIG. 4.7. NMO-corrected constant-offset stacked gathers showing the mute functions used: (a) P-P; (b) P-SV.



(a)



(b)

FIG. 4.8. Amplitude spectra from fast Fourier transformation of ten adjacent traces: (a) P-P; (b) P-SV.

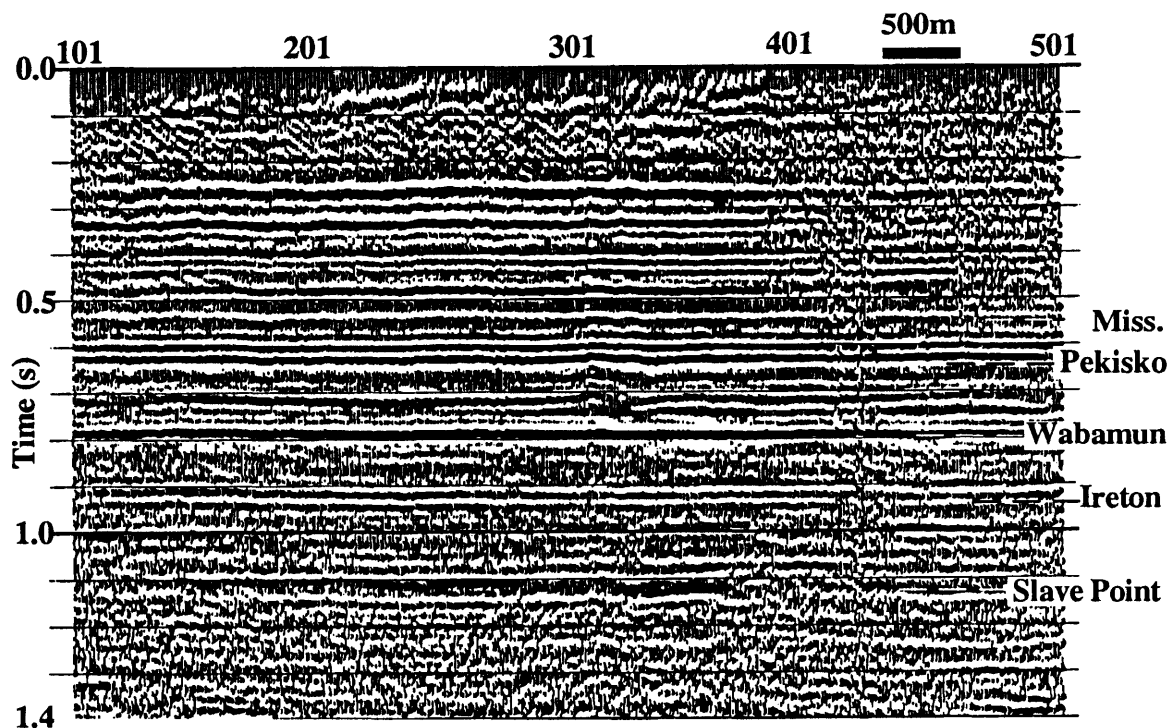
Amplitude spectra were created using the fast Fourier transform of ten adjacent traces from shot records (Figure 4.8). These spectra indicated that the majority of the energy was contained between 10 and 65 Hz for the vertical component and between 8 and 40 Hz for the radial component. This information, combined with band-limited bandpass filter panels was used to obtain the bandpass filter parameters to be applied to the data.

The final stacked sections for vertical and radial components of line EUE001 of the Slave Lake survey are shown as Figure 4.9. The data quality of the transverse component does not allow any in-depth processing to be attempted. However, using the parameters derived from the radial component, a stacked section for the transverse component is created (Figure 4.10). All of these sections have the hand-picked final static corrections applied, discussed in Chapter 5, as well as a mild  $f$ - $k$  filter with a pass-band of  $\pm 2$  ms/trace for the vertical component and  $\pm 3$  ms/trace for the radial component data sets, with a 6-dB maximum reject.

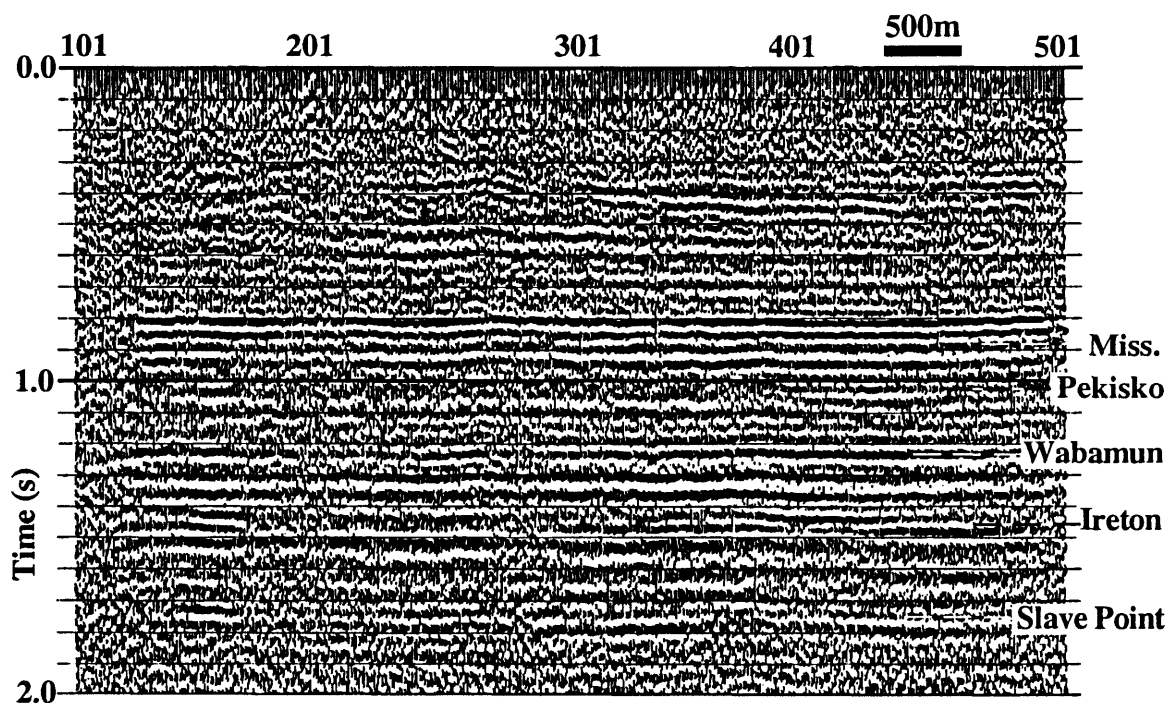
The final receiver static solutions are shown as Figure 4.11. Refraction and residual static corrections were applied to the vertical component, while hand-picked and residual static corrections were applied to the radial component. These static correction methods as well as several others will be discussed in Chapter 5.

#### **4.4 Discussion**

The vertical-component records (Figure 4.2) contain a linear, high-energy event originating from the source with a velocity of 340 m/s. This event is likely a Rayleigh wave. This can be inferred due to the close relation between the velocity of this event and the velocity of the uppermost layer and the dispersion of the event. P-wave refractions with a velocity of 1200 m/s are also visible on the vertical component.



(a)



(b)

FIG. 4.9. Final stacked sections from line EUE001 with poststack  $f$ - $k$  filter applied: (a) P-P; (b) P-SV.

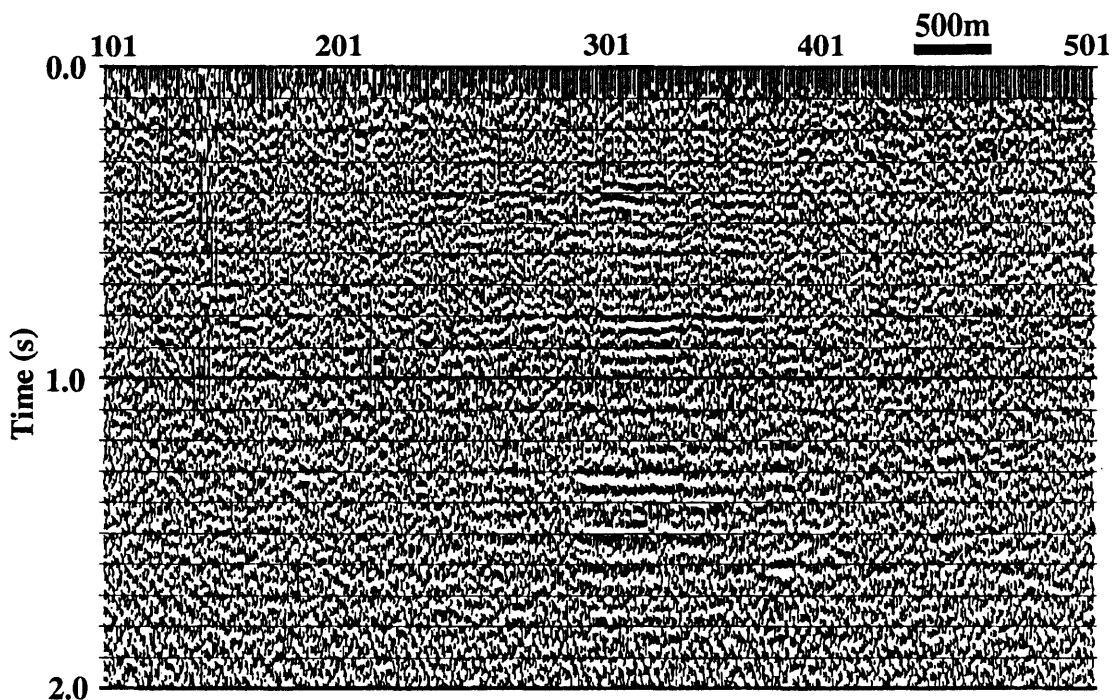


FIG. 4.10. Final stacked section of the transverse component from line EUE001 with poststack  $f-k$  filter applied.

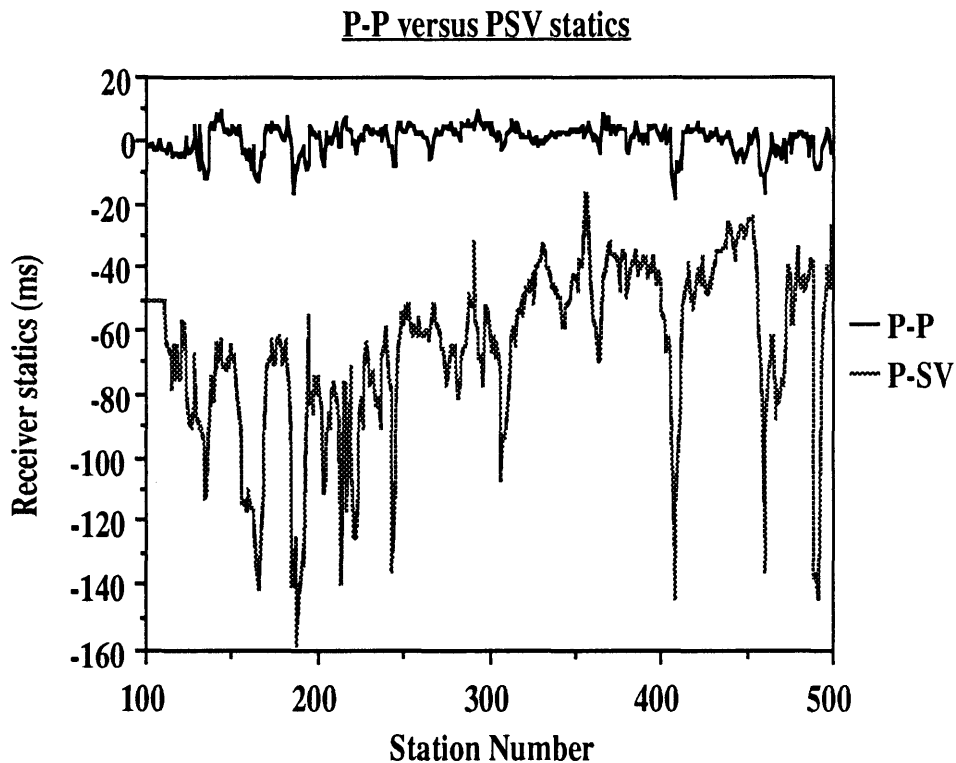


FIG. 4.11. Final receiver static solutions for the vertical component (P-P) and the radial component (P-SV) from line EUE001.

The radial-component records (Figure 4.3) contain an event that extends from 1.3 second at the near offsets to 2.8 seconds at the far offsets. This event is interpreted as an S-wave refraction for several reasons. This refracted S-wave event indicates that several layers are present, with velocities that correspond well with S-wave near-surface models from other P-wave and S-wave surveys in Alberta (Lawton, 1990). Further, notice that static pockets present on the P-SV reflections correspond with those on the S-wave refraction, in the same way that static pockets on the P-wave reflection correspond to those on the P-wave refraction, and that these static pockets are much larger than the P-wave static pockets. Further, the S-wave refraction is not likely to be a Rayleigh wave, commonly called 'ground roll', since it does not appear on the vertical channel (Figure 4.2). Rayleigh waves are polarized in the  $xz$ -plane, having retrograde elliptical particle motion from the inline horizontal (or radial) to the vertical direction. Hence, Rayleigh waves would appear on both the vertical and the radial channels. Finally, the possibility of this event being a Love wave is ruled out by the fact that Love waves should be seen only on the transverse channel, whereas the event under consideration is predominantly observed on the radial channel.

While the presence of a shear-wave refraction would usually be considered as noise, it can be quite useful if it can be picked and used for S-wave refraction static correction analysis, as P-wave refractions are used for P-wave refraction static correction analysis. Picking the S-wave refraction was attempted on this data set and the result is discussed in Chapter 5.

The radial-component records (Figure 4.3) have good signal strength, and contain events that roughly correspond to those on the vertical component (Figure 4.2). However, the peak frequency is obviously decreased, and the static pockets are vastly increased. The transverse-component records (Figure 4.4) do not have many noticeable reflections that correspond to those on the radial component and appear to consist mostly of noise.

For this reason, the transverse component was not processed as a separate component, and instead, the final radial-component parameters were used to obtain a stacked section for the transverse component (Figure 4.11).

From the velocity-analysis plots for line EUE001 (Figure 4.5 and 4.6), some contamination of one component by the other component is observed. This is apparent on the vertical component (Figure 4.5) where low-velocity converted-wave energy is present below the P-wave velocity profile, and on the radial component (Figure 4.6) where high-velocity P-wave energy is present above the P-SV velocity profile.

The final receiver static solutions (Figure 4.11) for the vertical and radial components clearly demonstrate the difference in magnitude, as well as the lack of correlation between the P-P and P-SV static solutions. The large, high lateral frequency static shifts on the vertical component complicate any static correction analysis, as discussed in Chapter 5.

While the lower velocities of the radial component would allow for greater vertical resolution with the same frequency bandwidth, the amplitude spectra for Slave Lake (Figure 4.8) indicate that the radial component bandwidth is only half of the vertical component. With half of the bandwidth, and the ratio of P to P-SV velocities being about two-thirds, assuming a  $V_P/V_S$  ratio of 2.0, the vertical resolution of the radial component will be approximately three-quarters of the vertical resolution of the vertical component.

The final stacked sections for the vertical and the radial components of Slave Lake line EUE001 (Figure 4.9) both have reasonable coherence of reflections. The radial-section, like the vertical-section, has continuous reflections, but has lower frequencies and more noise. The transverse-section (Figure 4.10) is mostly noise, with only a small portion of coherent reflections apparent in the middle of the line. Birefringence analysis of the portion of the transverse data that has coherent signal could be used to estimate the birefringence or preferred orientation of the coordinate system. This is accomplished by

using the cross-correlations between the radial- and the transverse-component field records to calculate the natural-coordinate-system angle and the time lag between the two components (Harrison, 1992). Rotating the horizontal components into the natural-coordinate-system angle would serve to properly position the components into the fast S wave and slow S wave directions. The lack of signal on the transverse component might indicate that line EUE001 is oriented in the preferred orientation of the coordinate system. This hypothesis could be tested by examining the other line in the survey, line EUE002, which is oriented at 60 degrees to line EUE001. If birefringence analysis of line EUE002 gives a natural-coordinate-system angle of 60 degrees, then the preferred orientation of the coordinate system is most likely 60 degrees. However, if this analysis obtains an angle of close to zero or if there is no signal on the transverse component of line EUE002, then the lack of S-wave splitting in the area would indicate that there is no S-wave anisotropy in the area.

## Chapter 5 - P-SV STATIC CORRECTION

### 5.1 Introduction

S waves experience much larger static shifts due to the near surface than P waves, causing static correction problems in converted-wave sections to be more prevalent than P-wave static correction problems. Usually, in the processing of the radial channel, it has been necessary to hand-pick the CRP-stacked sections before any further residual static correction analysis could be performed. Since refraction static correction methods have long been used on compressional seismic data, it is only natural to attempt to use refraction methods on converted-wave data also. P-wave refraction methods remove static shifts by first accounting for elevation differences and then analyzing P-wave refractions to obtain a model with thicknesses and velocities of the near-surface layers (Gardner, 1939). This model is then used to determine the shift in traveltime of the raypath relative to a chosen datum plane. Similarly, shear-wave refractions can be used to give a model of the near surface (Lawton, 1990), and thus help to solve for static shifts on converted-wave data. To automate the procedure for P-SV static correction analysis, residual static correction methods have been applied to P-SV data with varying degrees of success. Attempts to apply surface-consistent residual static correction estimation by stack-power maximization (Ronen and Claerbout, 1985) to P-SV data have failed due to their inability to find a local maximum and due also to cycle-skipping. By modifying the optimization function and considering only the receiver static correction, Cary and Eaton (1993) have obtained good results using their CRP stack-power optimization method. A review of the various static correction methods available for use on P-P data was compiled by Russell (1989) and again by Marsden (1993a, b, and c). The objective of this chapter is to compare the result of applying these static correction methods to converted-wave field data, the radial component of Slave Lake line EUE001.

## 5.2 Hand-picked static correction

If the near-surface, shear-wave velocity structure could be approximated by assuming a  $V_P/V_S$  ratio of two, then applying twice the final P-wave static solution from the vertical-component to the radial-component receivers would give a good P-SV static solution. However, the ratio of P-wave velocity to S-wave velocity is not constant throughout the seismic section (Lawton, 1990; Watrus, 1989), and is particularly variable in the near surface (Figure 5.1). Thus, it is necessary to separate the data into common source point (CSP) stacked sections (Figures 5.2 and 5.3) and common receiver point (CRP) stacked sections (Figures 5.4 and 5.5) to pick the static shifts for each section separately. Both of the CSP-stacked sections for the vertical and radial components (Figures 5.2 and 5.3) consist of P waves and thus are expected to have the same static shifts. However, the CRP-stacked section for the radial component (Figure 5.4b) consists of S waves, while the vertical component (Figure 5.2b) consists of P waves and the static shifts are not expected to be similar. The CRP-stacked section for the radial component data (Figure 5.4b) does indeed have much larger static shifts than the vertical component (Figure 5.4a), while the corresponding CSP-stacked sections have static shifts of similar magnitudes (Figures 5.2 and 5.3).

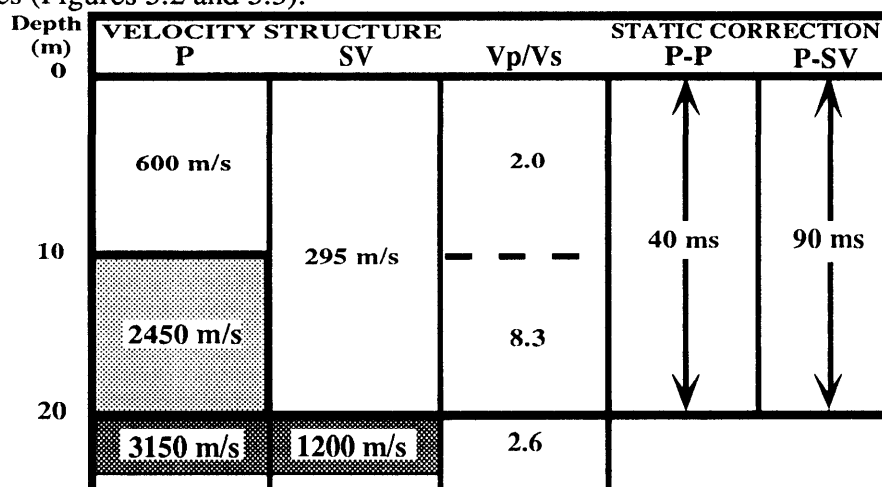


FIG. 5.1. Near-surface P-wave and S-wave velocity structures from Jumping Pound, Alberta (from Lawton, 1990).

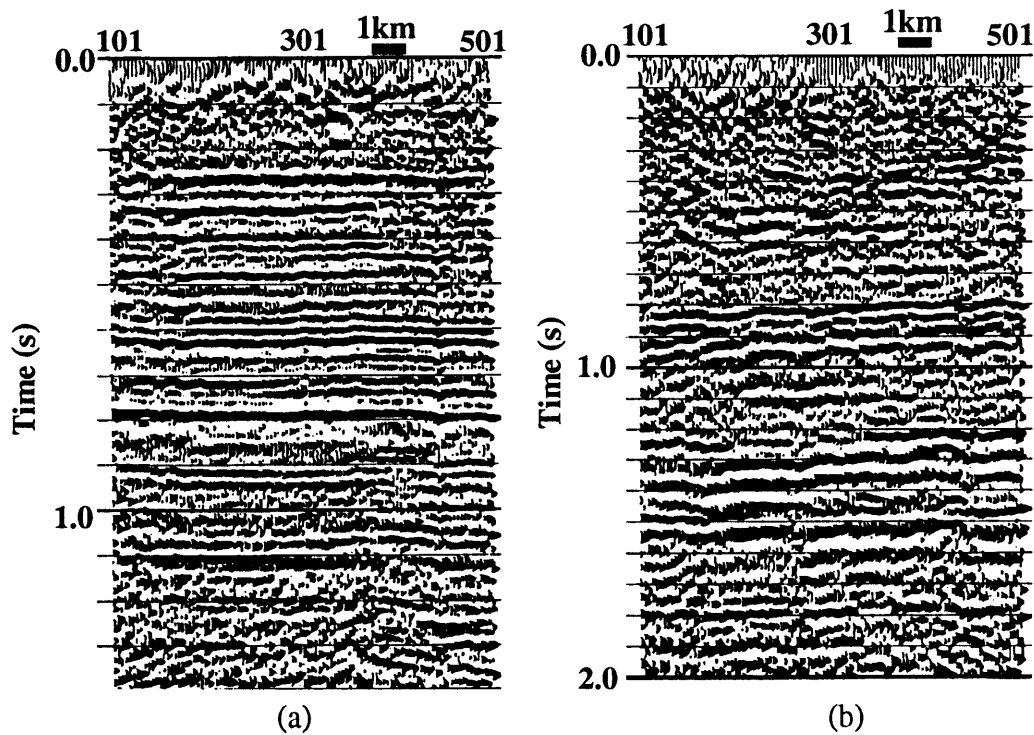


FIG. 5.2. CSP-stacked sections without any static-corrections applied: (a) (P-P); (b) (P-SV).

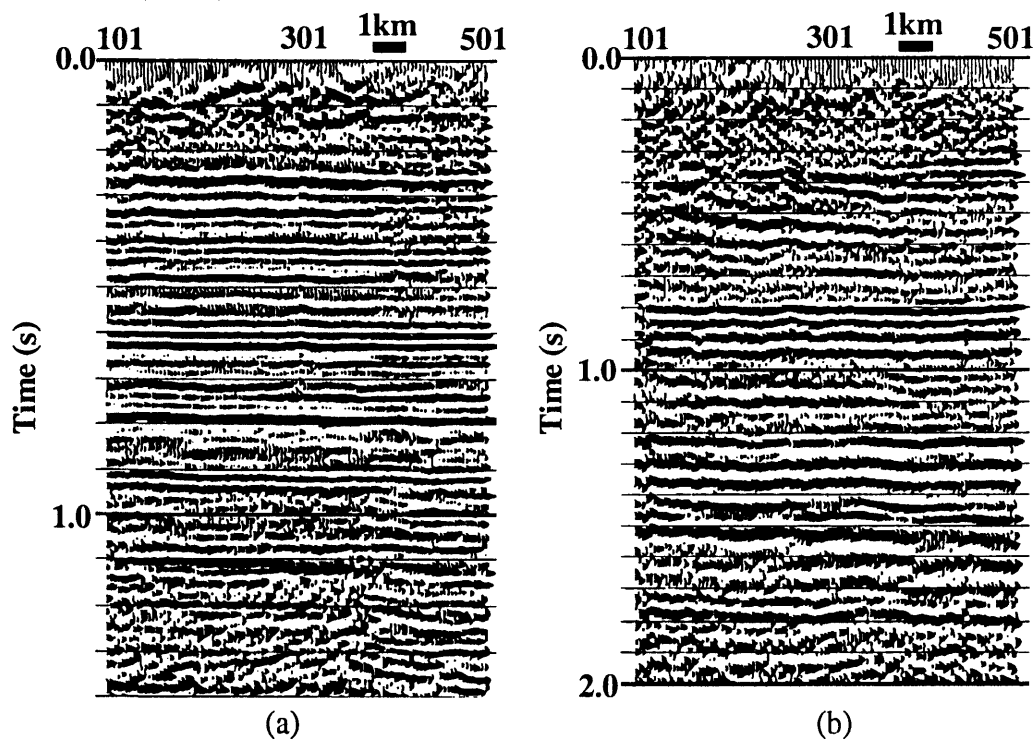
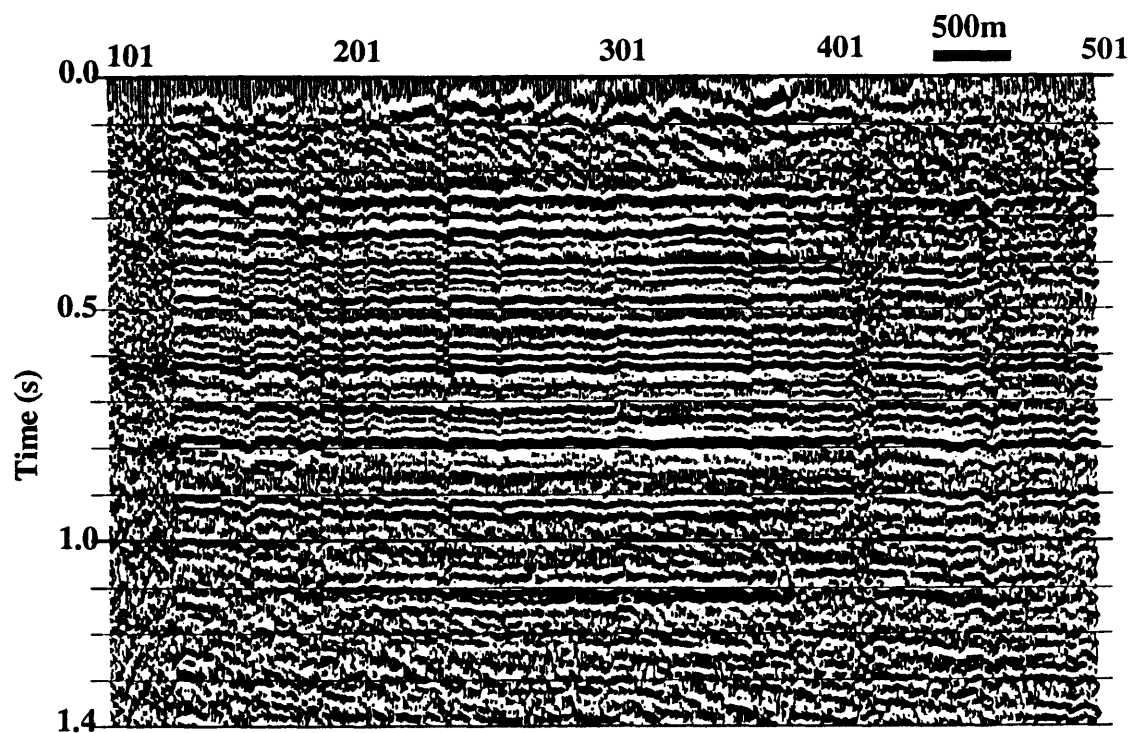
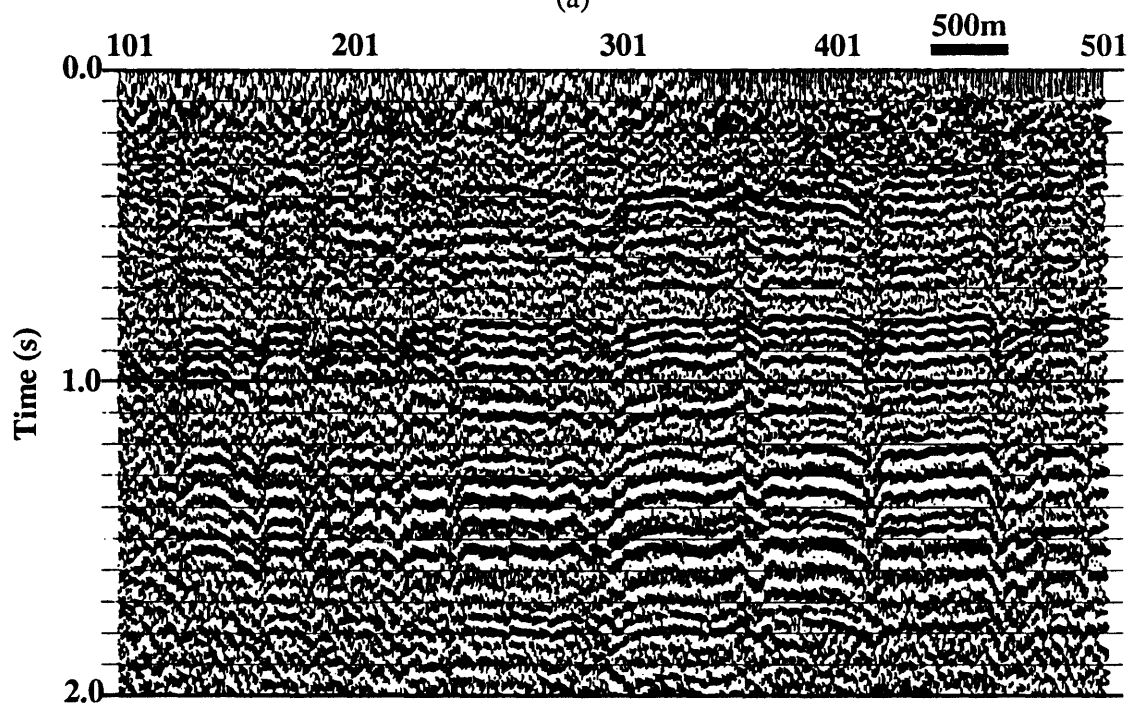


FIG. 5.3. CSP-stacked sections with hand-picked and residual static-corrections applied: (a) P-P; (b) P-SV.



(a)



(b)

FIG. 5.4. CRP-stacked sections without any static-corrections applied: (a) P-P; (b) P-SV.

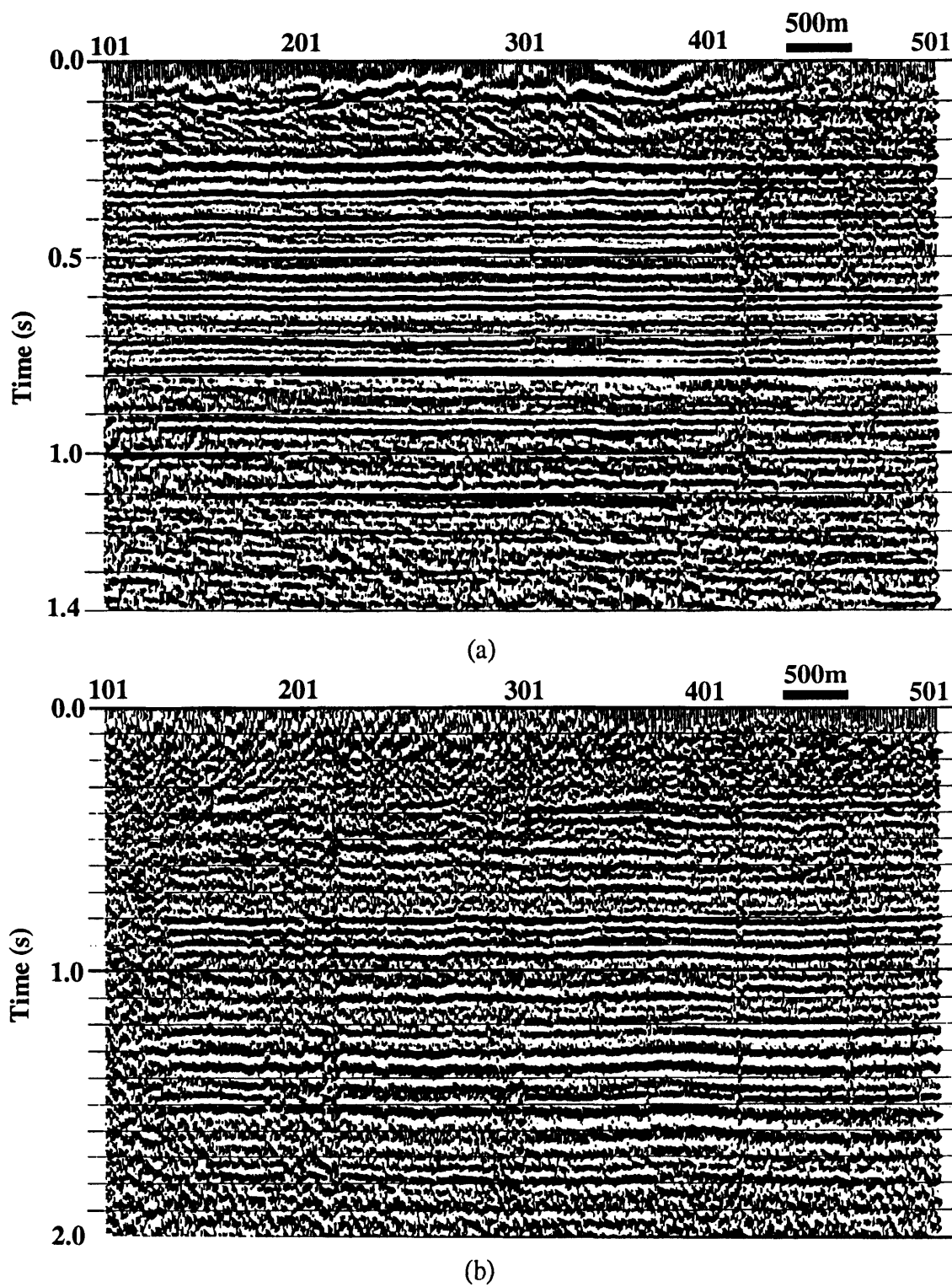


FIG. 5.5. CRP-stacked sections with hand-picked and residual static-corrections applied: (a) P-P; (b) P-SV.

Since the static shifts on the CRP-stacked section for the vertical component (15 ms) are not as large as those for the radial component (100 ms), it was possible to successfully apply automatic residual static corrections to the vertical component, but not to the radial component. The automatic residual static correction programs used were Western Geophysical's "MISER" program, and ITA's "SUPER" program, which are both surface-consistent residual static correction programs. These residual static correction programs failed on the radial component due to a phenomenon known as cycle-skipping, where the wrong cycle of a seismic trace is accepted as the correct one since it results in a smaller time shift and still results in a high stack power. If the automatic programs fail, then the static shifts have to be picked by hand. A solution of the receiver static corrections is obtained from hand-picking of the CRP-stacked section and applied back to the CRP-stacked section to check the result until a satisfactory solution is obtained. To obtain the final static solution (Figure 5.5b), this process was iterated three times, followed by one pass of ITA's residual static correction program. The final stacked section after application of the hand-picked and residual static solutions has good signal continuity with considerably fewer static shifts remaining (Figure 5.5b).

### **5.3 Refraction methods**

In Chapter 4, a high-energy, low-velocity event was observed on the radial component (P-SV) shot records, which was identified as a shear refraction. The existence of shear refractions on compressional-source seismic data may appear to be questionable since, theoretically, very little shear energy is generated by a perfectly spherical explosion. However, it is possible for compressional waves to convert to shear waves close to their generation point, then to travel as shear waves back to the receiver. In this manner, refracted waves result which are close to being entirely shear-wave refractions. To obtain the shear-wave static solution, it is assumed that the refractions observed are

indeed true shear refractions and that the traveltime as a compressional wave can be ignored. The justification for not considering the P-wave part of the refractions is that the traveltime as a P wave is minimal compared to the traveltime as a shear wave due to the shorter distance travelled and higher velocity of the P-wave component.

The S refraction discussed in Chapter 4 is picked and used to obtain an S-wave refraction static solution in the same way that P refractions have been used to obtain a P-wave refraction static solution. A full refraction static solution for converted-wave data involves using the source terms of the compressional-wave refraction static solution combined with the receiver terms of a shear-wave refraction static solution. The P-wave refraction static solution has already been determined in the processing of the vertical channel. Therefore, it is simply necessary to separate the source terms from the receiver terms and to apply the P-wave source terms to the radial channel. The receiver terms from the S-wave refraction static solution are then added to the radial component to complete the P-SV refraction static solution. Computer picking of the S refraction is theoretically possible, but fails because the S refractions are masked by major P-SV reflections, whereas P refractions always precede P-P reflections. The S refractions, therefore, were picked on an interactive workstation. This is rather time-consuming since the full data set must be stored in order to pick the S refractions, since the S refractions almost cover the full range of zero to three seconds.

To obtain a static solution from the refractions, a refraction static correction program must be used. There are several options available to accomplish this, including the slope/intercept method (Gardner, 1939, 1967), delay-time method (Barry, 1967; Lawton, 1989), and some form of an inversion routine (Palmer, 1980; Hampson and Russel, 1984; de Amorim, et al., 1987; Boadu, 1988). For this data set I have chosen to use the time-difference method (Lawton, 1989) and Western Geophysical's Extended Generalized Reciprocal Method (EGRM) refraction static correction program (Diggins et

al., 1988). The refraction static correction programs derive the Earth models using the traveltimes of the refractions, from which static shifts can be calculated. Since the radial channel records converted waves that travel as P waves from the source to the reflector but travel as SV waves to the receivers, the P-wave source static solution and the shear-wave receiver static solution should be applied to the radial-component data. Thus, only the receiver components of the shear-refraction static solution are applied to the radial-component data. Similarly the source terms of the P-wave static solution are applied to the data to compute the refraction static solution for converted waves on the radial-component data.

### 5.3.1 Time-difference refraction static correction

Time-difference refraction static correction uses time-differences, or delay times, at shots and receivers to find the velocities and thicknesses of the refractors (Lawton, 1989). This method is similar to the delay-time method (Barry, 1967), except that it uses time differences, which are really the 'generalized half-intercept time', as introduced by Palmer (1980). The primary advantage of this method is that it does not require the common receiver to lie between the two shotpoints, therefore forward and reverse spreads are not required, as they are for the reciprocal methods (Barry, 1967).

From Lawton (1989), the delay time at shotpoint  $k$ , for difference window  $n$ , is given by

$$t_d(k)_n = \frac{1}{j_{\text{tot}}} \sum_{j=1}^{j_{\text{tot}}} \frac{t_{j,k} - \delta t_{j,k}}{2}, \quad (5.1)$$

where 'time-difference windows' are defined as the zones over which common receivers involve common refractors,  $j_{\text{tot}}$  is the number of records with overlapping difference windows at  $k$ ,  $t_{j,k}$  is the traveltime from  $j$  to a receiver at  $k$  and  $\delta t_{j,k}$  is the time difference

between common receivers on shotpoints  $j$  and  $k$  (Figure 5.6). This expression is also equivalent to

$$t_d(k)_n = \sum_{m=1}^{n-1} \frac{z(k)_m \cos(i_{m,n})}{v_m}, \quad (5.2)$$

where  $z(k)_m$  is the thickness of layer  $m$  at shotpoint  $k$ ,  $v_m$  is the velocity of layer  $m$ , and  $i_{m,n}$  is the critical angle;  $i_{m,n} = \sin^{-1}(v_m/v_n)$  (Figure 5.6). Equation (5.2) can be rearranged to solve for the thickness,  $z_m$  for  $n-1$  layers of the depth model.

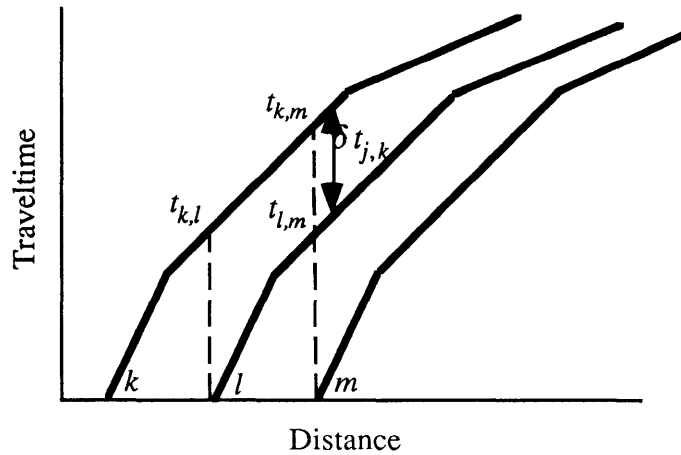


FIG. 5.6. Definition of traveltimes, time differences, and source-receiver offsets for the time difference method (Lawton, 1989).

The velocity of layer  $n$ , in which the wave is refracted (Figure 5.7), is given by Lawton (1989) as:

$$v_n = \frac{1}{j_{\text{tot}}} \sum_{j=1}^{j_{\text{tot}}} \frac{x_{j,k}}{t_{j,k} - t_d(j)_n - t_d(k)_n}, \quad (5.3)$$

where  $x_{j,k}$  is the offset between the shotpoints  $j$  and  $k$ . Since there is not always a shot at each receiver location, the delay time  $t_d$  for a receiver at a location  $r$  is determined as

$$t_d(r)_n = \frac{1}{j_{\text{tot}}} \sum_{j=1}^{j_{\text{tot}}} \frac{t_{j,r} - t_d(j)_n - x_{j,r}}{v_n}. \quad (5.4)$$

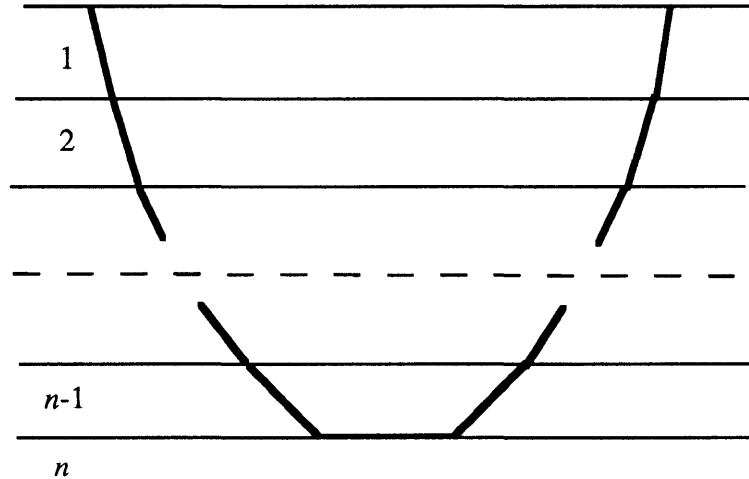


FIG. 5.7. Geometry of the raypath for the  $n$ -layer model, showing a wave refracted at the  $n$ th layer.

### 5.3.2 EGRM Gauss-Seidel Refraction Static correction

This method is a combination of the EGRM (Palmer, 1980) and Gauss-Seidel iterative decomposition method (Farrell and Euwema, 1984) of refraction static correction analysis (Diggins et al., 1988). The 'Extended Generalized Reciprocal Method', or EGRM, algorithm is based on the 'Generalized Reciprocal Method', the GRM, of refraction interpretation introduced by Palmer (1980). The EGRM adds and subtracts combinations of travelpaths to estimate velocities and intercept times. Velocities are derived from a plot of time differences between shots ahead of and behind the receiver versus the differences in offset. The velocity of the refractor is obtained from half of the presumed linear least-squares slope. Time depths to each receiver are then calculated using the formula

$$t_d(k)_n = \frac{t_{j,k} + t_{l,k} - t_{j,l}}{2} = \sum_{m=1}^{n-1} \frac{z(k)_m \cos(i_{m,n})}{v_m}, \quad (5.5)$$

where  $t_{j,k}$ ,  $t_{l,k}$ , and  $t_{j,l}$  are the traveltimes along paths  $jk$ ,  $lk$ , and  $jl$ , respectively (Figure 5.8).

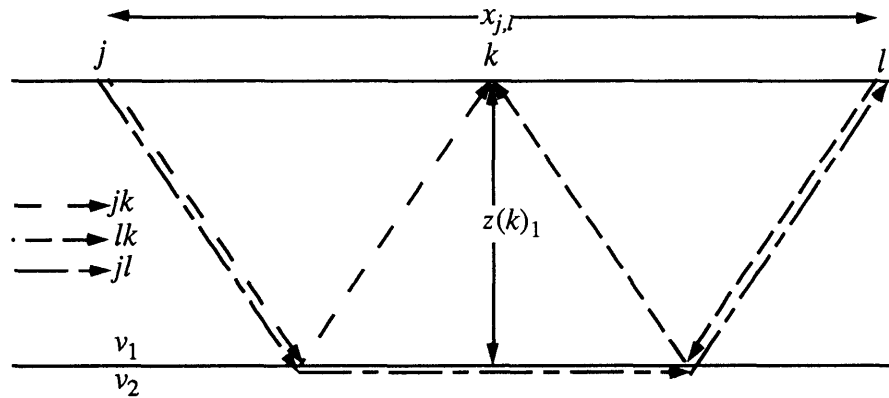


FIG. 5.8. Definition of thickness at the receiver, offset between receivers; and forward, reverse, and total travelpaths for a two-layer model ( $n=2$ ).

This is essentially twice the definition of the intercept time used in the intercept method (Barry, 1967). These time depths are then used by the Gauss-Seidel iterative decomposition method (Farrell and Euwema, 1984) to calculate the refractor thicknesses and velocities. The Gauss-Seidel method is based upon the assumption that the travelttime from receiver  $j$  to receiver  $l$  is given by the sum of the delay times at  $j$  and  $l$ , plus an offset-dependent term (Diggins et al., 1988):

$$t_{j,l} = t_d(j) + t_d(l) + \frac{x_{j,l}}{v_{n-1}}. \quad (5.6)$$

Rearranging this equation allows for a solution for  $v_{n-1}$ , using the delay times obtained from the EGRM analysis:

$$v_{n-1} = x_{j,l} (t_{j,l} - t_d(j) - t_d(l)). \quad (5.7)$$

The program then calculates the delay time at receiver  $j$  keeping the delay time at receiver  $l$  constant, and using the new velocities,  $v_{n-1}$ . At the ends of the line, or whenever the Gauss-Seidel algorithm fails to find a velocity, the velocity derived from EGRM is used.

The program iteratively calculates the delay times to achieve a final solution for the delay time at each shot and receiver. The thicknesses can then be calculated using

$$z(k)_n = \frac{v_n}{\cos(\phi)} \left( t_d(k) - \sum_{m=1}^{m_{tot}} \frac{z(k)_m \cos(i_{m,n})}{v_m} \right), \quad (5.8)$$

where

$$\phi = \sin^{-1} \left( \frac{v_1}{v_2} \right). \quad (5.9)$$

## 5.4 CRP stack-power optimization

The CRP stack-power static correction method was devised by Cary and Eaton (1993). The underlying assumption of this method is that the static solution on the P-SV CRP-stacked section can be approximated by the receiver static solution only. Similar to other optimization methods (Ronen and Claerbout, 1985), the method obtains the optimal static picks for all the events within a chosen trace window of the CRP-stacked section by optimizing an objective function. As a starting point, consider the objective function for the total power of the laterally averaged CRP-stacked section,

$$E(g,n) = \sum_j \sum_t \left( \sum_{k=j-n+1}^j G_k(t + g_k) \right)^2, \quad (5.10)$$

where  $G_k$  denotes the  $k$ th CRP-stacked trace and  $g_j$  is the  $j$ th receiver static. Based on the cross-correlation approach of Ronen and Claerbout (1985), a pilot trace,  $P_j$  is defined as

$$P_j = \sum_{k=j-n+1}^j G_k(t + g_k). \quad (5.11)$$

Equation (5.10) then becomes (Cary and Eaton, 1993):

$$E(g,n) = \sum_j \sum_t \left( P_j^2 + G_j^2 + 2P_j G_j \right), \quad (5.12)$$

which is maximized by choosing the receiver static  $g_j$  according to the maximum of the cross-correlation of  $P$  and  $G$ .

The method can be summarized as follows (Cary and Eaton, 1993):

$$\left\{ \begin{array}{l} \text{for } j = 1, J, \\ \text{pilot}(t) = G_{j-n+1}(t + g_{j-n+1}) + G_{j-n}(t + g_{j-n}) + \dots + G_{j-1}(t + g_{j-1}), \\ g_j = \max[\text{pilot}(t) \otimes G_j(t)] \end{array} \right\}, \quad (5.13)$$

where  $\otimes$  denotes the cross-correlation operation.

## 5.5 Comparison of static-correction methods

The resulting near-surface Earth models for the two refraction methods, namely the time-difference method and the EGRM Gauss-Seidel method, are shown as Figures 5.9 and 5.10, respectively. Refraction analysis uses these near-surface Earth models to obtain the expected static shifts required to simulate replacing the calculated Earth layers with a single flat layer of uniform velocity. These static shifts are for the two-way traveltimes of an S wave, and therefore must be halved to obtain the required one-way S-wave traveltimes for P-SV surveys. The S-wave static is then combined with the P-wave static to form the P-SV static solution. The results of applying these solutions to the CRP-stacked sections are shown as Figure 5.11 for the time-difference method and Figure 5.12 for the EGRM method. To obtain the CRP stack-power optimization results shown in Figure 5.14, a 5-trace model with a correlation window from 700 to 1700 ms and a maximum lag of  $\pm 140$  ms was used. The static solution derived from the hand-picking method is also shown as Figure 5.13.

From the vertical-component final stacked sections, shown in Chapter 4, there is apparently no structural relief in the area spanned by this survey. The goal of static correction analysis is to remove all of the static shifts and hence to be left with the most

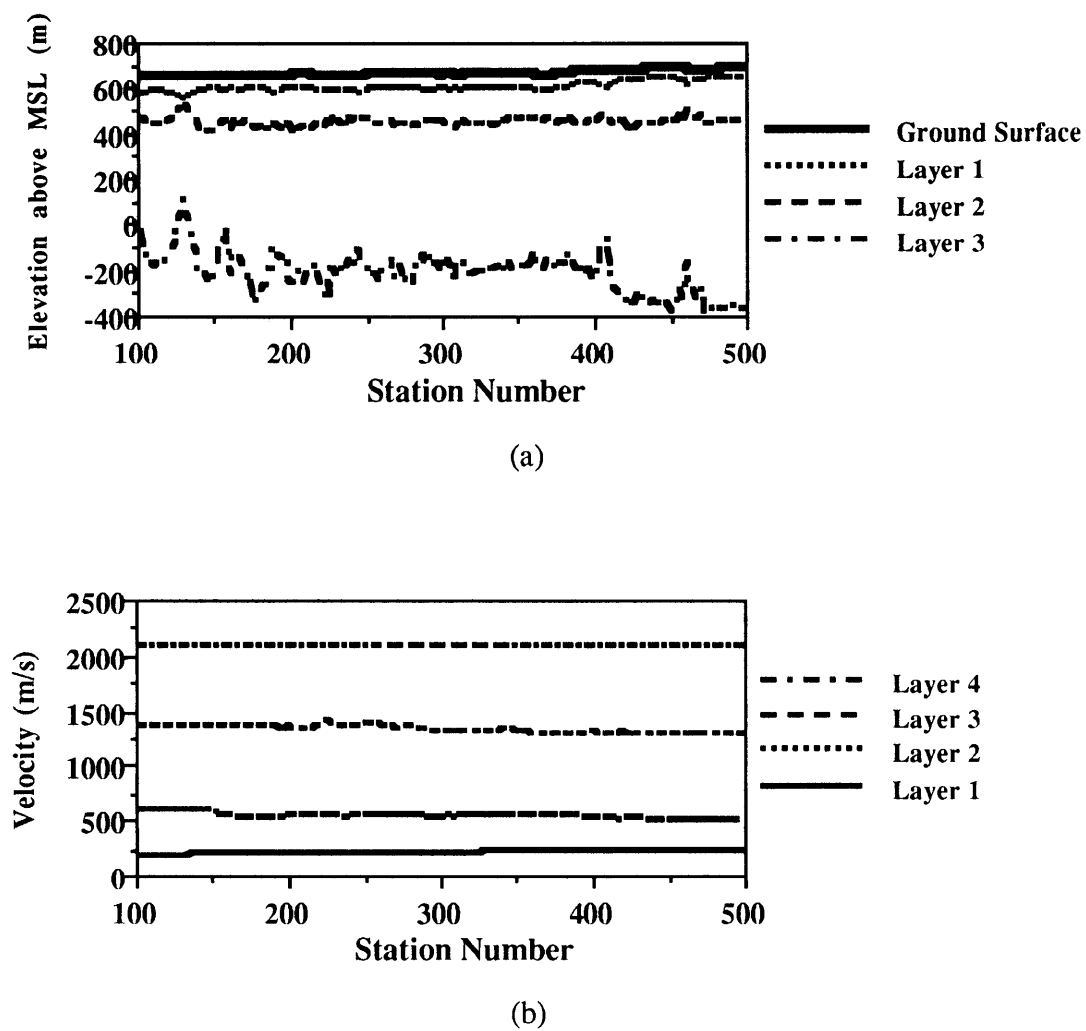


FIG. 5.9. Time-difference S-wave Earth models: (a) thicknesses; (b) velocities.

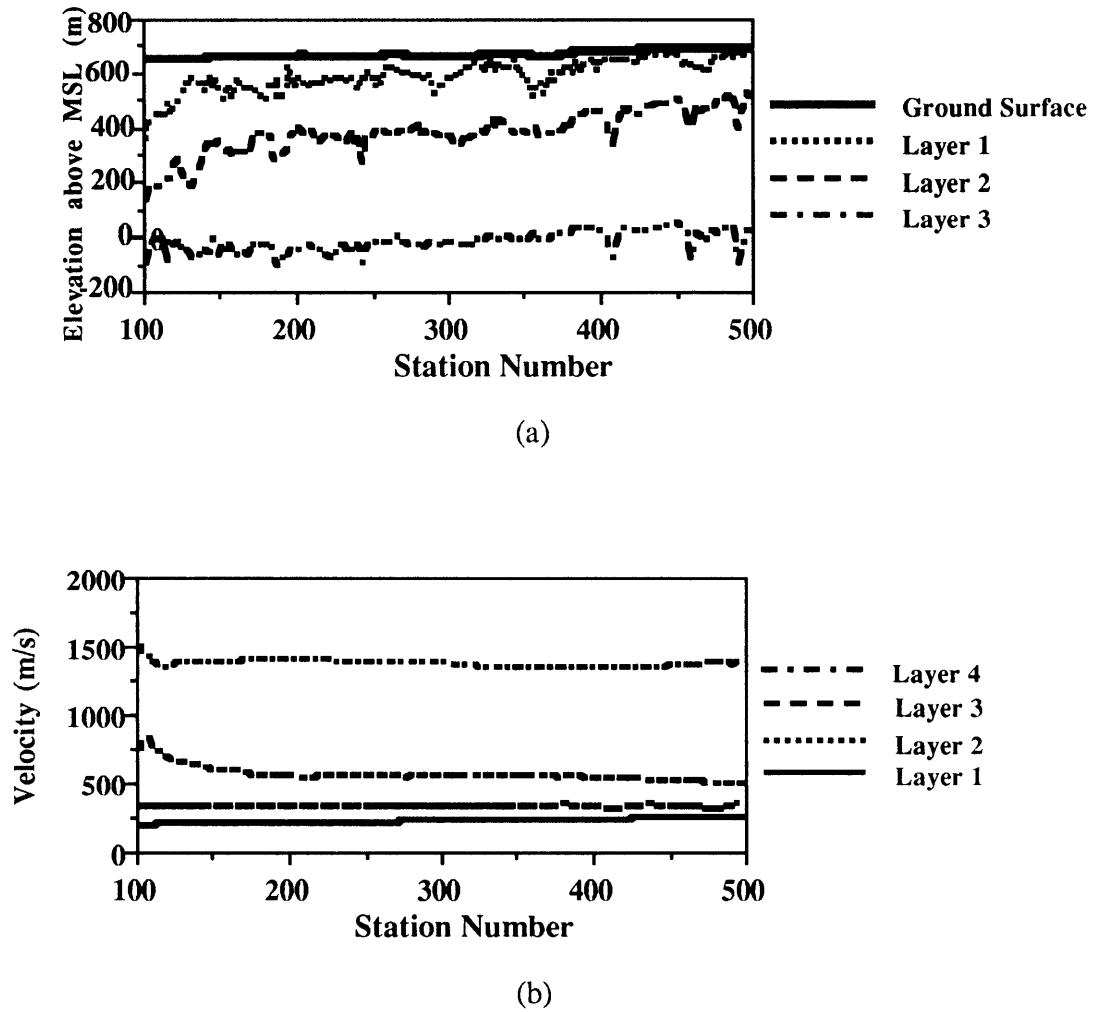


FIG. 5.10. EGRM Gauss-Seidel S-wave Earth models: (a) thicknesses; (b) velocities.

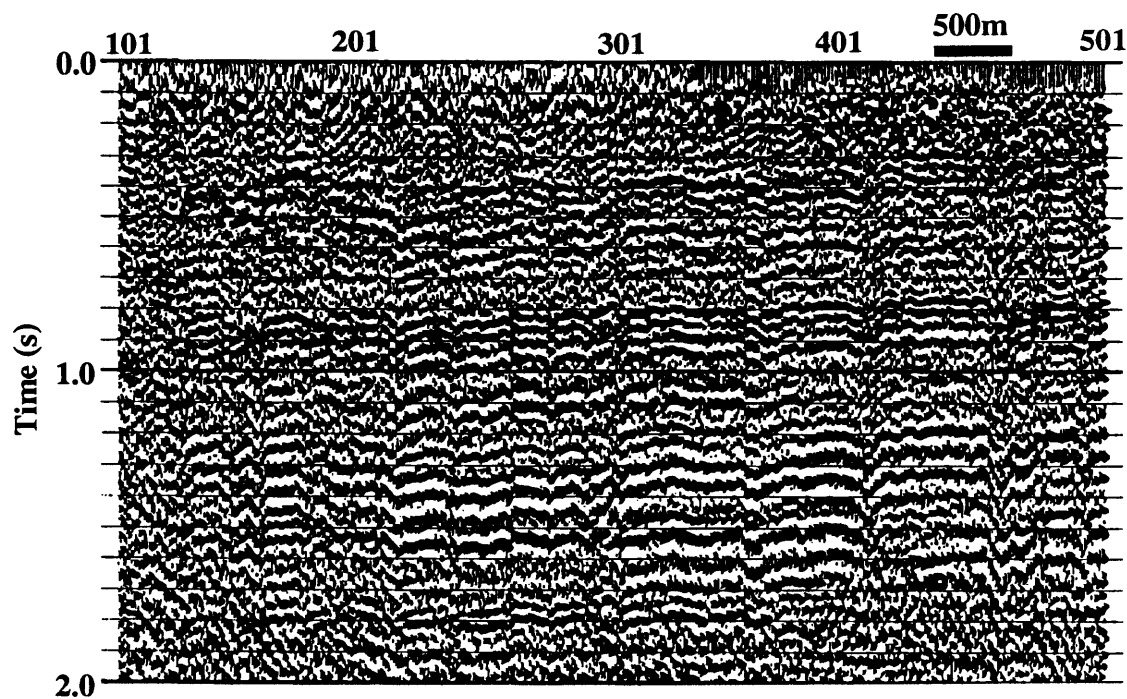


FIG. 5.11. CRP-stacked section with time-difference refraction static solution applied.

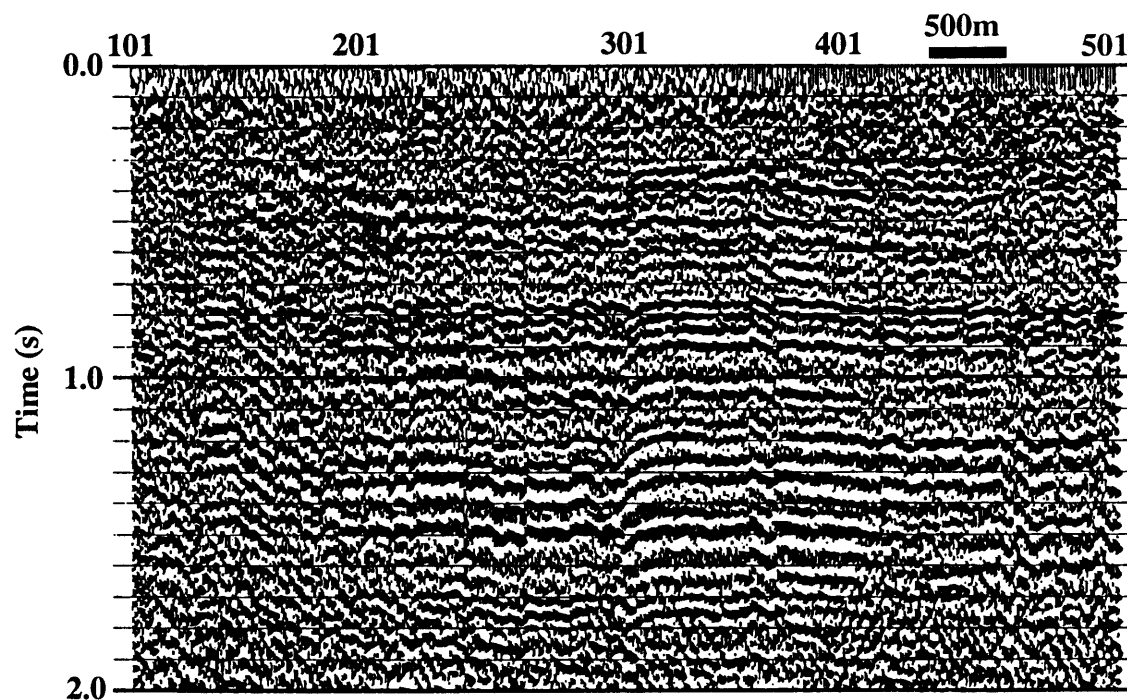


FIG. 5.12. CRP-stacked section with EGRM Gauss-Seidel refraction static solution applied.

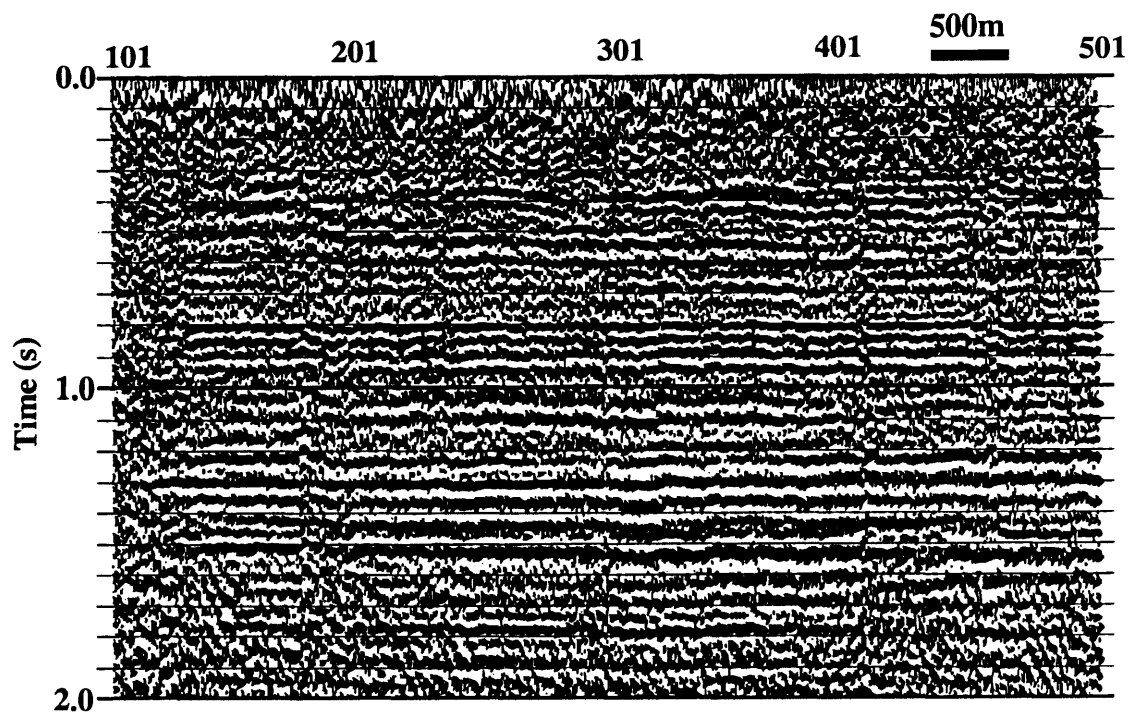


FIG. 5.13. CRP-stacked section with hand-picked and some residual static solution applied.

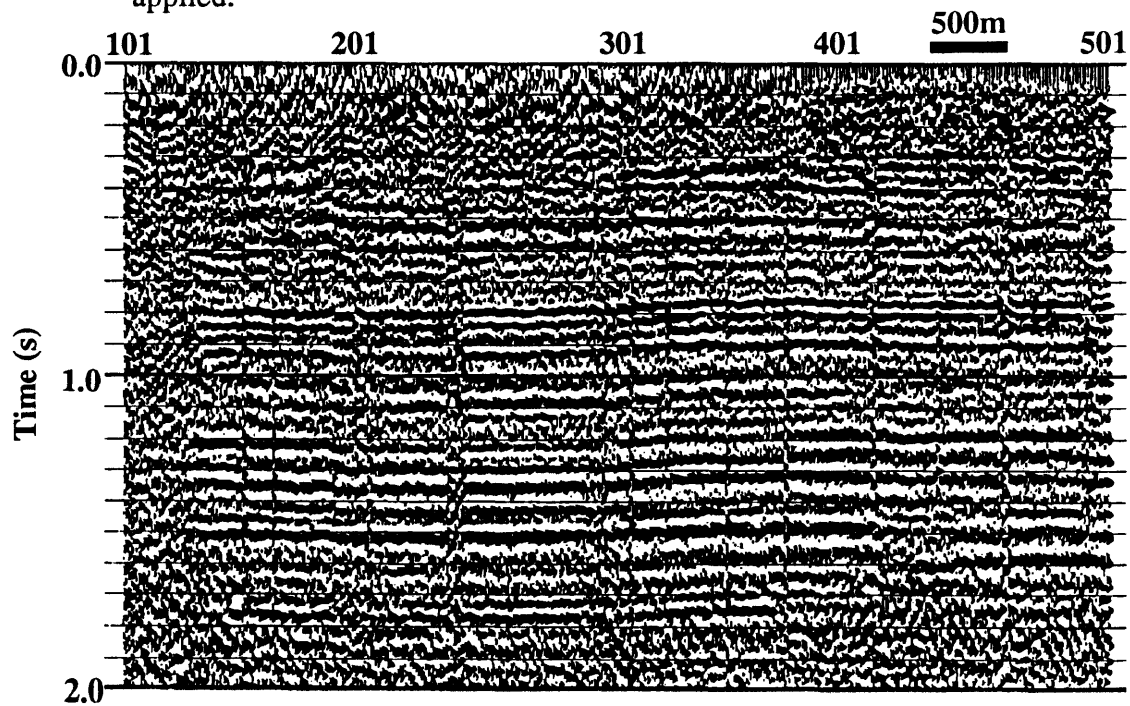


FIG. 5.14. CRP-stacked section with CRP stack-power optimization static solution applied.

coherent and continuous final stacked section possible. For the P-SV case the source static solution is already known from the vertical component, and all that is left is to solve for the receiver static solution. Thus, the ability of a particular static correction method to solve for the receiver statics on the radial-component data is a good indication of the effectiveness of that method. Using this criterion, the hand-picked static correction method gives the best result, with the stack-power optimization static correction method giving a very similar result. The refraction static correction methods do not work as well; however, they both give considerable improvement over the original CRP-stacked section without any static corrections applied (Figure 5.4b). A further way to compare these methods is to examine a plot of the receiver static solutions (Figure 5.15). On this graph, the large static correction problems are easily seen as sudden negative spikes. Comparing the other methods to the best final static solution, using both of the hand-picking and residual static correction methods, the minor deficiencies of the refraction methods and the good result obtained by the stack-power optimization methods are evident.

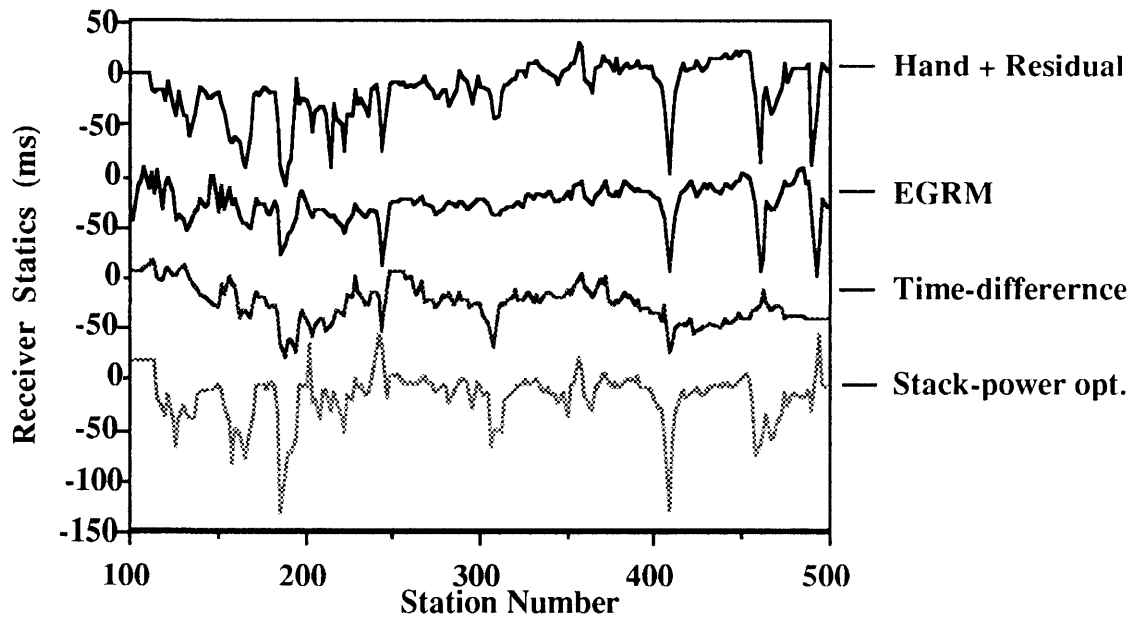


FIG. 5.15. Comparison of the receiver static solutions.

## 5.6 Discussion

Hand-picking of the receiver static corrections gives a good result, but it is very tedious and time-consuming. Each of the three iterations of the hand-picking method required the previous static corrections to be applied to the CCP data and the data to be sorted into the common receiver domain. The CRP-stacked section is then plotted and a static value for each of four hundred traces is picked. These four hundred values are then entered into a static corrections file and applied to the data to start another pass. In total, hand-picking of this data set takes almost eight hours. Another problem with this method is the lack of a proper long-wavelength solution, which the refraction static correction methods offer.

While the refraction methods do give a reasonable result and provide a physically valid, long-wavelength result, they are difficult to implement and time-consuming due to the need to pick the S refraction. A further problem with these methods is that shear refractions are not present in many 3-component P-wave source data sets (Harrison, 1992). Various source-receiver configurations may serve to suppress the shear refractions and thereby eliminate the possibility of using this method. The design of the Slave Lake survey was favourable to the generation of S refractions, as this survey was shot using a shot array with the long dimension of the rectangle parallel to the profile direction. In the future, surveys are likely to be designed to suppress S refractions, since they are usually considered as noise and obstruct the P-SV reflections. Even if they are present, they are difficult to pick. While P refractions are the first breaks for the vertical-component record, S refractions are embedded in the shot record along with the reflections. A further drawback of this method is the amount of time required to pick the shear refractions on a workstation. Automatic picking could save much time, but it is hampered by noise masking the shear refraction and is unable to override this noise using logical reasoning as the human mind can. One possible solution to the noise problem is to apply

polarization filtering to remove everything except the shear refraction, since a shear refraction should have a characteristic direction of particle motion at the surface. Another possibility might be a time-variant velocity filter to selectively enhance the shear refraction relative to the background. However, a velocity filter is a multichannel filter which is likely to smear the sharp variations (statics). Finally, instantaneous amplitudes or frequencies could also be used to assist the time-variant velocity filter to selectively enhance the shear refraction.

CRP stack-power optimization appears to be a reasonable solution to many of the problems that hinder the other methods. It gives a very good result, with a minimum of effort. CRP stack-power optimization is similar to the other residual static correction methods in that it is entirely automatic. However, the solution obtained by CRP stack-power optimization is better than the other methods. While other methods are likely to get stuck in a local maximum of the energy function, this method rapidly converges to find the global maximum. The possibility of cycle-skipping is still present, and a visual inspection of the CRP-stacked section is necessary to safe-guard against cycle-skipping. CRP stack-power optimization can readily compute the one-dimensional cross-correlation functions that it optimizes, but simultaneously optimizing a multidimensional, multimodal objective function with respect to all the parameters is not easy, and sometimes not possible at all (Rothman, 1985).

Theoretically, the Monte Carlo simulated-annealing method (Vasudevan et al., 1992) should be able to find the global maximum of the energy function as this method is a combination of a totally random, Monte Carlo search technique and a controlled gradient-descent method (Cary and Eaton, 1993). The advantage of combining these two methods is that the combination would allow the algorithm to ascend into a local maximum in an iterative manner, yet retaining the option of jumping into another local maximum, which is perhaps an even better maximum. The critical, or annealing,

temperature controls the random-search versus the gradient-descent aspects of this method. It is estimated that convergence to a solution that is the global maximum could take up to 20 000 iterations (Vasudevan et al., 1992).

While the CRP stack-power optimization method works well, it does have a major drawback: it is quite similar to hand-picking in that it does smooth the data over a specified range. A solution that results in a smooth receiver stack may be esthetically pleasing, but it is only physically correct outside of the range of the smoothing operator. This is where combining the refraction static solution with a pass of CRP stack-power optimization as a residual static solution would be beneficial. The refraction static solution would provide the physical validity and long-wavelength P-SV static solution, while residual static corrections would remove the high-frequency remnants, just as is done for conventional (P-P) surveys.

## **Chapter 6 - TWO-COMPONENT SEISMIC DATA PROCESSING: CRYSTAL EAST, ALBERTA**

### **6.1 Introduction**

A two-component seismic survey was conducted in the Crystal East area of central Alberta in 1985 by Compagnie Générale de Géophysique (CGG) (Figure 6.1). The data have since been donated to The University of Calgary by Alberta Energy Company Ltd. The targets in this area are Viking sandstone channels, and the problem is to differentiate the clean sandstones from the background of shale and/or shaly sandstones. This chapter discusses the processing of the two components of the three lines, showing examples from line 6223. Details of the interpretation of this survey are given in the next chapter, Chapter 7.

### **6.2 Data acquisition**

This survey consists of three lines, each of which was recorded in two components, the vertical component and the radial component (Figure 6.2). The field acquisition parameters are summarized in Table 6.1. The survey was recorded using 1 kg dynamite charges as sources and a 120-trace DFS-V recording system. The radial component was recorded separately from the vertical component, using different geophones and geophone arrays. The vertical component was recorded using geophones with a central frequency of 14 Hz, arranged in an array of nine geophones covering 25 m, while the radial component employed 8.5 Hz geophones in an array of nine geophones over 75 m. Further, the near offset for the radial component was 62.5 m, while the vertical component used a near offset of only 37.5 m. Both components recorded 120

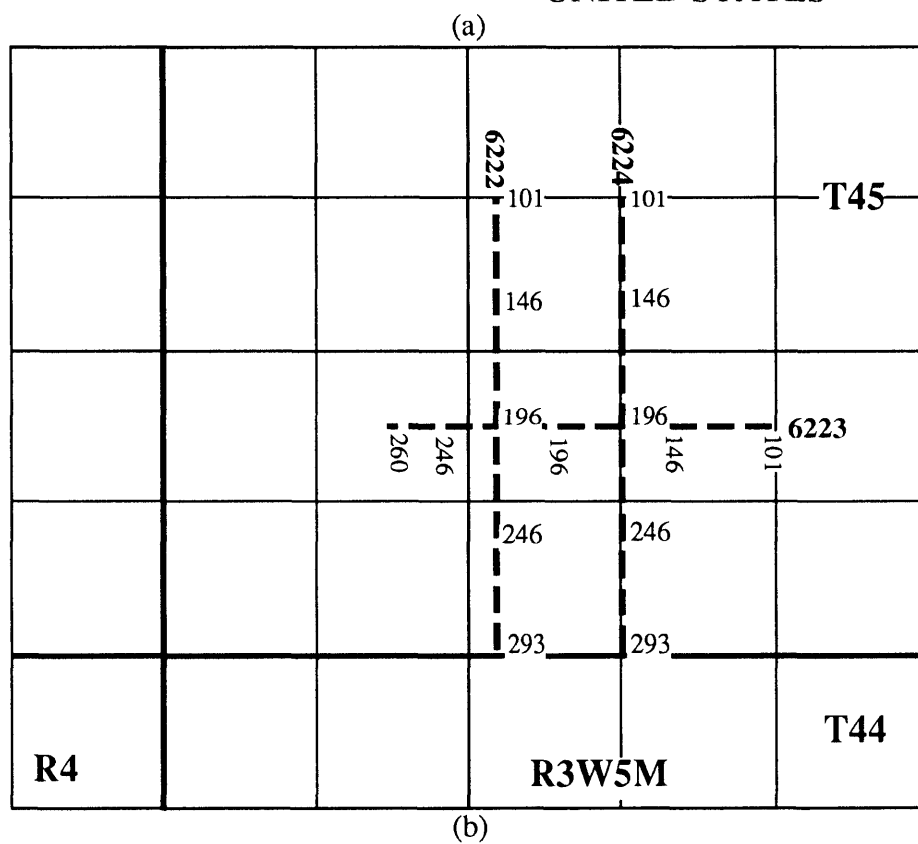
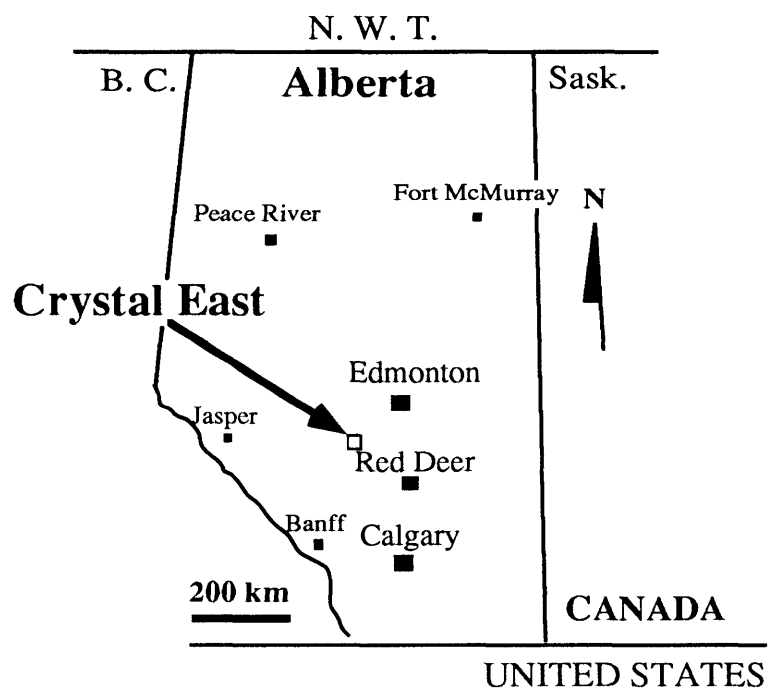


FIG. 6.1. Location map of the Crystal East survey: (a) inside Alberta; (b) close-up of lines 6222, 6223, and 6224.

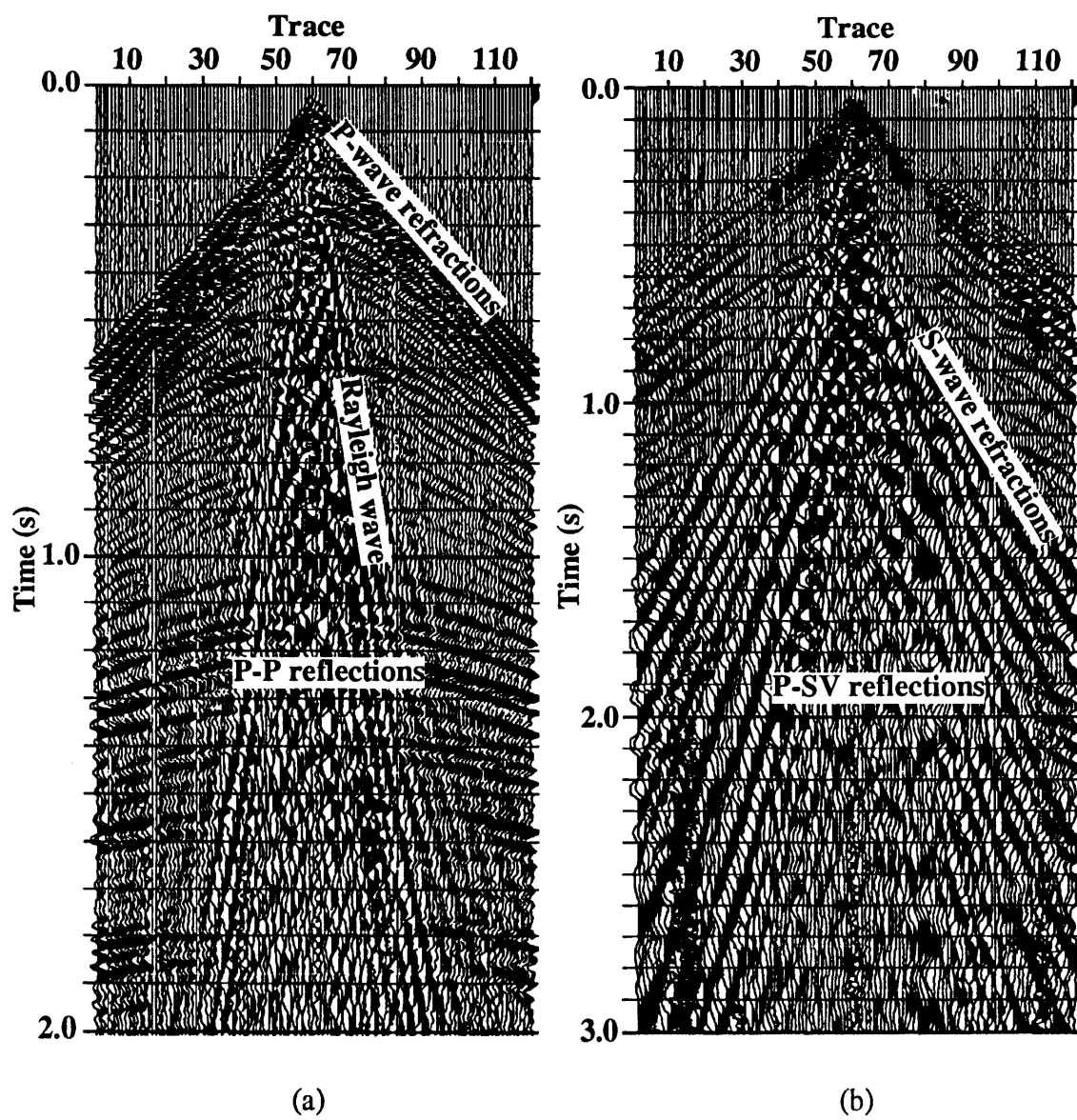


FIG. 6.2. Shot record at station 146 from line 6223: (a) P-P; (b) P-SV.

groups with a group interval of 25 m, and a normal source interval of 50 m, resulting in a nominal fold of 30.

Table 6.1. Field acquisition and recording parameters for the Crystal East survey.

Energy source	Dynamite
Charge size	1 kg
Hole Depth	18 m
Geophone array	Radial: 9 over 75 m Vertical: 9 over 25 m
Geophone type	Radial: LRS 280, 8.5 Hz Vertical: LRS 280, 14 Hz
Groups recorded	120
Group interval	25 m
Normal source interval	50 m
Near offset	Radial: 62.5 m Vertical: 37.5 m
Recorder type	DFS-V
Number of channels	120
Sample rate	2 ms
Low-cut filter	Out
Antialias filter	120 Hz
60-Hz notch filter	In
Fixed gain	36 dB

Shot records at station 146 are shown in Figure 6.2 for the two directions of recorded motion, the vertical component and the radial component. Individual trace balancing as well as a time-variant gain function were applied to the field records in order to correct for geometrical spreading and field gain.

### 6.3 Data Processing

Similar to the Slave Lake three-component seismic data set, processing of the Crystal East two-component seismic data set began with the processing of the vertical channel. The processing of the vertical channel followed a standard P-wave processing flow (Table 6.2). Then, following the general processing flow outlined in Chapter 2, the radial component was processed (Table 6.3).

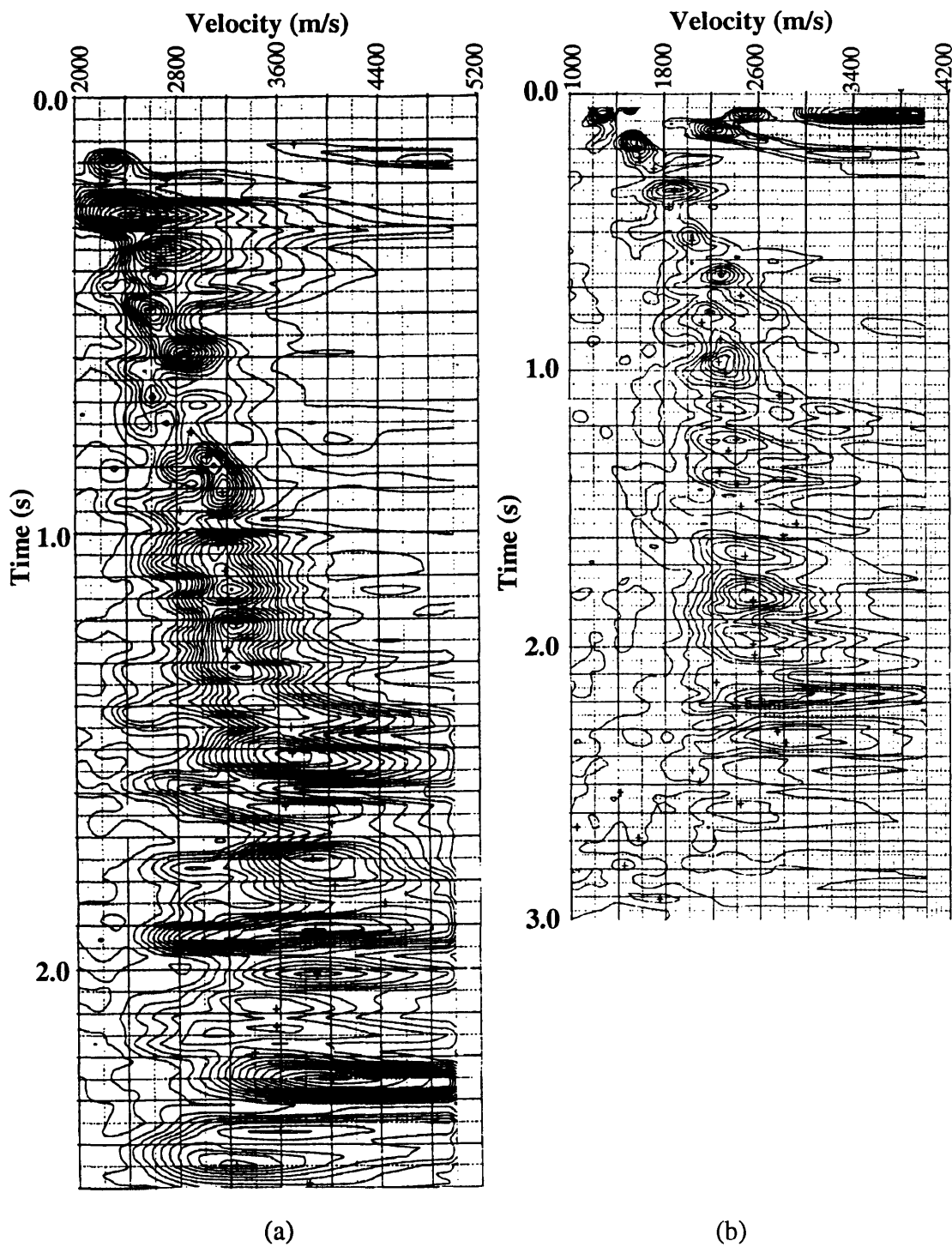


FIG. 6.3. Sample velocity-analysis semblance plots for line 6223: (a) vertical-component (P-P) data and (b) radial-component (P-SV) data.

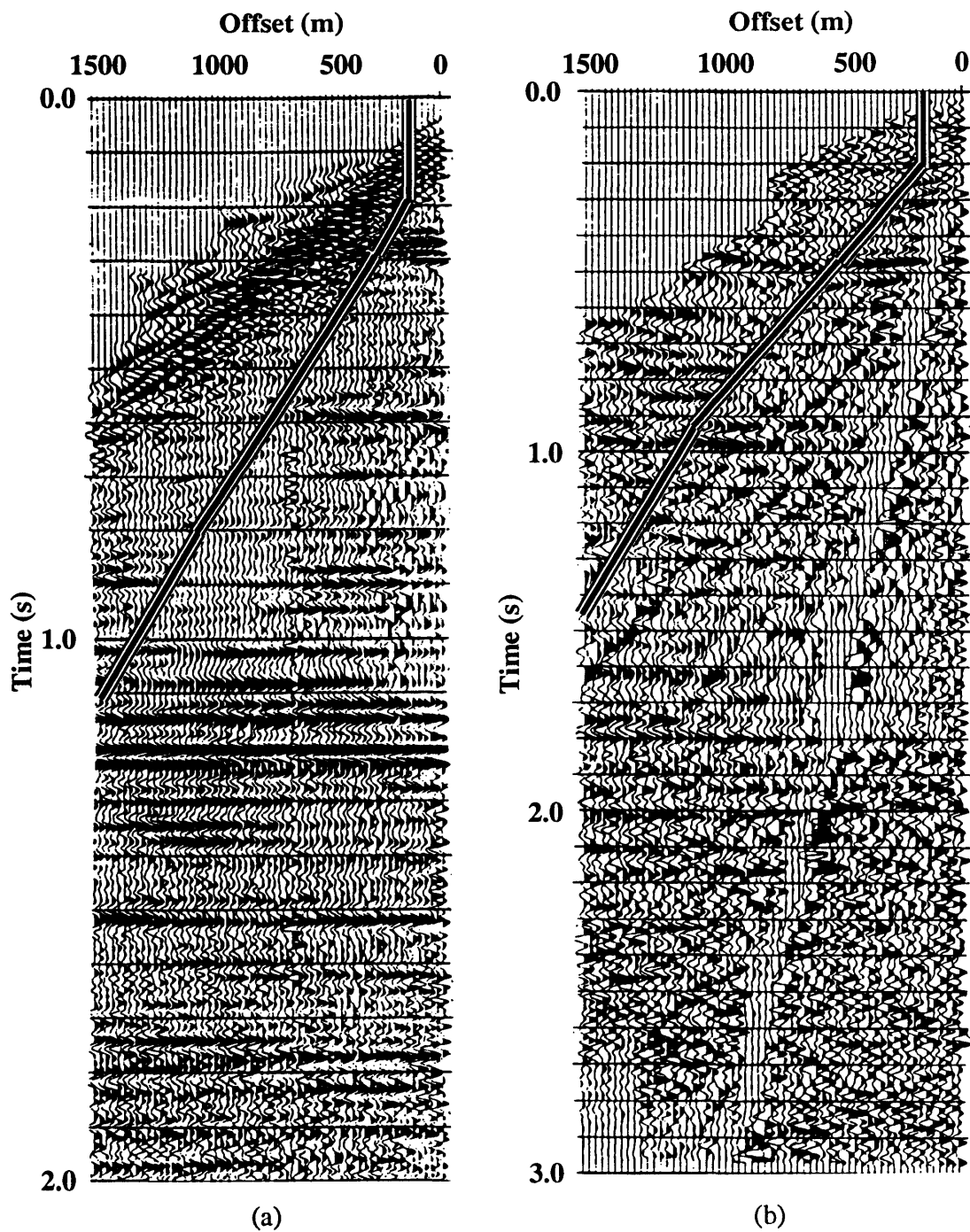


FIG. 6.4. Sample NMO-corrected common offset stacked records: (a) P-P; (b) P-SV. The applied mute function for station 146 is shown on both records.

Table 6.2. Processing sequence and parameters for the vertical-component (P-P) data.

DEMULTIPLEX  
 GEOMETRIC SPREADING COMPENSATION  
 SPIKING DECONVOLUTION  
     100-ms operator, 0.1% prewhitening  
 CMP SORT  
 ELEVATION & REFRACTION STATIC CORRECTION  
 INITIAL VELOCITY ANALYSIS  
 AUTOMATIC SURFACE-CONSISTENT STATIC CORRECTION  
     Correlation window of 800 to 1900 ms  
     Maximum shift of  $\pm 24$  ms  
 VELOCITY ANALYSIS  
 NORMAL MOVEOUT CORRECTION  
 MUTE  
 CMP TRIM STATIC CORRECTION  
     Correlation window from 400 to 1900 ms  
     Maximum shift of  $\pm 12$  ms  
 STACK  
 BANDPASS FILTER  
     Zero-phase, 12-65 Hz  
 RMS GAIN  
     First window of 200 ms, second of 400 ms,  
     subsequent windows of 400 ms.  
 F-K FILTER  
     Pass-band of  $\pm 2$  ms/trace  
     6 dB maximum reject.

Sample velocity analysis plots for the vertical and radial channels show the stacking velocities used for the final stacked section (Figure 6.3). Velocity analysis for the P-SV data was done using the conventional, hyperbolic-NMO curve-fitting technique that is used for the P-P data. There does not appear to be any sign of P-SV events on the P-P analysis and there is only a slight indication of P-P events on the P-SV analysis. Common-offset stack records were used to pick the mute functions, and an example from station 146 is included as Figure 6.4.

Table 6.3. Processing sequence and parameters for the radial-component (P-SV) data.

DEMULTIPLEX  
 GEOMETRIC SPREADING COMPENSATION  
 SPIKING DECONVOLUTION  
     120 ms operator, 0.1% prewhitening  
 REVERSE THE POLARITY OF TRAILING SPREAD  
 APPLY FINAL P-WAVE STATIC CORRECTION  
 INITIAL VELOCITY ANALYSIS  
 APPLY HAND STATIC CORRECTION FROM SURFACE STACKS  
 AUTOMATIC SURFACE-CONSISTENT STATIC CORRECTION  
     Correlation window from 400 to 2200 ms  
     Maximum shift of + or -24 ms  
 CMP STACK  
 CCP REBINNING  
     Vp/Vs of 1.96 used  
 VELOCITY ANALYSIS  
 NORMAL MOVEOUT APPLICATION  
 MUTE  
 STACK  
 BANDPASS FILTER  
     Zero-phase, 8-35 Hz  
 RMS GAIN  
     First window of 200 ms, second of 400 ms,  
     subsequent windows of 400 ms length  
 F-K FILTER  
     Pass-band from -3 to +3 ms/trace  
     6 dB maximum reject.

Unfortunately, data quality is not sufficient in this case to allow for statements concerning amplitude changes with offset for either component. In order to determine the frequency bandwidth of the data, an averaged time-variant cross-power spectrum was generated (Figure 6.5). The cross-power spectra were calculated by computing the average cross-correlations of 20 adjacent stacked traces and computing the spectra at 100 ms increments using a 400 ms correlation window. The usable frequency bandwidth for the vertical component is observed to be from about 10 to 60 Hz, while the bandwidth for the radial component is from 8 to 35 Hz. The source-point static solution from the vertical component was successfully applied to the radial component, but the receiver static solution from the radial component was not adequate for the vertical component. The large high-frequency static shifts on the CRP-stacked section for the radial

component were first picked by hand and then an automatic static correction program was used to generate the final static solution. The final static solutions applied to the vertical- and radial-component data are shown as Figure 6.6.

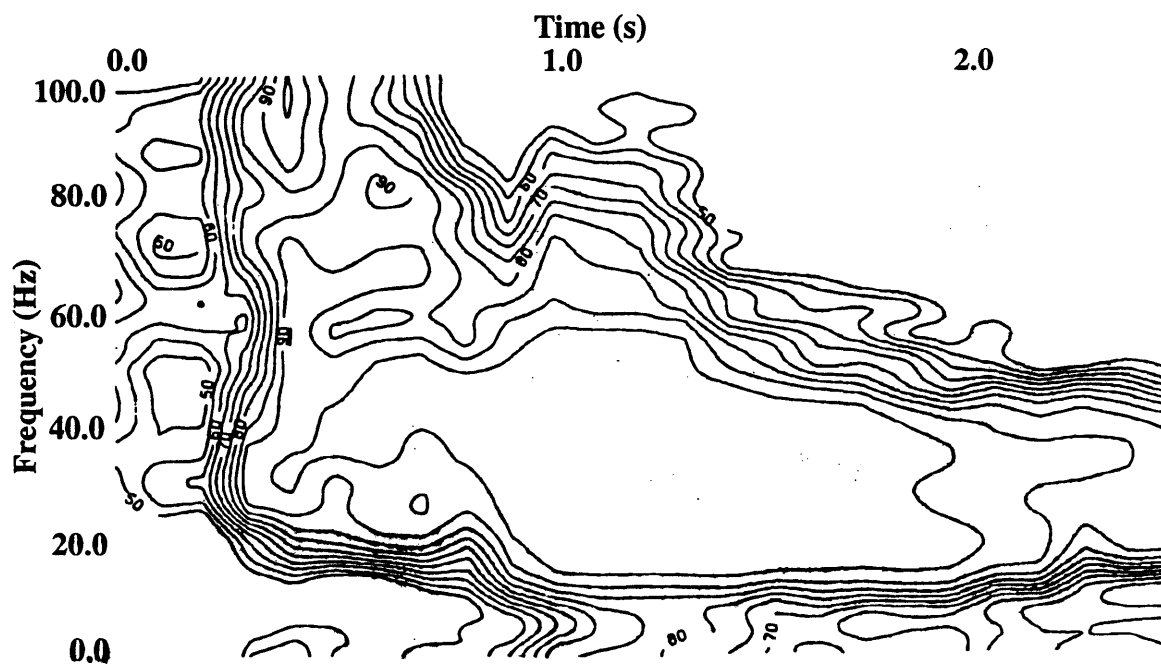
The final stacked section for the three lines in the Crystal East survey are shown as Figures 6.7, 6.8 and 6.9. These sections have the final static solutions applied, as well as a mild  $f-k$  filter with a pass-band of  $\pm 2$  ms/trace for the vertical-component and  $\pm 3$  ms/trace for the radial-component data sets, with a 6-dB maximum reject. The radial components can be used to predict the presence of anisotropy in the area. If there was large anisotropy in the area, then events on the N-S lines, lines 6222 and 6224, should not correlate with events on the E-W line 6224 as shear-wave splitting would result in a fast and a slow shear-wave direction. Correlation of the radial components of the Crystal East survey failed to indicate any variation of the shear-wave velocity with direction, thereby indicating that there is no anisotropy (Figure 6.10).

The correlation between the P-wave section and the converted-wave section can readily be made by examination of the character of a part of the P-wave section and its continuation as a converted-wave section (Figure 6.11). Using the correlated event times, time intervals are calculated for the P-P and the P-SV cases to give a ratio of P-wave velocity to S-wave velocity,  $V_P/V_S$ , using equation (6.1).

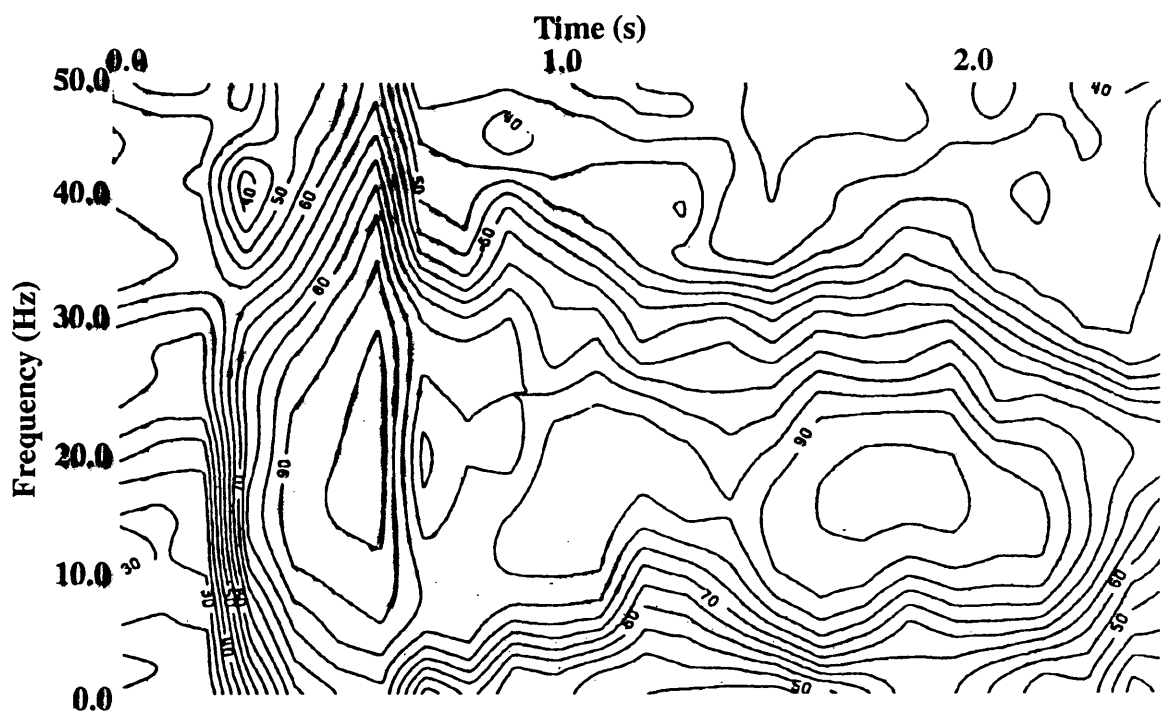
$$V_P/V_S = \frac{2I_S}{I_P} - 1, \quad (6.1)$$

where  $I_P$  is the P-P time interval, and  $I_S$  is the P-SV time interval. The results are given in Table 6.4. The errors associated with the  $V_P/V_S$  analysis are calculated using the standard-error or probable-error analysis method.

A time-weighted average over the whole section is then used to rebin the converted-wave data using the asymptotic approximation for converted-wave binning (Chapter 3).



(a)



(b)

FIG. 6.5. Averaged time-variant cross-power spectra between adjacent stacked traces from line 6223: (a) P-P; (b) P-SV. Contours are in percentage of maximum.

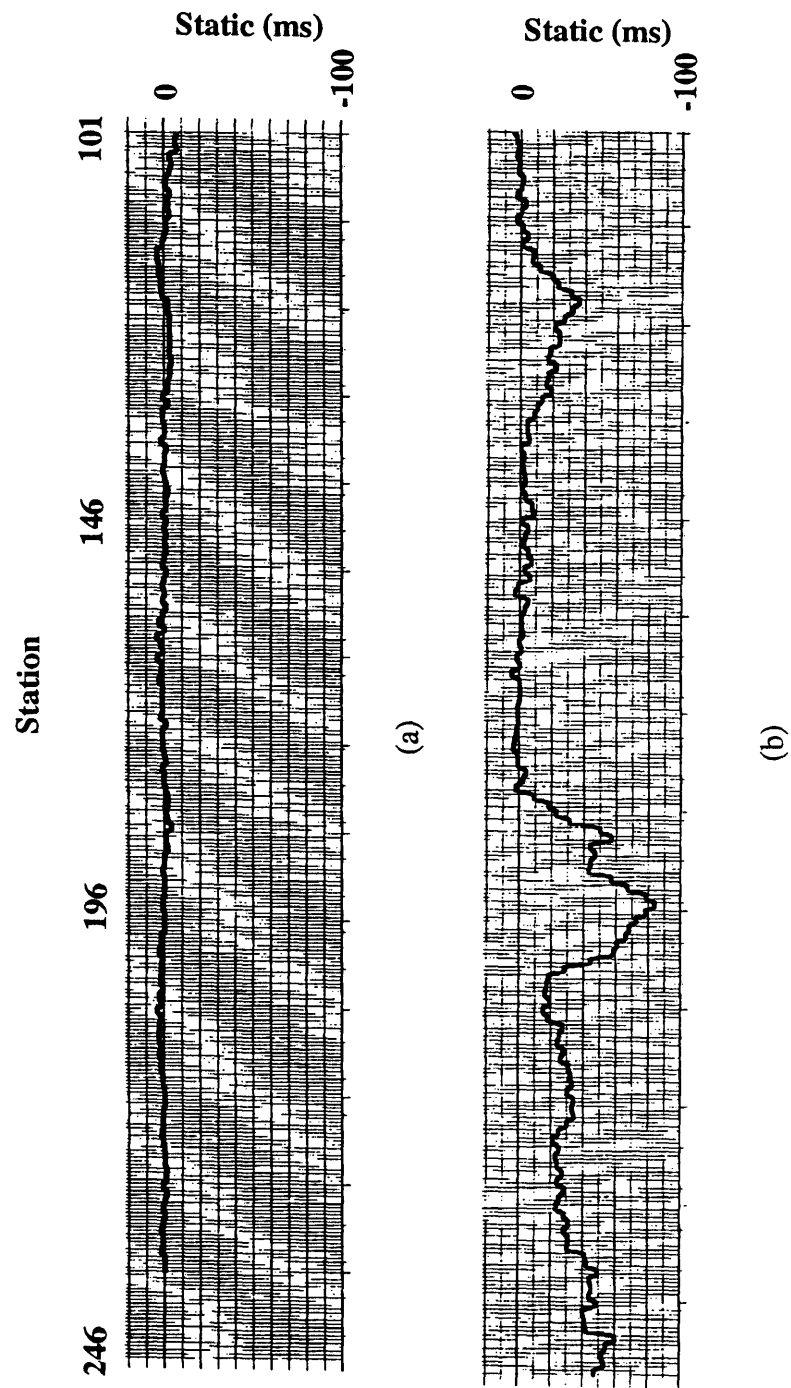
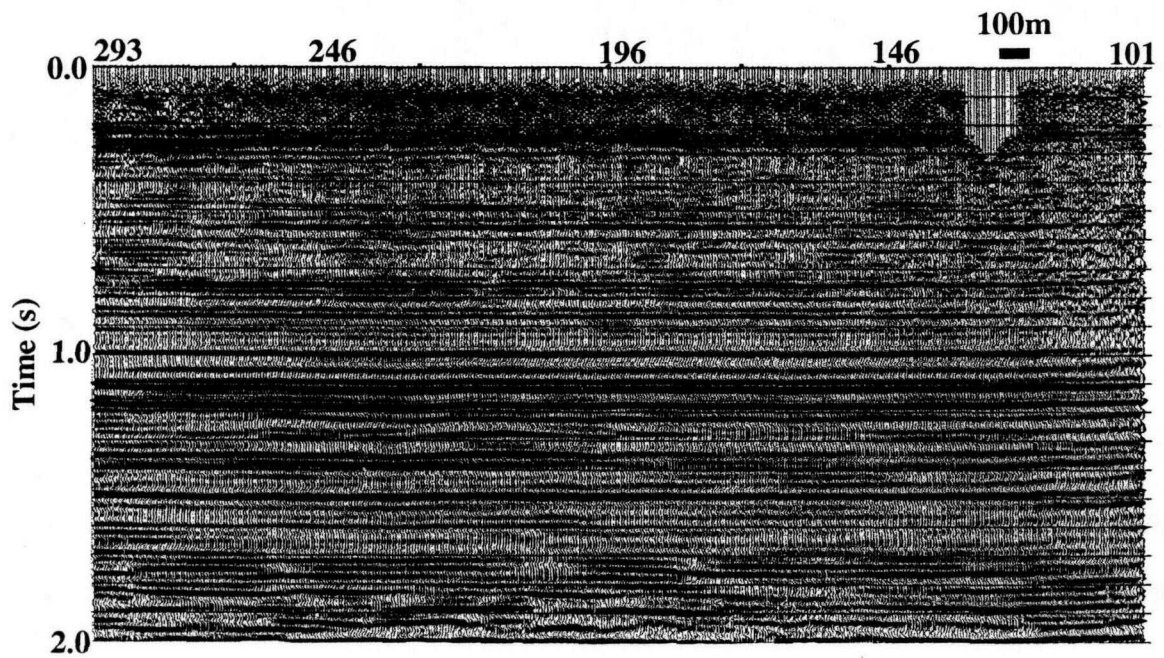
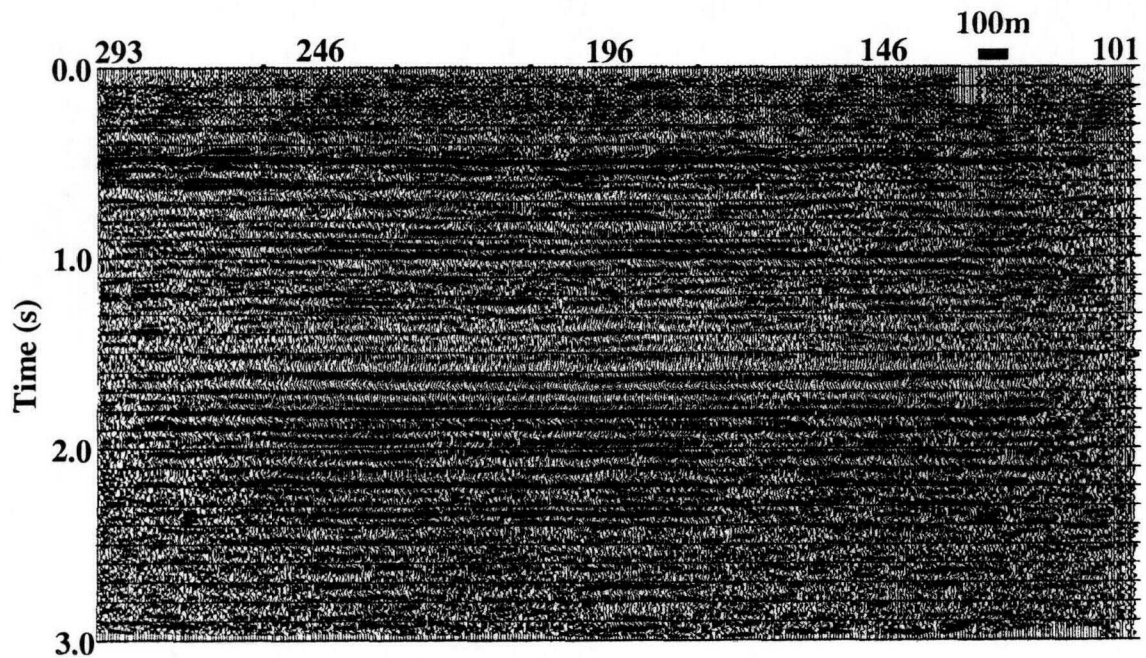


FIG. 6.6. Final receiver static solutions for line 6223: (a) P-P; (b) P-SV.

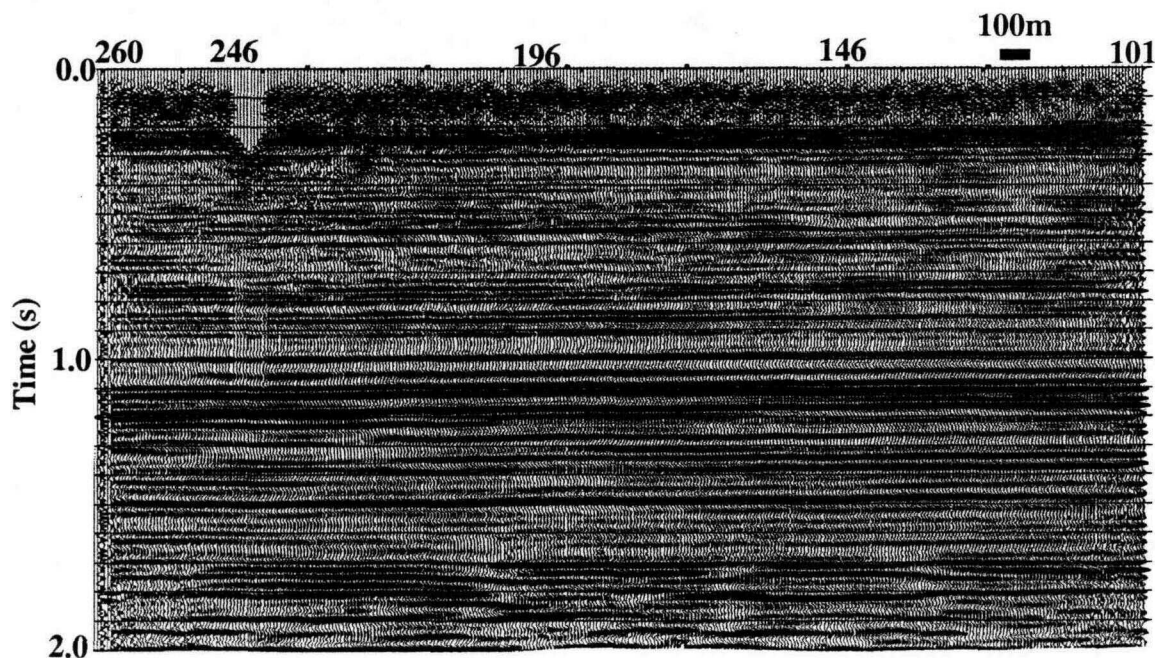


(a)

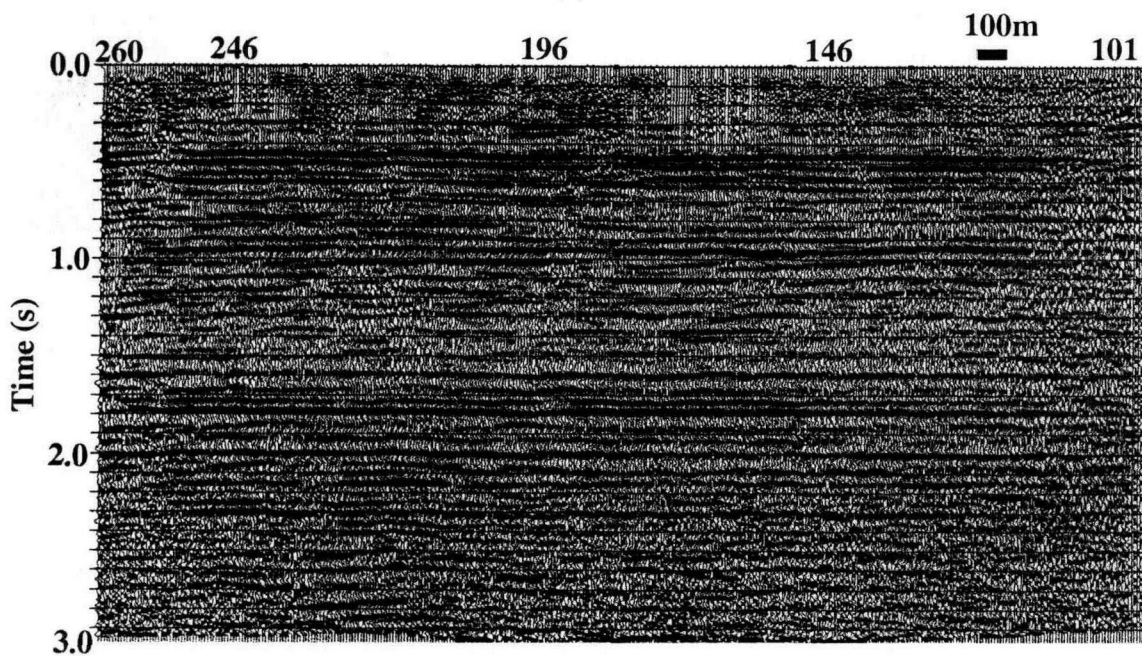


(b)

FIG. 6.7. Final stacked sections from line 6222 with poststack  $f$ - $k$  filter applied:  
 (a) P-P; (b) P-SV.

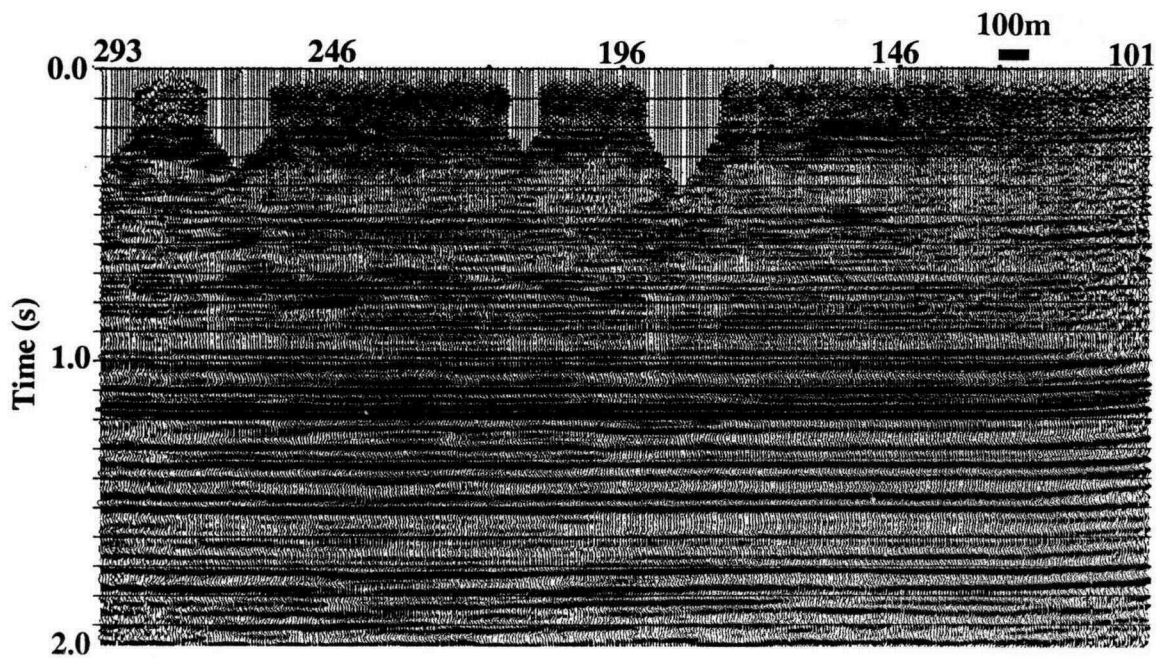


(a)

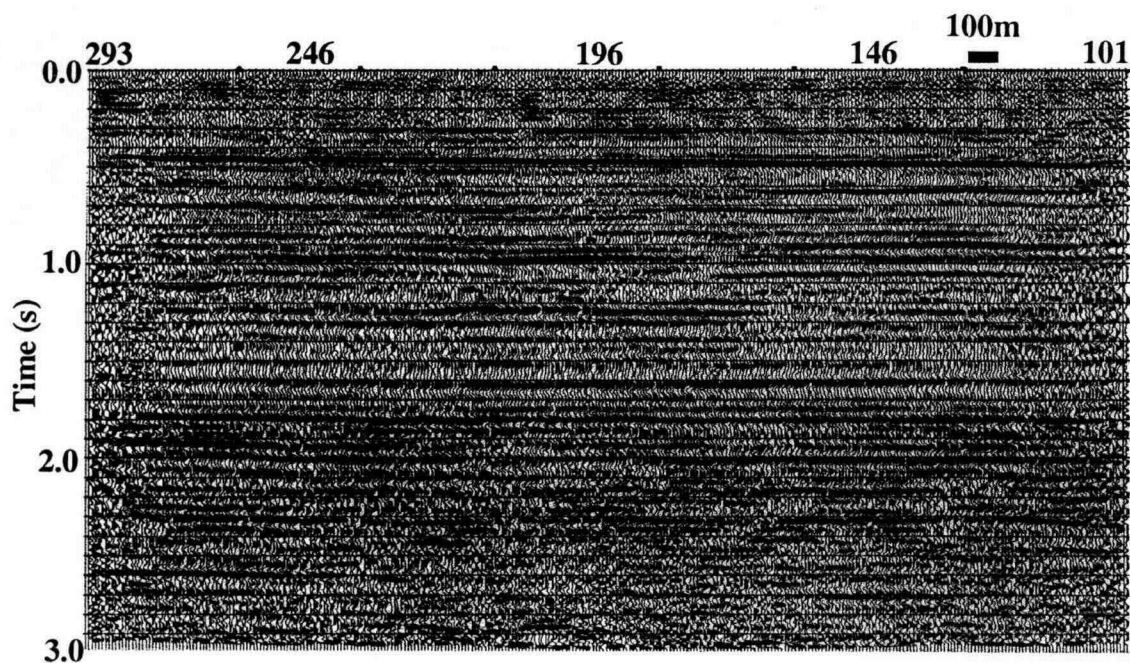


(b)

FIG. 6.8. Final stacked sections from line 6223 with poststack  $f$ - $k$  filter applied:  
(a) P-P; (b) P-SV.



(a)



(b)

FIG. 6.9. Final stacked sections from line 6224 with poststack  $f$ - $k$  filter applied: (a) P-P; (b) P-SV.

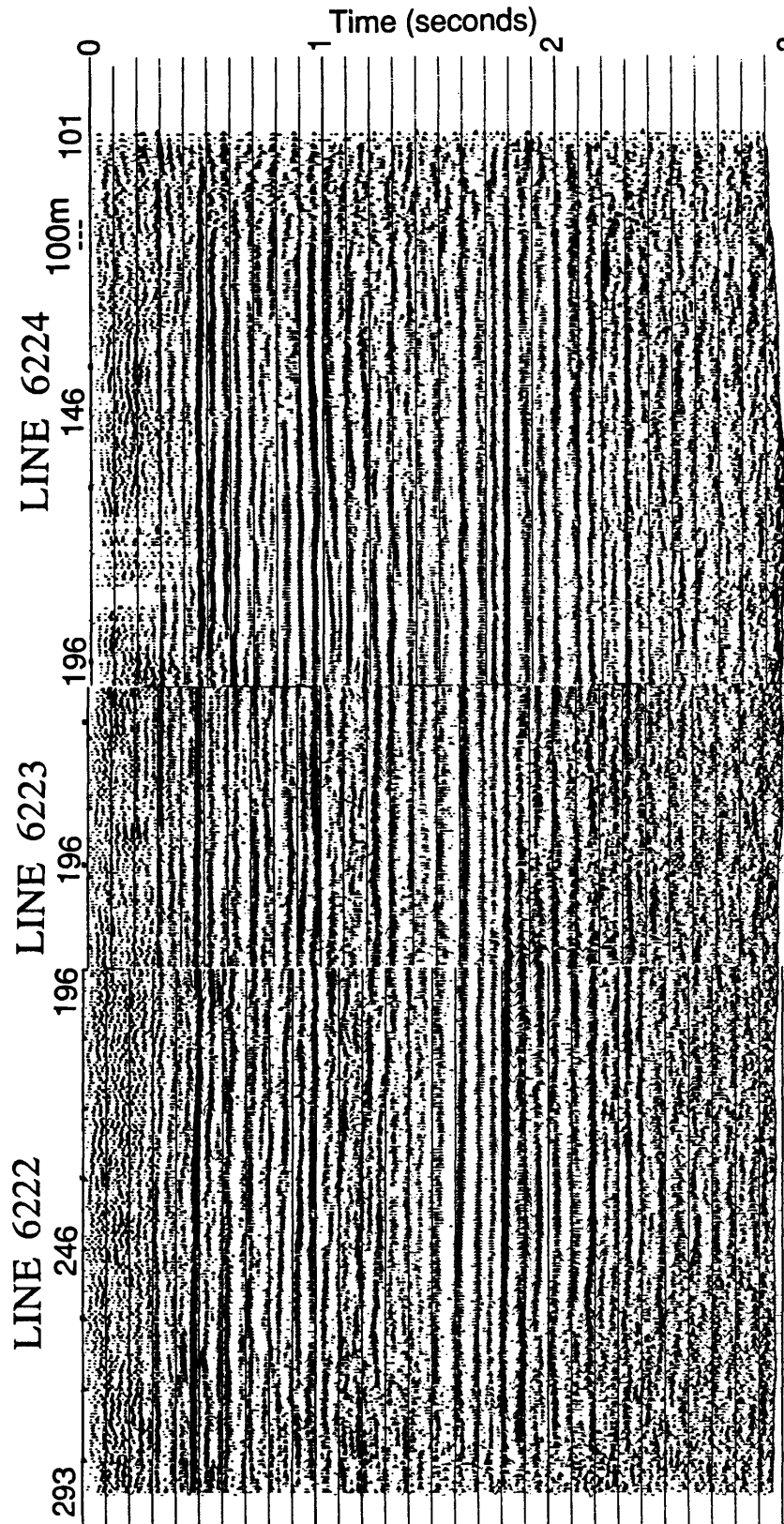


FIG. 6.10. Correlation of the radial components of the Crystal East survey.

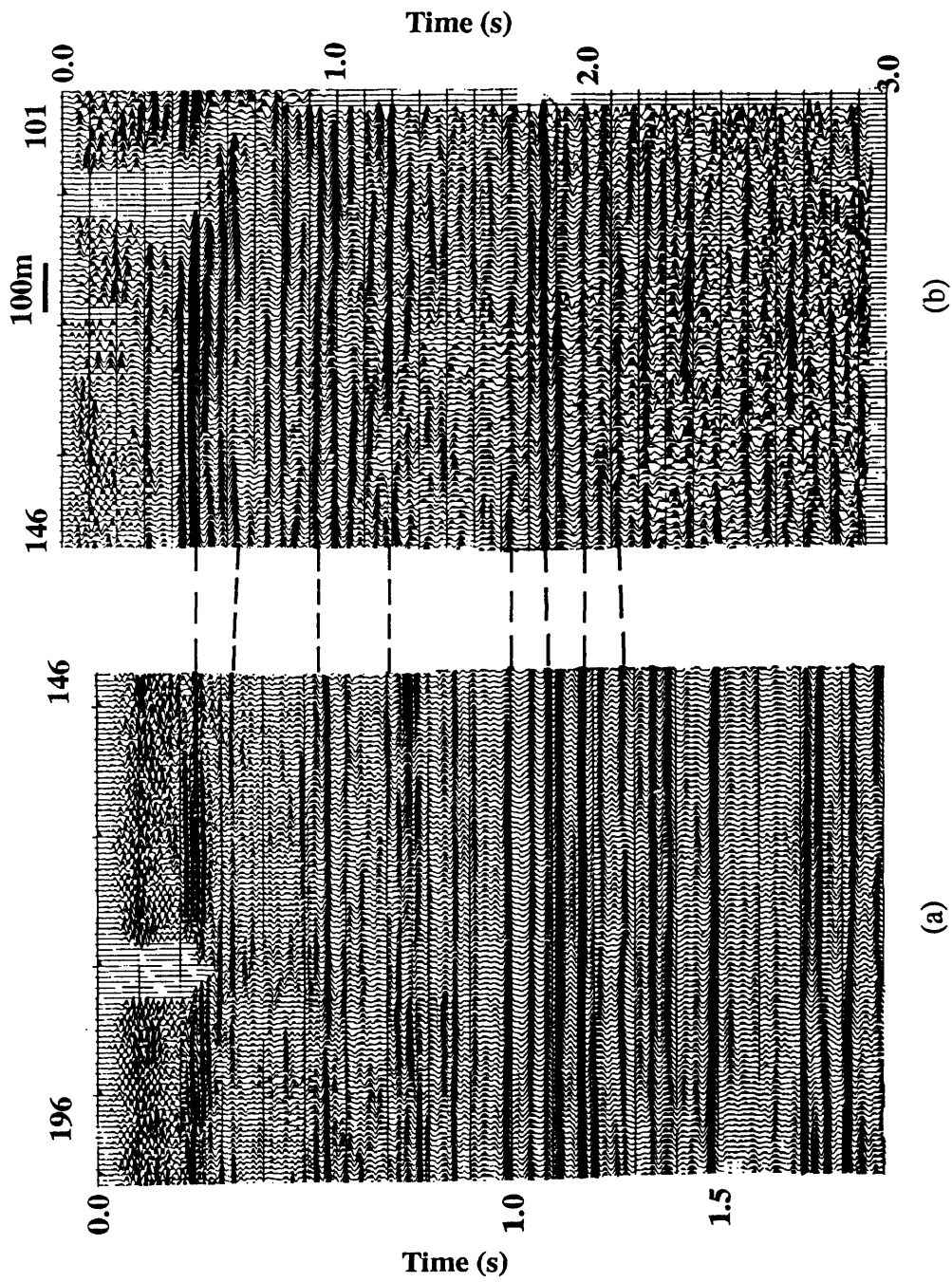


FIG. 6.11. Reflection correlation between (a) the vertical-component (P-P) section and (b) the radial-component (P-SV) section from line 6224.

Table 6.4.  $V_P/V_S$  ratios computed from event and interval times (in ms) for vertical (P-P) and radial (P-SV) component data.

P-P time $\pm 2$	P-P interval $\pm 2$	P-SV time $\pm 2$	P-SV interval $\pm 2$	$V_P/V_S$
130		310		
	105		170	$2.24 \pm 0.10$
235		498		
	322		498	$2.09 \pm 0.03$
557		978		
	298		462	$2.10 \pm 0.02$
855		1440		
	135		175	$1.59 \pm 0.07$
990		1615		
	60		85	$1.83 \pm 0.16$
1051		1700		
	37		50	$1.70 \pm 0.26$
1088		1750		
	32		50	$2.13 \pm 0.33$
1120		1800		
	150		210	$1.84 \pm 0.06$
1270		2010		
	220		310	$1.82 \pm 0.04$
1490		2320		

## 6.4 Discussion

The vertical-component data clearly show the presence of a signal-generated noise with a velocity of about 610 m/s (Figure 6.2a). This event is also present on the radial-component data, although it is largely obliterated by reverberations of the S-wave refractions. The low velocity of this event, its dispersive nature, and its presence on the radial component records are evidence that this event is a Rayleigh wave, otherwise known as ground roll.

The radial-component data also contain another event, with a velocity of about 1160 m/s (Figure 6.2b). From its low velocity and its similarity to the P-wave refraction, as well as the lack of its presence on the vertical component, this is assumed to be a source-generated, shear refraction (Schafer, 1991). Since the P-wave refractions have a velocity of about 3030 m/s, the  $V_P/V_S$  ratio of the near surface would be 2.61 using the

shear refractions, which is reasonable for the unconsolidated sediments of the near surface (Garotta, 1985).

In general, the radial-component record contains a fair signal strength, although much of the signal is covered by the Rayleigh wave and S refractions. An indication of P-SV reflections correlating with the P-P reflections on the vertical component is apparent on the right-hand side of the radial-component record at about 2.0 s two-way traveltime, as well as in the shallow record, above 1.4 s (Figure 6.2b).

## Chapter 7 - CONVERTED-WAVE INTERPRETATION

### 7.1 Introduction

Distinguishing shales and sandstones that have similar P-wave velocities and densities is usually very difficult and may not even be possible using conventional P-wave recording. However, if one also recorded S-wave information, then parameters that depend on the P-wave and S-wave velocities, such as the ratio  $V_p/V_s$  and Poisson's ratio could potentially be useful in distinguishing between lithologies (Pickett, 1963; Tatham and Stoffa, 1976; Tatham, 1982; Garotta et al., 1985). By recording the radial (P-SV) component of wave motion along with the vertical (P-P) component it is economically possible to determine Poisson's ratio by correlating reflectors on the final stacked sections of the two components. This method is used here on two-component data from the Crystal East field of central Alberta in an attempt to distinguish between productive Viking sandstone conglomerate channels and adjacent shales. Previous experience, as well as examination of sonic and density logs, has shown that the Viking channels do not yield any noticeable anomaly on conventional P-wave stacked sections. To test the applicability of combining P-wave and S-wave measurements to differentiate between lithology, a two-component survey was shot over a Viking channel. This chapter examines the interpretation of a two-component seismic survey recorded over a known Viking channel.

## 7.2 Event interpretation and correlation between P-P and P-SV seismic sections

Event interpretation for conventional (P-P) seismic data has long been achieved with zero-offset synthetic seismograms. Synthetic seismograms also allow the seismic events to be tied to depth and lithologic information from wells. For the P-SV case, this zero-offset synthetic seismogram has to be modified, since there is no mode conversion of the P wave to an S wave at normal incidence. Converted-wave (P-SV) surface-seismic data overcome this problem by summing across a range of offsets to simulate a conventional zero-offset stacked section. Similarly, P-SV synthetic seismograms are derived by stacking a range of NMO-corrected and muted offset traces, resulting in the P-SV synthetic stack (Lawton and Howell, 1992).

The method used by Lawton and Howell (1992) to generate the P-SV synthetic stack is based on the assumption of horizontal, homogeneous layers with constant time-interval thicknesses, no amplitude attenuation and no multiples. Following the construction of a layered model consisting of constant zero-offset traveltime thicknesses, each layer is raytraced using the bisection method to determine the traveltime and the angle of incidence for each ray. The exact amplitude and phase are calculated from the angle of incidence using the algorithm of Aki and Richards (1980).

The P-P synthetic gathers and the resulting P-P synthetic stacks are shown as Figure 7.1. To generate these synthetics, a group interval of 100 m and offsets from 0 m to 3000 m were used. A zero-offset Ricker wavelet with a centre frequency of 28 Hz was chosen to best match the surface-seismic data. The mute applied (Figure 7.1b) was the same as that used on the vertical-component surface-seismic data.

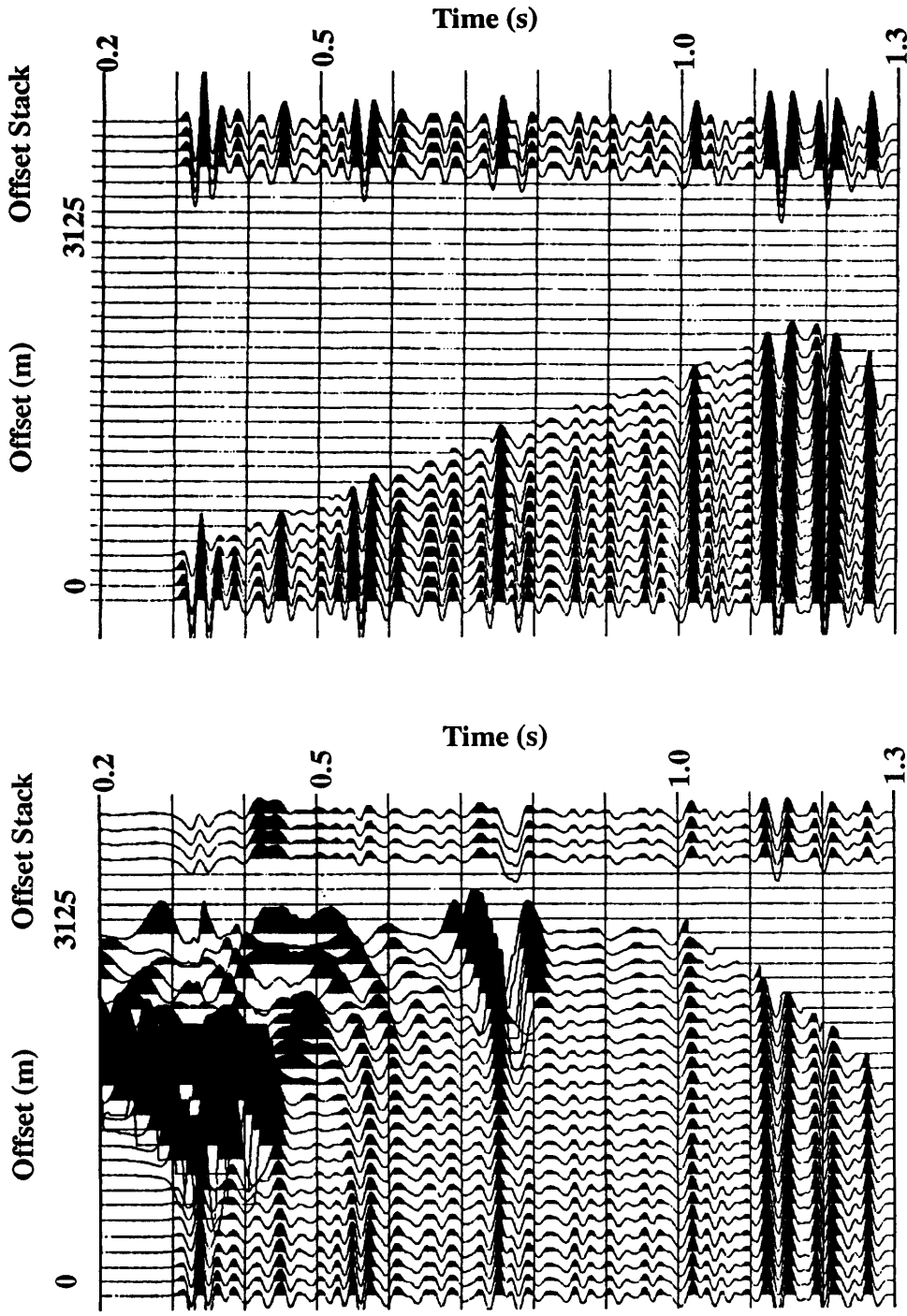
The P-SV synthetic gathers and the resulting P-SV synthetic stacks are shown as Figure 7.2. These synthetics used a group interval of 100 m and offsets from 0 m to 2500 m, with a 20-Hz, zero-phase Ricker wavelet. The lack of a full-waveform sonic log in the

area forced the use of a fixed  $V_P/V_S$  ratio to calculate the S-wave velocity from the P-wave sonic log. A  $V_P/V_S$  ratio of 2.0 was determined to provide the best fit to the data after experimenting with other  $V_P/V_S$  values. Using a combination of the P-P and P-SV synthetic seismograms to identify events on the P-P and P-SV surface-seismic data allows for correlation between the vertical and radial components (Figure 7.3).

### **7.3 Lithology estimation using lateral variations of $V_P/V_S$ ratios.**

The targets in the Crystal East field are Viking sand channels. The plays are stratigraphic, the sand channels interbedded in the surrounding shales. Deposition of these sands is most likely due to the high-energy environment of storm events (Beach, 1962; Koldijk, 1976). Since the sand channels have P-wave velocities similar to those of the surrounding shales, conventional zero-offset P-wave seismic sections will not show an amplitude anomaly over the channel. However, previous studies over similar channels have shown that using the ratio of P-wave traveltime to S-wave traveltime can be useful for discriminating sandstone from shale (Garotta, 1985). This is due to the change observed in the S-wave velocity, even when the P-wave velocities are similar for both lithologies. Plotting  $V_P/V_S$  versus  $V_P$  for clean sandstones and shales (Miller and Stewart, 1990) clearly demonstrates the differentiation between sandstone and shale (Figure 7.4).

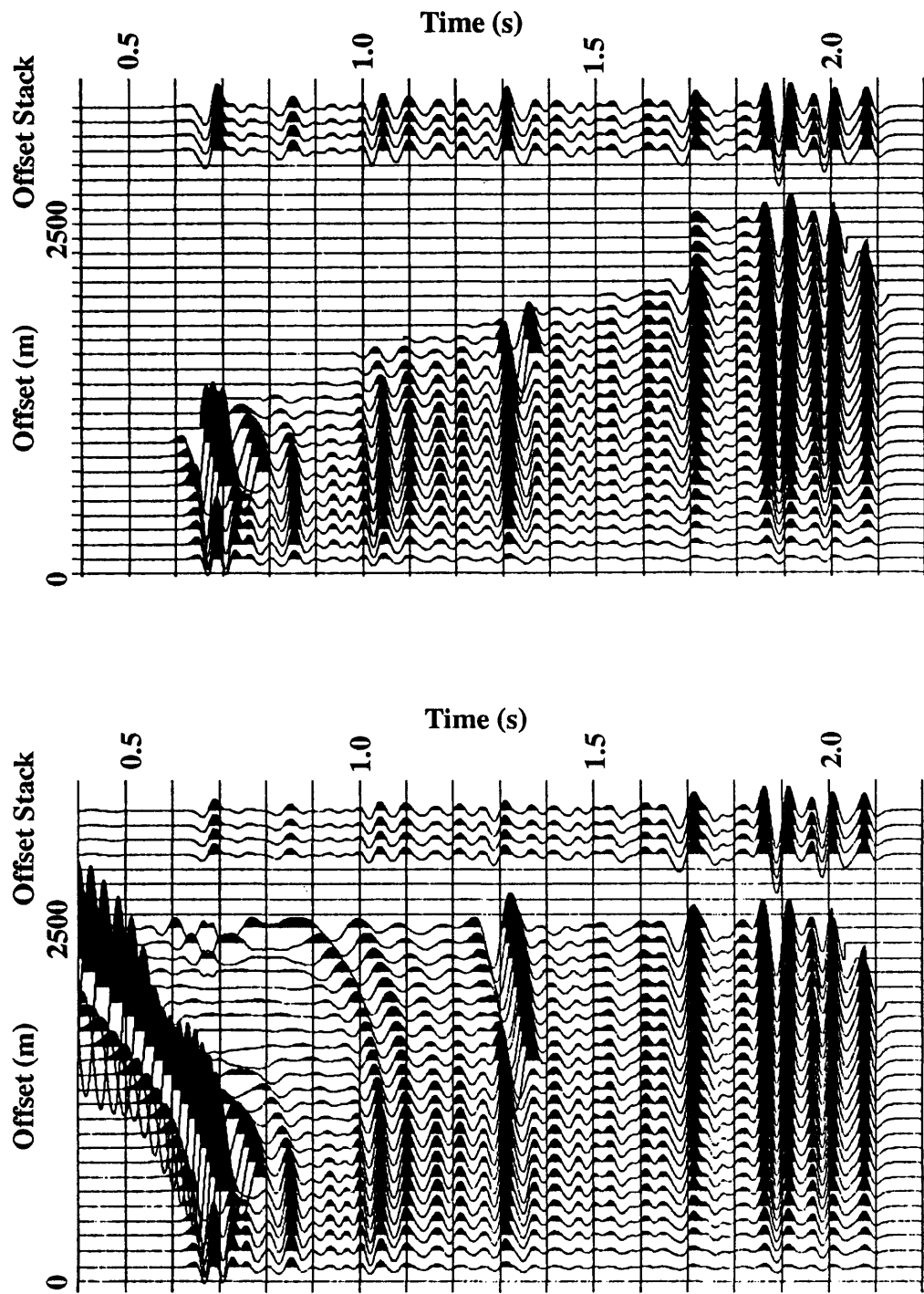
The extent of the Viking sand channel in the Crystal East survey is roughly outlined by the 10-m sand thickness isopach, shown in Chapter 6 as Figure 6.1. Examination of the three lines from this survey fails to indicate an increase in amplitude of the Viking reflection on either the vertical or radial components (Figures 6.7 to 6.9). Thus, in the hope that an analysis of  $V_P/V_S$  would be able to discern what the naked eye could not,  $V_P/V_S$  was calculated for an interval covering the Viking. The interval chosen for this analysis extended from a reflector just above the top of the Viking to another



(a)

(b)

FIG. 7.1. P-P synthetic seismograms for offsets ranging from zero to 3125 m, generated from the P-wave sonic and density logs of well 8-9-45-3W5: (a) without mute; (b) with mute applied.



(a) (b)

FIG. 7.2. P-SV synthetic seismograms for offsets ranging from zero to 2500 m, generated from the P-wave sonic and density logs of well 8-9-45-3W5, using a  $V_p/V_s$  of 2.0: (a) without mute; (b) with mute applied.

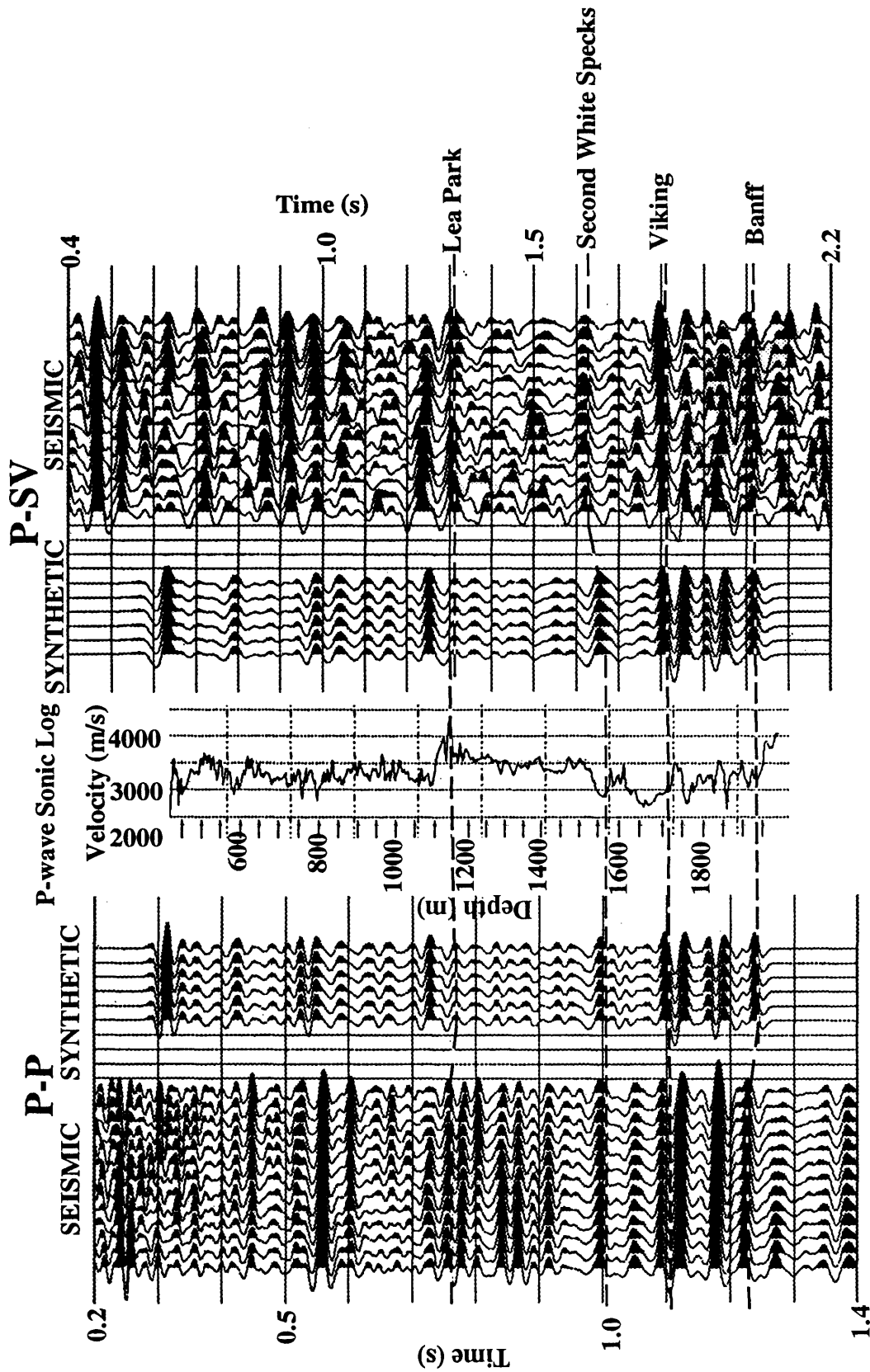


FIG. 7.3. Identification of events and correlation between vertical component (P-P) and radial component (P-SV) of line 6223 using P-P and P-SV synthetics generated from the P-wave sonic and density logs of well 8-9-45-3W5.

reflector just below the Viking, since attempting to pick only the actual Viking zone would require instantaneous phase displays. Due to the variations in fold and offsets in the sections, waveform variations would occur which would introduce error into the analysis. Choosing a larger interval allows for the waveform variations to be reduced; however it also complicates the analysis by including some effects of the lithology in the zones above and below the Viking zone. Further, variations in lithology inside the range chosen may also serve to interfere with the observed anomaly. The smoothed results of this analysis for line 6223 of the Crystal East survey, along with the geologic model of the sand channel, are shown as Figure 7.5. This analysis was also completed for lines 6222 and 6224, but the correlation between sand thickness and  $V_P/V_S$  was not as apparent as for line 6223.

#### **7.4 Discussion**

The advantage of using the radial-component section with the vertical-component section is apparent in the ability to derive another physical property of rocks, the S-wave velocity. The ratio of the P-wave to the S-wave velocity,  $V_P/V_S$  allows differentiation of Viking sandstone channels from the background shale (Figure 7.5). The  $V_P/V_S$  plot clearly shows a decrease of  $V_P/V_S$  as sand thickness increases.

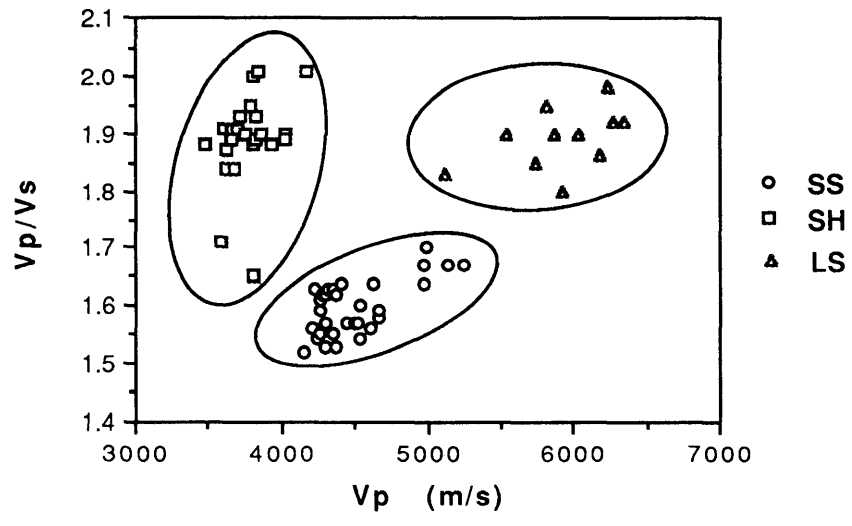


FIG. 7.4.  $V_p/V_s$  versus  $V_p$  for sandstone, limestone, and shale (Miller and Stewart, 1990)

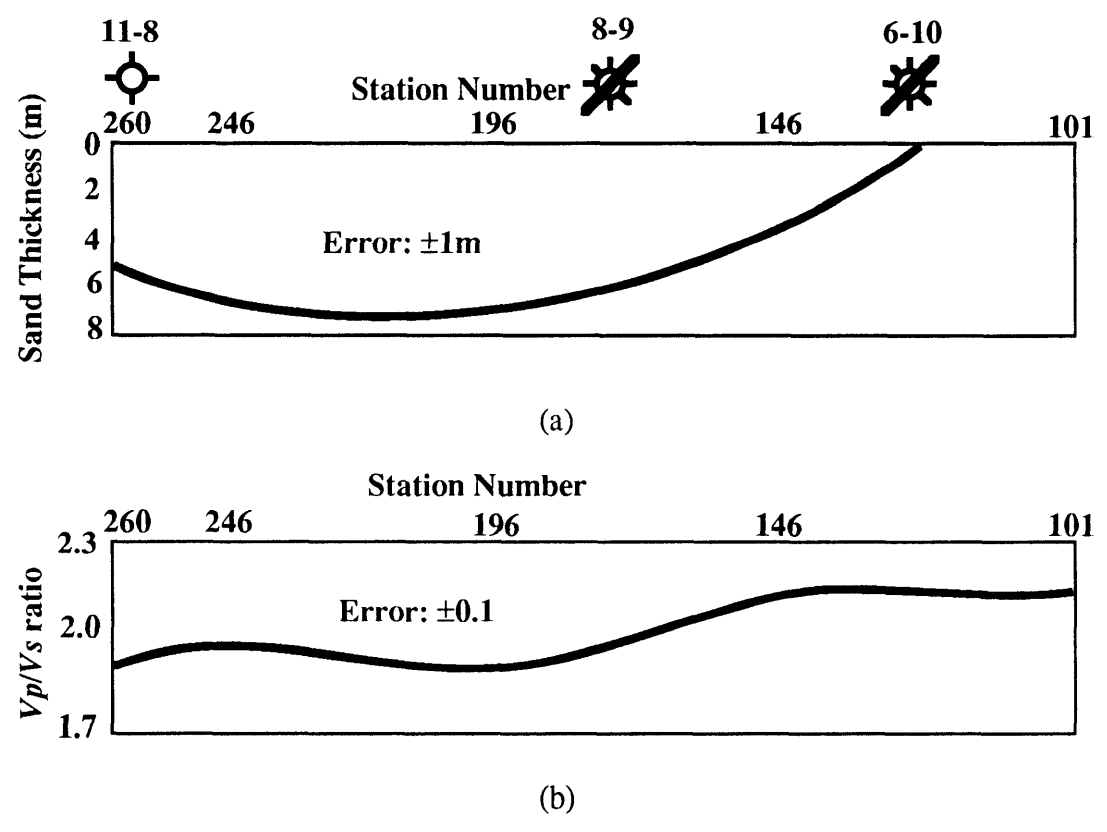


FIG. 7.5. (a) Viking sand channel model and (b) corresponding  $V_p/V_s$  anomaly for line 6223 of the Crystal East survey.

## Chapter 8 – SUMMARY AND CONCLUSIONS

### 8.1 Summary

This thesis has examined the processing and interpretation of P-SV seismic data. The general processing flow for converted-wave (P-SV) surface-seismic data was described in Chapter 2. Several steps, polarity reversal of the trailing spread, geometric-spreading compensation, P-SV stacking-velocity determination, and NMO correction, were discussed in detail.

The various methods available for converted-wave binning were discussed in Chapter 3. These included the CMP, the asymptotic approximation, the depth-variant CCP, and the P-SV DMO methods. These methods were tested by applying them to a structurally complex P-SV synthetic-seismic section. The P-SV synthetic section was designed to simulate a thrust fault structure, the Highwood Structure, located near Turner Valley, Alberta. The result provided by the more computer-intensive methods, DMO and depth-variant binning, proved vastly superior to the other methods for shallow and steeply dipping reflectors. The asymptotic approximation works well at greater depths, while the CMP method gives undesirable results for P-SV data.

The processing results for the radial and transverse components of one of the lines of a three-component seismic survey from Slave Lake, Alberta, were presented in Chapter 4. A high-energy event on the radial-component (P-SV) shot records was observed and identified as a shear-wave refraction.

In Chapter 5, various converted-wave static correction methods were examined and applied to the Slave Lake data set. Refraction static correction methods were extended from P-P to P-SV seismic data by using half of the P-wave refraction static solution and half of the S-wave refraction static solution. Hand-picking of the CRP-

stacked section gave a good result, although it was very time-consuming. The two refraction static correction methods, time-difference and EGRM Gauss-Seidel, both gave results that were inferior to those of hand-picking, but do have the advantage of providing a better long-wavelength static solution.

The results of processing a two-component dynamite survey from Crystal East, Alberta, were presented in Chapter 6. The radial-component data were of better quality than those of the Slave Lake survey, having smaller static shifts and higher signal-to-noise ratios. However, the radial-component data still had a higher noise level and a much narrower bandwidth than the vertical-component data. Correlation of the radial components indicates that there is little anisotropy in the area.

The interpretation of the Crystal East data set was discussed in Chapter 7. Correlation between the P-P and P-SV seismic data, as well as event interpretation, was achieved through P-P and P-SV synthetic seismograms. The ratio of P-wave velocities to S-wave velocities,  $V_P/V_S$ , was calculated from time intervals on the vertical- and radial-component final stacked sections. Lateral variation in  $V_P/V_S$  matched well with changes in the thickness of Viking sandstone, indicating that  $V_P/V_S$  could be an effective tool in discriminating sandstone from shale.

## **8.2 Conclusions**

This thesis has presented a general processing flow for converted-wave (P-SV) surface-seismic data. The most common problems encountered: binning, static correction, and interpretation were discussed in detail. Sponsors of the CREWES Project have access to these results and have already successfully implemented most of the techniques presented.

The main conclusions derived from this thesis are:

- i) P-SV surface-seismic data can result in high-quality final stacked sections using the processing flow outlined. The radial-component (P-SV) data can be correlated with the vertical-component (P-P) data using P-P and P-SV synthetics.
- ii) Depending on the offset-to-depth ratio relevant to the zone of interest and the amount of dip present, different converted-wave binning methods can be employed. P-SV DMO and depth-variant CCP binning are recommended for steeply dipping and shallow reflectors, while asymptotic CCP binning would be satisfactory for deep, relatively horizontal reflectors.
- iii) The converted-wave static solution can be obtained using several methods. Stack-power optimization and hand-picking of the CRP-stacked section can both be used successfully for eliminating converted-wave static shifts. Refraction static methods can also be used with limited success if S-wave refractions are present.
- iv) Clean sandstone can readily be delineated from clean shale using the lateral variations of the ratio of P-wave to S-wave velocity, derived from differences of the time intervals on the P-P and the P-SV final stacked sections.

## REFERENCES

- Aki, K. and Richards, P. G., 1980, *Quantitative Seismology*, **1**: W. H. Freeman and Company, San Francisco.
- Anno, P. D., 1987, Two critical aspects of shear-wave analysis: Statics solutions and reflection correlations, *in* Danbom, S. H., and Domenico, S. N., Eds., *Shear Wave Exploration: Society of Exploration Geophysicists*, 48-61.
- Barry, K. M., 1967, Delay time and its application to refraction profile interpretation, *in* Musgrave, A. W., Ed., *Seismic refraction prospecting: Society of Exploration Geophysicists*, 348-361.
- Beach, F. K., 1962, Viking deposition: *Journal of the Alberta Society of Petroleum Geologists*, **10**, No. 4, 210-212.
- Behle, A., and Dohr, G., 1985, Converted waves in seismic exploration, *in* Dohr, G. E., *Seismic Shear Waves: Handbook of Geophysical Exploration*, **15b**, 178-220.
- Boadu, F. K., 1988, Tomographic inversion for shear wave static corrections: unpublished Geophysics 701 research paper, University of Calgary.
- Cary, P. W., and Eaton, D. W. S., 1993, Short Note: A simple method for resolving large converted-wave (P-SV) Statics, *Geophysics*, **58**, 429-433.
- Cherry, J. T., and Waters, K. H., 1968, Shear-wave recording using continuous signal methods: Part I – Early development: *Geophysics*, **33**, 229-239.
- Chung, W. Y., and Corrigan, D., 1985, Gathering mode-converted shear waves: a model study: 55th Annual International Meeting, Society of Exploration Geophysicists, Expanded Abstracts, 602-604.
- Corbin, R. J., Bell, D. W., and Danbom, S. H., 1987, Shear- and compressional-wave surface and downhole tests in southern Louisiana, *in* Danbom, S. H., and

- Domenico, S. N., Eds., Shear Wave Exploration: Society of Exploration Geophysicists, 62-75.
- de Amorim, W. N., Hubral, P., and Tygel, M., 1987, Computing field statics with the help of seismic tomography: *Geophysical Prospecting*, **35**, 907-919.
- Deregowski, S. M., 1985, An integral implementation of dip moveout: Presented at the 47th Annual Meeting, European Association of Exploration Geophysicists.
- Dewey, J., and Byerly, P., 1969, The early history of seismometry (to 1900): *Bulletin of the Seismological Society of America*, **59**, No. 1, 183-227.
- Diggins, C., Carvill, C., and Daly, C., 1988, A Hybrid Refraction Algorithm, 58th Annual International Meeting, Society of Exploration Geophysicists, Expanded Abstracts, 578-581.
- Eaton, D. W. S., and Lawton, D. C., 1992, P-SV stacking charts and binning periodicity: *Geophysics*, **57**, 745-748.
- Eaton, D. W. S., Slotboom, R. T., Stewart, R. R., and Lawton, D. C., 1990, Depth-variant converted-wave stacking: 60th Annual International Meeting, Society of Exploration Geophysicists, Expanded Abstracts, 1107-1110.
- Ensley, R. A., 1984, Comparison of P- and S-wave seismic data: A new method for detecting gas reservoirs: *Geophysics*, **49**, 1420-1431.
- Erickson, E. L., Miller, D. G., and Waters, K. H., 1968, Shear-wave recording using continuous signal methods: Part II – Later experimentation: *Geophysics*, **33**, 240-254.
- Farrell, R. C., and Euwema, R. N., 1984, Surface consistent decomposition of refraction ray-paths: 54th Annual International Meeting, Society of Exploration Geophysicists, Expanded Abstracts, 424-425.
- Fromm, G., Krey, T., and Wiest, B., 1985, Static and dynamic corrections, *in* Dohr, G. Ed., *Seismic Shear Waves: Handbook of Geophysical Exploration*, **15a**, 191-225.

- Gardner, G. H. F., and Harris, M. H., 1968, Velocity and attenuation of elastic waves in sands: Society of Professional Well Log Analysts, 9th Annual Logging Symposium, M1-M19.
- Gardner, L. W., 1939, An areal plan of mapping subsurface structure by refraction shooting: *Geophysics*, **4**, 247-259.
- Gardner, L. W., 1967, Refraction seismograph profile interpretation, *in* Musgrave, A. W., Ed., *Seismic refraction prospecting*: Society of Exploration Geophysicists, 338-347.
- Garotta, R., 1985, Observation of shear waves and correlation with P events, in Dohr, G. Ed., *Seismic Shear Waves: Handbook of Geophysical Exploration*, **15a**, 1-86.
- Garotta, R., Marechal, P., and Magesan, M., 1985, Two component acquisition as a routine procedure for recording P-waves and converted waves: *Journal of the Canadian Society of Exploration Geophysicists*, **21**, No. 1, 40-53.
- Hampson, D., and Russell, B., 1984, First-break interpretation using generalized linear inversion: *J. Can. Society of Exploration Geophysicists*, **20**, 40-54.
- Harrison, M. P., 1992, Processing of P-SV surface-seismic data: anisotropy analysis, dip moveout, and migration: Ph. D. dissertation, University of Calgary.
- Horton, C. W., 1943, Secondary arrivals in a well velocity survey: *Geophysics*, **8**, 290-296.
- Iverson, W. P., Fahmy, B. A., and Smithson, S. B., 1989,  $V_p/V_s$  from mode-converted P-SV reflections: *Geophysics*, **54**, 843-852.
- Jolly, R. N., 1956, Investigation of shear waves: *Geophysics*, **21**, 905-938.
- Judson, D. R., Schultz, P. S., and Sherwood, J. W. C., 1978, Equalizing the stacking velocities of dipping events via DEVELISH: presented at the 48th Annual International Meeting, Society of Exploration Geophysicists.

- Koldijk, W. S., 1976, Gilby Viking 'B': a storm deposit, *in* The Sedimentology of Selected Oil and Gas reservoirs in Alberta: Canadian Society of Petroleum Geologists, 62-77.
- Lawton, D. C., 1989, Computation of refraction static corrections using first-break traveltimes differences: *Geophysics*, **54**, 1289-1296.
- Lawton, D. C., 1990, A 9-component refraction seismic experiment: *Canadian Journal of Exploration Geophysicists*, **26**, 7-16.
- Lawton, D. C., and Howell, C. E., 1992, P-SV and P-P synthetic stacks, presented at the 62nd Annual International Meeting, Society of Exploration Geophysicists, Expanded Abstracts, 1344-1347.
- Levin, F. K., 1971, Apparent velocity from dipping interface reflections: *Geophysics*, **36**, 510-516.
- MacKay, P. A., 1991, Geometric, kinematic, and dynamic analysis of the structural geology at Turner Valley, Alberta: M. Sc. Thesis, University of Calgary.
- Marsden, W. H., 1993a, Static corrections – a review: Part 1: THE LEADING EDGE, **12**, 43-39.
- \_\_\_\_\_, 1993b, Static corrections – a review: Part 2: THE LEADING EDGE, **12**, 115-120.
- \_\_\_\_\_, 1993c, Static corrections – a review: Part 3: THE LEADING EDGE, **12**, 210-216.
- Mayne, W. H., 1956, Seismic Surveying: U.S. Patent 2,732,906 (application 1950), (Abstract): *Geophysics*, **21**, 856.
- Mayne, W. H., 1962, Common reflection point horizontal data stacking techniques: *Geophysics*, **27**, 927-938.

- Miller, S. L. M., and Stewart, R. R., 1990, Effects of lithology, porosity and shaliness on P- and S-wave velocities from sonic logs: *Canadian Journal of Exploration Geophysicists*, **26**, 94-103
- Nazar, B. D., 1991, An interpretive study of multicomponent seismic data from the Carrot Creek area of west-central Alberta: M. Sc. thesis, University of Calgary.
- Newman, P., 1973, Divergence effects in a layered earth: *Geophysics*, **38**, 481-488.
- Palmer, D., 1980, The generalized reciprocal method of seismic refraction interpretation: Society of Exploration Geophysicists.
- Pickett, G. R., 1963, Acoustic character logs and their applications in formation evaluation: *Journal of Petroleum Technologists*, 659-667.
- Press, F., and Dobrin, M. B., 1956, Seismic studies over surface layer: *Geophysics*, **21**, 285-298.
- Richter, C. F., 1935, An instrumental earthquake scale: *Bulletin of the Seismological Society of America*, **25**, 1-32.
- Robertson, J. D., and Pritchett, W. C., 1985, Direct hydrocarbon detection using comparative P-wave and S-wave seismic sections: *Geophysics*, **50**, 383-393.
- Ronen, J., and Claerbout, J. F., 1985, Surface-consistent residual statics estimation by stack-power maximization: *Geophysics*, **50**, 2759-2767.
- Rothman, D. H., 1985, Nonlinear inversion, statistical mechanics, and residual statics estimation: *Geophysics*, **50**, 2784-2796.
- Russell, B. H., 1989, Statics corrections – a review: *Canadian Society of Exploration Geophysicists, The Recorder*, **14**, no. 3, 16-30.
- Schafer, A., W., 1991, The determination of converted-wave statics using P refractions together with SV refractions: presented at the 61st Annual International Meeting, Society of Exploration Geophysicists, Expanded Abstracts, 1413-1415.

- Sheriff, R. E., 1991, Encyclopedic dictionary of exploration Geophysics, third edition: Society of Exploration Geophysicists.
- Slotboom, R. T., 1990, Converted-wave (P-SV) moveout estimation: presented at the 60th Annual International Meeting, Society of Exploration Geophysicists, Expanded Abstracts, 1104-1106.
- Sukaramongkol, C., and Lawton, D. C., 1992, P-P and P-SV seismic imaging in the Triangle Zone, Canadian Rocky Mountain Foothills: CREWES Project Research Report, University of Calgary, **4**, ch. 10, 1-23.
- Taner, M. T., and Koehler, F., 1969, Velocity spectra – digital computer derivation and applications of velocity functions: Geophysics, **34**, 859-884.
- Tatham, R. H., 1982,  $V_P/V_S$  and lithology: Geophysics, **47**, 336-344.
- Tatham, R. H., 1985, Shear waves and lithology, in Dohr, G. Ed., Seismic Shear Waves: Handbook of Geophysical Exploration, **15a**, 87-133.
- Tatham, R. H., and Krug, E. H., 1985,  $V_P/V_S$  interpretation, in A. A. Fitch, Ed., Developments in geophysical exploration methods–6: Elsevier Applied Science Publications, 139-188.
- Tatham, R. H., and Stoffa, P. L., 1976,  $V_P/V_S$  - A potential hydrocarbon indicator: Geophysics, **41**, 837-849.
- Tessmer, G., and Behle, A., 1988, Common reflection point data-stacking technique for converted waves: Geophysical Prospecting, **36**, 661-688.
- Ursin, B., 1990, Offset-dependent geometrical spreading in a layered medium: Geophysics, **55**, 492-496.
- Vasudevan, K., Wilson, W. G., and Laidlaw, W. G., 1992, Simulated annealing statics computation using an order-based energy function: Geophysics, **57**, 1831-1839.
- Wattrus, N. J., 1989, Inversion of ground roll dispersion: 59th Annual International Meeting, Society of Exploration Geophysicists, Expanded Abstracts, 946-948.

- White, J. R., Heaps, S. N., and Lawrence, A. L., 1956, Seismic waves from a horizontal force: *Geophysics*, **21**, 715-723.
- Winterstein, D. F., 1986, Anisotropy effects in P-wave and SH-wave stacking velocities contain information on lithology: *Geophysics*, **51**, 661-672.
- Winterstein, D. F., and Hanten, J. B., 1985, Supercritical reflections observed in P- and S-wave data: *Geophysics*, **50**, 185-195.